PREDICTIVE MODELING OF RESIDUAL STRESS IN MQL GRINDING AND SURFACE CHARACTERISTICS IN GRINDING OF CERAMICS

A Dissertation
Presented to
The Academic Faculty

by

Yamin Shao

In Partial Fulfillment
Of the Requirements for the Degree
Doctor of Philosophy in Mechanical Engineering

Georgia Institute of Technology

Aug 2015

PREDICTIVE MODELING OF RESIDUAL STRESS IN MQL GRINDING AND SURFACE CHARACTERISTICS IN GRINDING OF CERAMICS

Approved by:

Dr. Steven Y. Liang, Advisor
School of Mechanical Engineering
Georgia Institute of Technology

Dr. Roshan Vengazhiyil
School of Industrial & Systems Engineering
Georgia Institute of Technology

Dr. Shreyes N. Melkote
School of Mechanical Engineering
Georgia Institute of Technology

Dr. Ismail Lazoglu
College of Engineering
Koc University

Dr. Steven Danyluk
School of Mechanical Engineering
Georgia Institute of Technology

Dr. Beizhi Li
College of Mechanical Engineering
Donghua University

Date Approved: May 2, 2015

ACKNOWLEDGEMENTS

It is a pleasure to thank the many people and sponsors who made who made this research possible.

Foremost, I would like to express my sincere thanks to my advisor, Dr. Steven Y. Liang, for his inspiration and guidance on my PhD study and also for his encouragement and support on my graduate school life. I would also like to thank members of my committee, Professors Shreyes Melkote, Steven Danyluk, Roshan Vengazhiyil, Ismail Lazoglu, and Beizhi Li for their advice. Special thanks goes to Dr. Beizhi Li, for her support on the experimental studies in my research.

I also want to thank my colleagues Dr. Xia Ji, Manik Rajora, Alexander Shih, Pan Zou, Zhipeng Pan, and especially Dr. Zishan Ding and Omar Fergani for their help and many good ideas. Thanks are also due to John Morehouse, Steven Sheffield, Louis Boulanger, Drew Bullard, Melissa Raine, Glenda Johnson, Kysten Raleigh from ME and John Anthony from Corning Inc. for their valuable help and support. I would like to thank Corning Inc. for the financial support.

Most importantly, I would like to thank my parents, Meisheng Shao and Mei Liu, and my fiancé Ying Cui for their love, company and continuous support throughout my graduate study. This work would not be possible without them.

TABLE OF CONTENTS

Page

LIST OF TABLES

Page

LIST OF FIGURES

Page

LIST OF SYMBOLS

A_m	Metallic contact area
A_b	Adsorbed lubricant film contact area
F , N	Friction force and normal load in boundary lubrication
s_b , p_b	Shear strength and yield pressure at the adsorbed lubricant film contact area
s_m , p_m	Shear strength and yield pressure at the metallic contact area
R_t	Asperity tip radius
n_0	Total asperity number
D_i	Inclination distribution function
a_s	Approach of two surfaces
$H_{\max}$	Asperity height distribution
t_b	Effective adsorbed lubricant film thickness
μ	Friction coefficient
C_1, C_2, C_3	Coefficients in boundary lubrication theory
t, α_s	Undeformed chip thickness and corresponding rake angle
t_{cr}, α_{cr}	Critical undeformed chip thickness and corresponding rake angle
t_{nom}, α_{nom}	Undeformed chip thickness where the local rake angle reaches nominal rake angle of the grit and nominal rake angle
τ	Workpiece material flow stress
b	Local cutting width

β	Friction angle
α	Local rake angle
ϕ	Local shear angle
r	Grit radius
rc	Cutting ratio
t_c	Cut chip thickness
$F_{tg,chip}$, $F_{ng,chip}$	Single grit forces in tangential and normal directions due to chip formation
ε	Strain in the deformation zone
$\dot{\varepsilon}$	Strain rate in the deformation zone
HB	Brinell hardness of the workpiece
F_p	Indentation force
D	Grit diameter
$F_{tg,ploughing}$, $F_{ng,ploughing}$	Single grit forces in tangential and normal directions due to ploughing
$F_{tg,rubbing}$, $F_{ng,rubbing}$	Single grit forces in tangential and normal directions due to rubbing
τ_w , σ_w	Shear and normal stress in rubbing zone
L_{VB}	Wear flat length
F_{tg} , F_{ng}	Single grit forces in tangential and normal directions
a	Wheel depth of cut
V_s	Wheel speed

V_w	Workpiece speed
l_c	Real contact length
C_d	Dynamic grit density
d_s	Wheel diameter
F_n'	Normal force per contact length
R_r	Constant that represents the roughness of the surfaces in contact
K_s, K_w	Wheel and workpiece elasticity
E_s, E_w	Wheel and workpiece modulus of elasticity
ν_s, ν_w	Wheel and workpiece Poisson's ratio
z	Radial distance measured into the wheel
A, k	Parameters of grit density
$\tan(\varepsilon_z)$	Represents kinematic effect in dynamic grit density calcualtion
d_e	Equivalent wheel diameter
F_t, F_n	Total tangential and normal grinding forces
w	Grinding width
$T_{(x,z)}$	Temperature in the workpiece at point (x, z)
q_{in}	Heat flux into the workpiece
q_{out}, q_f	Heat flux taken away by fluid
q_t	Total heat flux generated

q_s	Heat flux enters wheel
q_{ch}	Heat flux taken away by chip
k_w, k_g, k_l, k_f	Thermal conductivity of the workpiece, air, oil-drop and the air-oil mixture
α_w	Thermal diffusivity of the workpiece
$\rho_w, \rho_g, \rho_l, \rho_f$	Density of the workpiece, air, oil-drop and the air-oil mixture
c_w, c_g, c_l, c_f	Specific heat of the workpiece, air, oil-drop and the air-oil mixture
K_0	Modified Bessel function of the second kind of order zero
R_{ws}	Workpiece-wheel partition ratio
h_f	Convection heat transfer coefficient of MQL/fluid
T_0, T	Ambient and workpiece temperature
Nu, Pr, Re	Nusselt number, Prandtl number and Reynolds number of the fluid
μ_g, μ_l, μ_f	Dynamic viscosity of the air, oil-drop and the air-oil mixture
u_f	Velocity of the fluid
$\overline{\chi}$	Gas weight fraction in air-oil mixture
$\dot{V}_g, \dot{V}_l$	Volumetric flow rate of air and oil
A, *B*, *C*, *m*, *n*, and $\dot{\varepsilon}_0$	Johnson-Cook parameters
$\sigma_{ij}^{mech}, \sigma_{ij}^{therm}$	Mechanical and thermal stresses
Ψ	Blending function

h	Plastic modulus
G	Elastic shear modulus
S_{ij}	Deviatoric stresses
α_{ij}	Back stresses
R	Uniaxial normalized radius of the yield surface
$\dot{\varepsilon}_{effective}$	Effective plastic strain rate
$\dot{\varepsilon}_{ij}^{p}$	Plastic strain rate
c_L	Lateral crack size
h	Plastic zone depth
K_c	Fracture toughness
H	Workpiece hardness
P	Single grit load
c_M	Median crack size
Q	Increase of out of plane hoop stress for a corresponding tangential-normal load ratio
d_c	Critical depth of cut for ductile-brittle transition
R_a	Arithmetic mean surface roughness
p', p''	Probabilities of a groove depth to be less and greater than y_{CL} but smaller than critical undeformed chip thickness t_{cr}
p	Probability of a grit engagement depth greater than critical undeformed chip thickness
y_{CL}	Position of center-line

σ_F	Fracture strength of a component
Y	Geometry factor
P_f	Weibull failure probability

SUMMARY

Surface integrity is of great significance in grinding performance since grinding process is often used as a finishing step. For metallic materials, residual stresses play an important role in surface integrity for its strong effect on fatigue life, corrosion resistance, and part distortion. For ceramic materials, the surface damage induced by grinding process could greatly affect the mechanical strength and surface finish of the component. The functional behavior of machined components can be enhanced or impaired by the grinding process. Because of this, understanding the surface integrity imparted by grinding is very important.

The use of fluid is common in grinding process, however, the high cost and environmental impact of the conventional flood cooling is very undesirable. The minimum quantity lubrication (MQL) have been introduced in industry for about two decades as a promising alternative to conventional flood cooling for economical and environmental advantages. A comprehensive understanding of the MQL effect on the process performances and surface integrity is of great value to the implementation of MQL technique in industrial situation.

Grinding-induced residual stress prediction has been a topic of research since the 1970's while the studies of MQL grinding is still on the early stage with experimental investigations. A comprehensive study and quantitative description of MQL effect on the residual stress generation in grinding is highly demanded. On the other hand, although there has been significant research in the area of surface damage in ceramic grinding, there are still opportunities for advancing predictive methods. Therefore, the objectives of the current research are set as follows: (1) develop a method of predicting residual stress

based on an analytical description of the grinding process under MQL condition, (2) develop a method of predicting surface finish and damage in ceramic grinding, and (3) validate the model with experimental data.

The research will first focus on predicting residual stresses in MQL grinding based on first principles. This includes predictive models of grinding forces, and grinding temperature stemmed from grinding kinematics and dynamics principles as part of the overall modeling effort. The effect of MQL on both lubrication and cooling aspects has been integrated into these models. The mechanical and thermal output parameters will serve as the basis for determining the loading history which generate residual stresses. The research will also aim at surface roughness modeling in ceramic grinding. A ductile-brittle mixed surface generation is predicted based on the nature of ceramic materials and grinding kinematics. The crack system developed from indentation fracture mechanics approach will be utilized in evaluating the brittle mode surface generation. The modeling techniques will be applied to a range of grinding conditions and materials.

This research would aid in evaluating various surface integrities in grinding of metallic and ceramic materials with little experimental efforts. The output could be used to machine these materials effectively to order to improve the functionality of the component.

CHAPTER 1

INTRODUCTION

1.1 Overview and Motivation

Grinding is a complex yet very important manufacturing process. Its competitiveness in producing superior surface finish and processing hard and brittle materials is virtually unchallenged by another machining process. The improvement of grinding process in terms of maximizing productivity, optimizing workpiece quality and achieving high energetic efficiency will undoubtedly benefit our whole society.

In recent decades, with increasing awareness of sustainable manufacturing, there has been rising demand for the development of environmental-friendly and energy-conserving manufacturing technologies. The concept of minimum quantity lubrication (MQL), which refers to the use of cutting fluids of only a minute amount, has been suggested two decades ago as a means of addressing the environmental and economical issues [1]. The minimization of cutting fluids not only alleviates environmental impact but also leads to economical benefits by ways of saving lubricant cost and workpiece/tool/machine cleaning cycle time. While extensive research has been conducted in various cutting processes such as turning, milling and drilling, MQL grinding is still a relatively new research area that requires more comprehensive analysis. In the profiling of MQL grinding capability, residual stress plays an important role for its effect on fatigue life, corrosion resistance, and part distortion of metallic components [2].

Therefore, the evaluation of the residual stress in ground workpiece imparted by MQL grinding is critical to understand the process.

Aside from the capability of achieving superior surface finish and fine tolerance, another area where grinding is virtually unchallenged is for machining of ceramic materials, because of their extreme hardness or brittleness, cannot be efficiently shaped by other methods [3]. Due to the high brittleness, the surface finish as well as mechanical strength of ground ceramic components often suffers from surface damage induced by brittle fracture. Previous research has shown that the material removal mechanism in grinding of ceramic components could behave as a mixture of plastic flow and brittle fracture [4], while the extent of mixture depends on process parameters and tool/workpiece material properties. However, the quantitative description of material removal process in ceramic grinding and its influence on surface finish and mechanical strength is still absent. The application of indentation fracture mechanics with machining process mechanics to real grinding conditions is appealing.

1.2 Research Goals and Objectives

Despite the extensive research in these areas, there are still opportunities for advancing the predictive methods for residual stress in MQL grinding of metallic components and the quantitative description of surface characteristics in grinding of ceramic components. The objective of current research are as follows: (1) develop an analytical model to predict residual stress in MQL grinding process, (2) develop an analytical model to predict surface finish and strength degradation in grinding of ceramic components, (3) validate the methodology with experimental data.

1.3 Research Approach

In this research, the physical-based studies of grinding process under MQL condition will be established via the robust, repeatable modeling of grinding force, temperature and residual stresses. A flowchart of the methodology is shown in Figure 1.1.

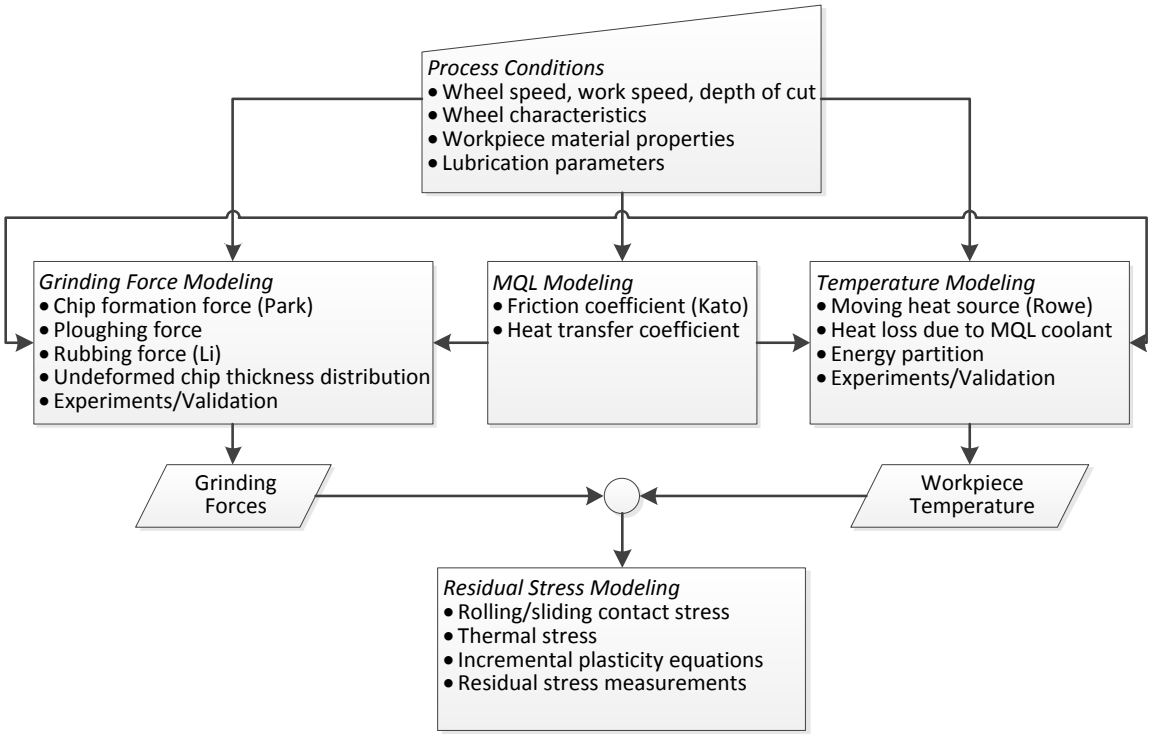

Figure 1.1 Research approach for residual stress modeling

As shown in the flowchart, the model takes grinding process conditions such as wheel speed, workpiece feed, and depth of cut along with wheel characteristics, workpiece material properties and lubrication parameters into models to predict grinding forces and temperature. The grinding force model starts from the basis of the process given by the interaction between an individual grinding grit with the workpiece [5]. The single grit forces are treated as a combination of chip formation, ploughing, and rubbing

forces [3]. The effect of MQL lubrication on friction coefficient is integrated in the single grit force calculation. Since grinding is a machining process with multiple cutting edges, the single grit interaction is then extrapolated to the whole grinding wheel through undeformed chip thickness distribution models [6]. The active number of cutting edges and the distribution of cutting depths of individual grits are calculated from grinding kinematics and dynamic effects. The grinding forces contribute to the mechanical stress experienced by the newly formed machined surface.

The grinding force results are inputted to the thermal models to predict the temperature rise in the workpiece due to grinding. The cooling effect of MQL is modeled as a heat loss at the grinding contact zone. The temperature distribution in workpiece can produce thermal stresses. Additionally, the material behavior, particularly yield stress, is also affected by temperature.

These aspects of the grinding process are used as inputs into a thermo-mechanical elasto-plastic model to predict residual stresses. The model predictions will then be validated with experimental data to determine the effectiveness of the modeling technique. The goal of this part of work is to establish a predictive model for grinding induced residual stress. Because an extensive calibration of parameters will be unnecessary, the research will enable prediction of grinding induced residual stress with much less experimental work.

In Figure 1.2, a flowchart for surface characteristics modeling in ceramic grinding is presented. In this study, from indentation fracture mechanics has been utilized in prediction of surface fracture generation. The ratio of surface fragmentation area generated in grinding process is represented as surface fracture percentage. A close

relationship between surface fracture percentage with crack size, and surface finish is proposed in this research.

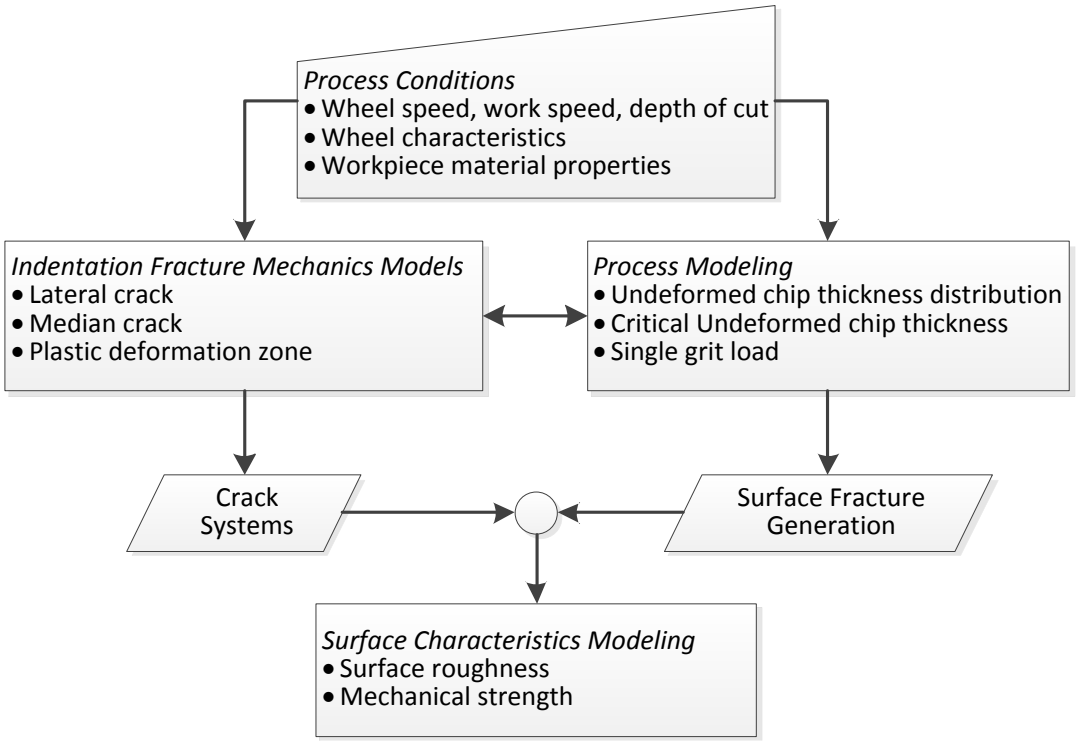

Figure 1.2 Research approach for surface characteristics modeling in ceramic grinding

The review of grinding mechanism for ceramic grinding suggested a mixture of plastic flow and brittle fracture material removal. The surface fracture percentage is predicted based on process mechanics and ductile-brittle transition behavior. The lateral and median crack systems are then associated with the surface fracture generation model to predict some of the important parameters in ceramics grinding such as crack size, surface roughness and strength degradation. This research will enable quantitative description of the relationship between process conditions such as process parameters,

wheel characteristics and material properties to the surface quality in grinding of ceramic materials.

1.4 Overview of Thesis

This dissertation begins by providing background information and a review of the present and past literature in the area of MQL grinding and ceramic grinding in Chapters 1 and 2. Following the discussion of grinding force, temperature and residual stress modeling in MQL grinding in Chapters 3-5. The model calibration and validation with experimental measurements is presented in Chapter 6. In Chapter 7, the establishment of an analytical model to predict surface finish and strength degradation is presented. Conclusions and recommendations will follow in Chapter 8 and finalize the thesis.

CHAPTER 2

LITERATURE REVIEW

The literature review is categorized into three parts: 1) investigations on MQL grinding, 2) research on residual stress modeling, 3) research on surface damage in ceramic grinding. The investigations on MQL grinding includes discussions on the experimental observations on cutting forces, cutting temperatures, surface roughness and other behaviors with the implementation of minimum quantity lubrication in grinning process. The research on residual stress modeling covers different modeling efforts for residual stress induced by machining process. These two parts conclude the previous research in MQL grinding residual stress and lead up to the current state of the field. The literature survey on ceramic grinding mechanism and induced surface damage discusses the relevant researches on ceramic grinding from both indentation fracture mechanics and machining approach. After the review, a summary of potential avenues for the current research is presented.

2.1 Literature Review on Residual Stress Modeling in MQL grinding

2.1.1 Investigations on MQL Grinding

Minimum quantity lubrication refers to the use of minimal cutting fluids – typically of a flow rate of 50 to 500 ml/hour – which is about three to four orders of

magnitude lower than the amount commonly used in flood cooling condition, where, for example, up to 10 liters of fluid can be dispensed per minute [1].

MQL has been widely studied in machining process [7, 8, 9, 10, 11, 12] regarding cutting force, temperature, tool wear, and residual stresses. The research in application of MQL to grinding process is rapidly increasing within recent years. Several experimental investigations in MQL grinding has been completed to characterize the effect of MQL on process performances such as grinding force, temperature and surface morphology.

Silva et al [13] has compared MQL grinding to dry and wet conditions in grinding 4340 steel with aluminum oxide wheel. Their results showed MQL grinding achieved less surface roughness and more compressive residual stress on the ground surface than other conditions. However, the influence of grinding parameters such as wheel speed, work speed or depth of cut was not presented and the residual stress were only measured at the ground surface. Li et al [14] also found that MQL achieved more compressive residual stress than flood cooling in grinding of 45 steel.

Shen and Shih [15] evaluated the force, temperature, surface roughness, and energy partition, which is the fraction of grinding energy transported into the workpiece as heat, in the grinding of cast iron using CBN wheel under dry, MQL and flood cooling conditions. While maintaining the similar force and surface roughness performance, the energy partition under MQL condition (around 54%) is in between dry (around 68%) and flooding cooling condition(around 13%). Their study indicated the porous CBN wheel structure can improve the insufficient cooling problem of MQL to a certain extent. Shen et al [16] also studied the effect of nanofluids in MQL grinding which is to apply nano-

sized particles into the lubricant. A slurry layer was formed to help generate a higher G-ratio, smaller grinding forces, and better surface finish.

Sadeghi et al [17] conducted an investigation on MQL grinding of hard-to-machined material Ti-6Al-4V. The analysis indicated MQL technique can achieve similar or better grinding performance as with conventional lubrication methods in terms of grinding force and surface roughness. Sadeghi et al [18] evaluated the performance of different grinding fluids, including mineral, vegetable and synthetic esters oil on the basis of grinding forces and surface quality properties in MQL grinding of 4140 steel. The results concluded that the synthetic oil gave lower tangential forces and the application of cutting fluid of MQL may remain the sharpness of cutting edges.

Tawakoli et al [19] have performed an experimental investigation of MQL grinding under different process parameters. Their results suggested that by the application of MQL, smaller grinding force and higher surface roughness were achieved when grinding of 42CrMo4 soft steel while smaller surface roughness were obtained when grinding of 100Cr6 hardened steel. Tawakoli et al [20] have conducted another experimental investigation of MQL grinding under different oil mist parameters, such as nozzle position, air pressure, and nozzle distance, with grinding of 100Cr6 hardened steel. It is discovered that spray nozzle positioned at approximately 10-20 ° towards the wheel surface achieved best performance. In other research, Tawakoli et al [21] investigated the minimum quantity lubrication grinding of 100Cr6 hardened steel using different abrasive and coolant-lubricant types. Based on the presented results, it was found that vitrified bond SG wheels and grinding oils have potential for the development

of the MQL grinding process in comparison to vitrified and resin bond corundum and water miscible oils.

While a considerable effort has been devoted to experimental investigations, literature shows very limited work in theoretical analysis of mechanical and thermal behavior in MQL grinding. Most recently, Hadad et al [22, 23] have proposed an analytical model to calculate the temperature distribution in the workpiece in MQL grinding of 100Cr6 hardened steel. The convective heat transfer coefficient of MQL/fluid inside and outside the grinding zone have been evaluated by spraying cooling convection heat transfer model. They estimated a value of 43400 W/m^2K for water-based coolants; for MQL fluid, a value of 1400 to 1630 W/m^2K is obtained for different sets of MQL parameters.

Literature review shows the lack of understanding on the effect of MQL on the residual stress behavior. The experimental research has only provided a qualitative understanding of the effect of MQL on grinding. The general findings have indicated that MQL could achieve similar or smaller grinding force and surface roughness but relatively high temperature which suggested sufficient lubrication and insufficient cooling of MQL lubricant/coolant. These effects will directly impact the residual stress profile of the final product.

2.1.2 Residual Stress Modeling in Grinding

This section reviews the research efforts that has aimed to explain the mechanisms of residual stress generation in grinding from different approaches. Experimental, Finite Element Method (FEM), and analytical models has been proposed

to quantitatively describe the residual stress in grinding process relative to process conditions.

Some early studies [24, 25] have aimed to establish an empirical correlation between grinding conditions and surface layer parameters. Kruszynski and Wojcik [26] developed an empirical model for predicting residual stress in grinding by relating the residual stress to a coefficient B which is a product of power density and contact time. A linear correlation between coefficient B and maximum residual stress was found experimentally. It was confirmed for several work materials.

Balart et al [27] investigated the effect of grinding temperature on the residual surface and subsurface stress states for hardened En9, En31, M2 and CP 10V steels. It is concluded that the onset of tensile surface residual stresses is caused by exceeding a critical transition temperature similar to the conclusions of the Chen et al [28].

The experimental research has provided a qualitative understanding of the effects of process parameters on grinding-induced residual stress. The general findings have indicated that in the absence of chemical changes, the residual stress profile is dependent on a combination of loadings. For cases where mechanical loads dominate, compressive residual stress profiles are more likely. Where thermal loads dominate, the residual stress profiles show a more tensile character. However, this relatively simple approach has some apparent drawbacks. First, the application is limited by the time-consuming and costly experiments. Second, the extrapolation of the experimental results is also unreliable with different grinding methods and grinding conditions.

Due to the complexity of grinding process, FEM technique has been utilized to simulate the grinding process. One of the earliest efforts at modeling residual stress in

grinding process using FEM was undertaken by Mishra and Prasad [29]. They investigated the residual stress due to a moving heat source and applied to grinding situation. The author discussed the effect of the magnitude of mechanical force, the rate of heat input, and the speed of movement of the workpiece on the residual stresses.

Mahdi and Zhang [30] have studied the residual stress in grinding induced by full coupling of mechanical deformation, thermal deformation and phase transformation. They found the phase transformation could be the dominant factor for tensile residual stress when the temperature is extremely high. However, no experimental validation was provided in the study.

Moulik et al [31] developed a finite element procedure to calculate the temperatures and stresses due to a moving source of heat in an elastic-plastic workpiece. They found predominantly tensile residual stress near the surface due to the thermal stress and the magnitude of the residual stress increases with increasing heat flux values which is in consistent with the experimental measurement.

Hamdi et al [32] proposed a finite element thermomechanical model for the determination of residual stresses induced by plane grinding process and studied the influence of grinding speed on residual stress. It has been shown that temperatures in the workpiece vary proportionally to wheel speed, and greater the wheel speed, the higher the residual stresses.

Analytical models of residual stress generation, which is based on the mathematical description of physical processes, is very promising for its time efficiency and physical understanding of the process. Many analytical models for machining processes [33, 34, 35] have been developed. However, due to the complex mechanism

induced by multiple grain contact and high temperature in grinding process, a comprehensive model is still under development.

Tonshoff [36] have summarized several efforts in the analytical modeling of residual stress in grinding. In most of the analytical models in grinding residual stress, thermal stresses are described.

Chen [28] investigated the transitional temperature between compressive and tensile residual stresses in ground surfaces based on an analytical approach. It was found that thermal stresses generated in the grinding process were the primary cause of tensile residual stresses. The thermally induced residual stresses are strongly dependent on the workpiece material properties, like yield stress. No mechanical induced stresses are considered in this study.

The current state of analytical modeling of the grinding condition on the residual stress falls short in terms of application to industrial environments. Models like that developed by Chen [28] didn't include the mechanical interaction between the individual grits and the workpiece. The material behavior is also over-simplified to have no work hardening. FEM does an adequate job in predicting the residual stresses, but they are not easily adaptable for varying process parameters because they are typically time consuming. The analytical models cover various aspects of sources of residual stress and mechanisms that affect the profiles. However, a thorough model for predicting residual stress with consideration of mechanical and thermal stresses is currently unavailable.

2.2 Literature Review on Surface Generation in Ceramic Grinding

Ceramics are much more susceptible to surface damage during grinding, as compared to metals, and their subsequent behavior under load is much less forgiving to grinding induced damage [37]. The material removal mechanism in ceramic grinding is key to the analysis of grinding induced surface damage. Most previous research has followed either “machining” approach or the “indentation fracture mechanics” approach [37]. The machining approach to investigating grinding mechanisms typically involves measurement of cutting forces coupled with microscopic observations of grinding debris and surface morphology [4].

2.2.1 Machining Approach

Imanaka et al [38] observed the chip formation process in ceramic grinding using a micro-flash technique. It was observed that many fine particles splinter off the ground surface, which suggests material removed by brittle fracture was crushed into smaller particles. Aside from brittle fracture particles, continuous flow-type chips are also occasionally observed at high grinding speeds and shallow depths of cut, which would indicate ductile flow.

Zhang et al [39] came up with another explanation for material removal mechanism for ceramic grinding. They claimed that material pulverization instead of ductile deformation is taking place underneath the scratched groove and is considered to be the most favorable material removal mechanism at low depth of cut. A loosely connected powder regime was observed in the ground surface.

Malkin [4] summarized the previous efforts in the observation of scratched or ground surfaces. Both “scale-like” cracks and plastic flow were observed on the groove surface, with most material removal in the form of finely crushed particles. An inclined single-point cutting of silicon and germanium showed initial ductile flow progressively changed to brittle fracture after a critical depth of cut was reached. The cutting regimes for silicon is shown in Figure 2.1.

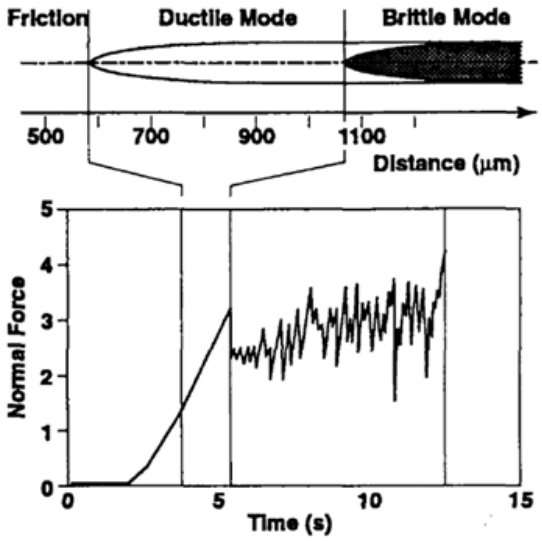

Figure 2.1 Cutting regimes for silicon [4]

Many observations have been reported showing the transition from a ductile to brittle mode for single point cutting. A systematic study of ductile regime grading was conducted using a special face grinder equipped with ultrafine infeed control [40]. An expression for the critical depth of cut corresponding to the threshold load per grain for fracture was derived.

Chen et al [41] measured specific grinding energy versus average uncut chip cross-sectional area for aluminum oxide and silicon nitride. Two distinctive areas have

been identified. Below a critical uncut chip area, the specific energy increases steeply with smaller chip size. Above the transition, the specific energy decreases more slowly as the chip size increases. It is concluded that most of the energy is not expended by brittle fracture but by ductile flow, although most of the material removal is by brittle fracture.

Li and Liao [42]examined previous works related to surface/subsurface damage and the fracture strength of ground structural ceramics. They summarized that crack size, compressive residual stress layer, non-uniform distribution of grains, thermal aspects, microstructure could play important role in determining the strength of machined component. Maksoud et al [43] investigated the surface and sub-surface cracks of ground ceramic. Lateral cracks and median cracks were identified after grinding with median cracks penetrates more into the workpiece. The results are shown in Figure 2.2.

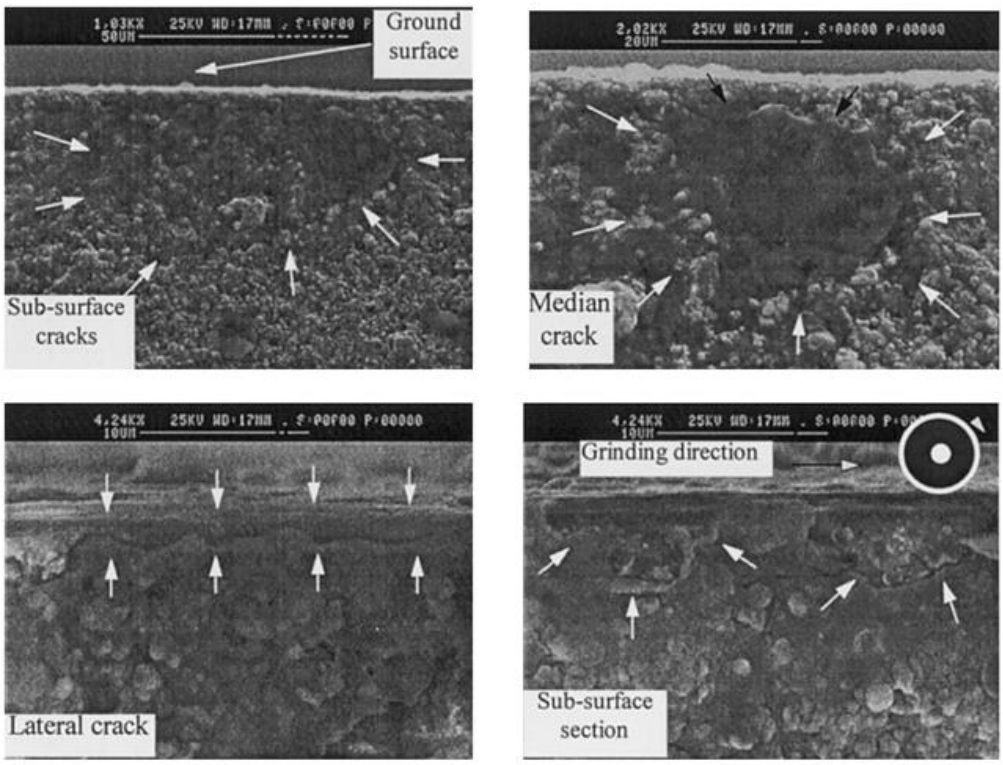

Figure 2.2 Surface and sub-surface cracks of ground ceramic [43]

It can be concluded from the above researches from machining approach that most of the grinding energy input is associated with ductile flow, even though material removal usually occurs by brittle fracture at large depth of cut. The material removal mechanism is combined with plastic flow at very low depth of cut and brittle fracture at larger engagement depth. Cracks have been observed at ground surface which indicates that grinding process has introduced surface damage to the ground workpiece.

2.2.2 Indentation Fracture Mechanics Approach

The indentation fracture mechanics approach likens abrasive-workpiece interactions for grinding of ceramic materials to localized small-scale indentation events. The fracture patterns under Vickers pyramidal indentor are characterized as a plastic deformation zone and two principal crack systems emanate from the plastic zone: median/radial and lateral cracks. This approach analyze the grinding process performance such as material removal rate and surface damage based on the investigations on the crack system from indentation fracture mechanics.

Lawn et al. [44] and Marshall et al. [45] developed a theory for describing the evolution of the median/radial crack system and lateral crack system for sharp-indenter contact. An expression for both lateral and median/radial crack size has been developed with respect to normal indentation load, indentor geometry and material properties. It provides theoretical basis for analyzing the surface damage in brittle materials from indentation fracture mechanics approach.

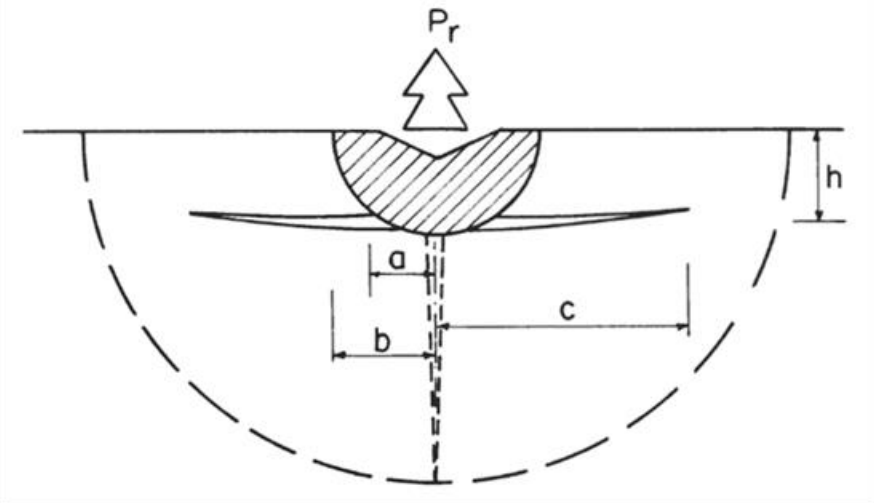

Figure 2.3 Lateral crack system. Broken lines indicate median/radial crack system [45]

Conway Jr. and Kirchner [46] investigated the elastic stress field due to both a normal force component and a tangential component. The tangential force was found to lead to increase tensile stresses normal to the direction of motion ahead of the contact point. This stress would cause initiation and propagation of median cracks beneath the tool.

Evans and Marshall [47] estimated the grinding material removal rate by the lateral crack size. This estimation correlates well with the experimental data for grinding of ceramics only at extremely small removal rates. Conway, Jr. and Kirchner [48] suggested crushing to be another mechanism for material removal in ceramic grinding. The analytical model successfully predicted the crushing depths for single point grinding of glass.

Malkin and Hwang [4] summarized previous researches from machining and indentation fracture mechanics approach. It is concluded that, the median/radial cracks are usually associated with strength degradation, and lateral cracks with material removal.

It is concluded that the indentation fracture analysis has provided important insights into abrasive-workpiece interaction, however, this approach has not been successfully applied to quantitatively describe the grinding process. It is pointed out that the grit geometry, multiple scratch interaction, stochastic distribution of grits, and elevated temperatures complicate the modeling effort.

The indentation fracture mechanics studies have provided a solid understanding of material removal mechanisms and crack generation and propagation under single grit load. However, the application of indentation fracture mechanics to realistic grinding conditions is not yet established. Due to the randomness of grinding process, a probabilistic approach must be pursued to accurately predict the surface characteristics such as surface finish, crack size and strength degradation in grinding process. However, a thorough model for predicting surface characteristics in ceramic grinding process with consideration of multiple random grit interactions is currently unavailable.

2.3 Summary

Based on literature reviews relating to residual stress modeling MQL grinding, limited information of MQL grinding process has been accumulated in this field, especially in the field of residual stress. A comprehensive investigation of residual stress behavior in MQL grinding is necessary. Although residual stress modeling in grinding process has been the subject of research for several decades, the majority of the work focused on FEM models, which require great computational expense. So there is a need to develop an analytical model capable of predicting residual stresses from process

condition inputs such as process parameters, wheel characteristics, workpiece properties and lubrication parameters.

In the area of ceramic grinding, extensive research has been conducted to characterize the material removal mechanism as well as grinding induced damages. The indentation studies have shown great potential in the application to ceramic grinding process. However, the implementation of indentation fracture mechanics models to quantitatively describe the ceramic grinding process performance in terms of surface finish or strength degradation has not be accomplished yet.

To address these issues, this dissertation consists of the following tasks:

(1) Force modeling in MQL grinding process and validation,

(2) Temperature modeling in MQL grinding process and validation,

(3) Residual stress modeling in MQL grinding process and validation,

(4) Surface roughness and strength degradation modeling in ceramic grinding and validation,

(5) Discussion of the effect of process conditions on MQL grinding residual stress and the surface fracture in ceramic grinding.

CHAPTER 3

FORCE MODELING IN MQL GRINDING

Force modeling in grinding has been the subject of research for many years. Some early grinding force models [3, 36] are composed of a physical part which includes the speed ratio, the workpiece engagement and the equivalent diameter, as well as an empirical addition which figures in the basic model as a constant for the grinding wheel and a constant for the workpiece. Hecker [49] have developed an analytical grinding force model based on chip thickness analysis. This model taken into account of probabilistic distribution of cutting edges of the wheel surface and single grit forces. However, some over simplification of single grit interaction analysis is noticed. The goal of the current research is to develop a more accurate cutting force model incorporating MQL effect based on single grit interaction analysis and undeformed chip thickness probabilistic distribution approach.

The single grit forces in the present model are decomposed as chip formation, ploughing and rubbing forces according to Malkin [3]. These three force components contribute to the overall single grit forces. The mechanism for minimum quantity lubrication is first discussed and the friction coefficient between the grit and the workpiece is calculated based on the boundary lubrication model presented by Kato et al [50]. The distribution of undeformed chip thickness is then analyzed based on Hecker's analytical approach [49]. The total grinding force is formulated as an integration of the

single grit forces over the undeformed chip thickness spectrum. Each aspect of the grinding force model is described in the following sections.

3.1 MQL Lubrication Mechanism and Friction Coefficient Prediction

In order to build the force model from an analytical approach, the effect of MQL lubricant on the tribological behavior must be first investigated. In grinding process, the contact zone is characterized by high pressure, speed and temperature which makes it very difficult for the fluid to effectively lubricate the wheel-workpiece contact surface. According to Godlevski [51], the penetration process of cutting fluids in conventional flood cooling machining involves (a) liquid phase penetration (b) micro-droplet evaporation and (c) gaseous phase filling of the capillary. In high speed machining process like grinding, when the filling time of the capillary is longer than the contact time between a cutting edge and the workpiece, the lubricant film couldn't be effectively formed and thus the lubrication effect is limited.

Different from conventional flood cooling, the air-oil mixture was directly applied to the contact zone with high speed jet in MQL grinding. The capillary filling action does not require liquid phase penetration and evaporation, thus the filling time is much shorter than conventional flood cooling which indicates more efficient lubrication. For example, the capillary filling time of water vapor lubrication is one magnitude smaller than that of water lubrication [52]. Besides, the air-oil mixture jet direction and position could be tuned to achieve optimal performance in MQL grinding. That explains why the MQL lubricant could achieve similar or even better lubrication effect comparing to conventional flood cooling.

As we know, the contact pressure between the cutting grits and the workpiece is very high and also due to the limited amount of lubricant, the lubricant film cannot be fully established. Therefore, the boundary lubrication theory is a more proper description of the lubrication condition instead of hydrodynamic lubrication. In boundary lubrication, part of the load is carried by the metallic contacts between asperities on both surfaces and the other part is carried by adsorbed lubricant film contact as shown in Figure 3.1.

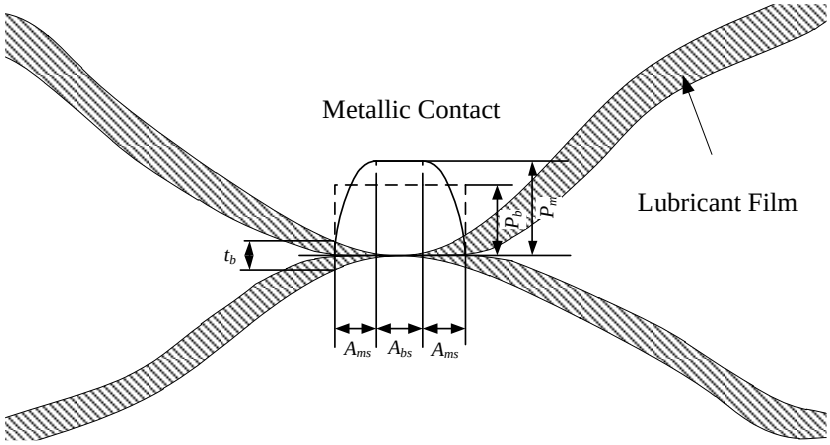

Figure 3.1 Boundary lubrication mechanism

The friction force and the normal load in boundary lubrication can be expressed as:

$$F = s_m A_m + s_b A_b, \qquad N = p_m A_m + p_b A_b \tag{3.1}$$

in which the metallic contact area A_m and the adsorbed lubricant film contact area A_b are calculated as follows according to the model presented by Kato et al. [50]:

$$A_m = \frac{\pi R_t n_0 D_i^2 a_s^3}{6H_{\max}^2},$$
$$A_b = \frac{\pi R_t n_0 D_i^2 \left[\left(a_s + t_b \right)^3 - a_s^3 \right]}{6H_{\max}^2} \tag{3.2}$$

in which R_t is asperity tip radius, n_0 is total asperity number, D_i is inclination distribution function, a_s is the approach of two surfaces, $H_{\max}$ is asperity height distribution, and t_b is effective adsorbed lubricant film thickness.

The friction coefficient is calculated as:

$$\mu = \frac{F}{N} = \frac{s_m A_m + s_b A_b}{p_m A_m + p_b A_b} = \frac{C_1 A_m + C_2 C_3 A_b}{A_m + C_2 A_b} \tag{3.3}$$

where

$$C_1 = \frac{s_m}{p_m}, \quad C_2 = \frac{p_b}{p_m}, \quad C_3 = \frac{s_b}{p_b} \tag{3.4}$$

where s_b, p_b and s_m, p_m are the shear strength and yield pressure at the adsorbed lubricant film contact area and the metallic contact area respectively.

Substituting (3.2) into (3.1), the approach of two surfaces a_s can be estimated from the cubic function:

$$a_s^3 + 3C_2 t_b a_s^2 + 3C_2 t_b^2 a_s + \left[C_2 t_b^3 - N / \left(p_m Q \right) \right] = 0 \tag{3.5}$$

where

$$Q = \pi R n_0 D^2 / \left(6H_{\max}^2 \right) \tag{3.6}$$

From (3.2), (3.3), and (3.5), the friction coefficient between the grinding grit and workpiece can be calculated as:

$$\mu = \frac{\left(C_1 a_s^3 + C_2 C_3 \left\{\left(a_s + t_b\right)^3 - a_s^3\right\}\right)}{\left(a_s^3 + C_2\left[\left(a_s + t_b\right)^3 - a_s^3\right]\right)} \tag{3.7}$$

It is noticed that the adsorbed lubricant film thickness t_b equals to zero is corresponding to the dry grinding condition. Setting t_b=0, (3.7) becomes:

$$\mu = C_1 \tag{3.8}$$

Here, the coefficient C_1 represents the friction coefficient in completely dry grinding condition. At low depth of cut since as in grinding situation, the coefficient of friction is sensitive to the ratio of engagement depth to the tool nose radius. There are different models to estimate the friction coefficient under this condition. Sin and Suh [53] proposed a model of a sliding spherical hard particle, and the friction coefficient could be estimated by:

$$\mu = \frac{2}{\pi}\left\{\left(\frac{w}{2r}\right)^{-2} \sin^{-1}\left(\frac{w}{2r}\right) - \left[\left(\frac{w}{2r}\right)^{-2} - 1\right]^{\frac{1}{2}}\right\} \tag{3.9}$$

where w is the width of indentation and r is the spherical grit radius. Bhushan [54] proposed the friction model of a sliding cylinder. It is given as:

$$\mu = \left[\frac{1}{2(r/t_0) - 1}\right]^{\frac{1}{2}} \tag{3.10}$$

where r is the cylinder radius and t_0 is the depth of cut. In this study, these two different models will be compared. The coefficients C_2, C_3 and other parameters are determined from experimental data and material properties. They will be further discussed in Section

6.2. The friction coefficient calculated will be implemented in the single grit interaction modeling calculations.

3.2 Single Grit Interaction Model

Grinding is typically characterized by the multiple cutting points with large negative rake angle removing materials at very high strain rate. A stochastic treatment of the cutting edge geometry and distribution is necessary [49]. In this study, the grit shape is assumed to be conical with a rounded tip. A wear flat area at the bottom of the grit may develop during the grinding process.

To describe the single grit interaction, a common three stages assumption [3] is employed here. The single grit force is thus calculated from three components – chip formation, ploughing and rubbing force. The rubbing force and ploughing force are dominant when the engagement depth of individual grit is very small. The chip formation only takes place when the undeformed chip thickness has reached a critical value [55].

Assuming that the single grit cutting process is orthogonal and treating the created chip as a series of elements with infinitesimal width, the individual grit grinding is simplified to a 2-D material removal process involving chip formation, ploughing and rubbing, as shown in Figure 3.2.

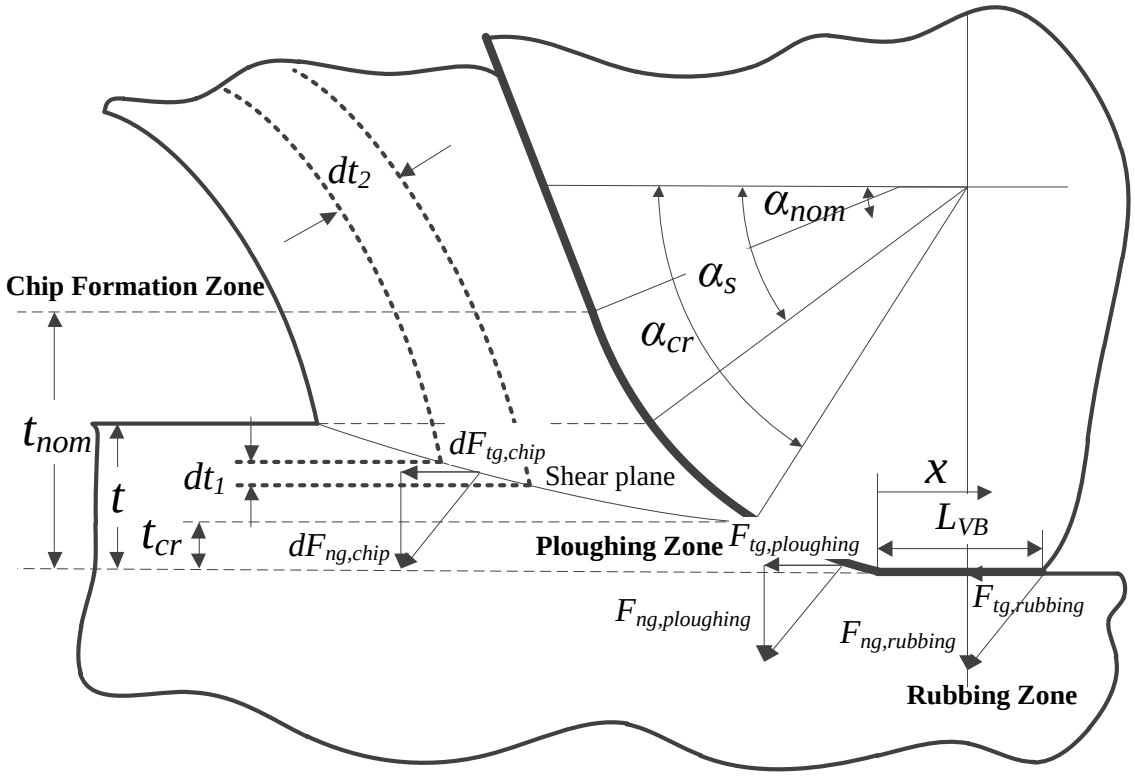

Figure 3.2 Single grit interaction illustration

Notice that all the rake angles here have negative values. The critical rake angle α_{cr} corresponds to the critical undeformed chip thickness t_{cr}. Ikawa et al. [56] suggested that the critical undeformed chip thickness may be at the order of 1/10 of the cutting edge radius. Basuray et al. [57] predicted the stagnation point to be equal to 37.6°. In this study, the critical undeformed chip thickness is experimentally calibrated.

When undeformed chip thickness t is larger than t_{cr}, the material removal mechanism is chip formation. When t reaches t_{nom}, the rake angle will be equal to the nominal rake angle which is calculated from the grit cone angle. This micro-cutting mechanism can be represented by applying the Merchant model to each of the infinitesimal elements. The incremental chip formation force can be expressed as:

$$dF_{tg,chip} = \frac{\tau b \cos(\beta - \alpha)}{\sin\phi \cos(\phi + \beta - \alpha)} dt_1,$$
$$dF_{ng,chip} = \frac{\tau b \sin(\beta - \alpha)}{\sin\phi \cos(\phi + \beta - \alpha)} dt_1 \tag{3.11}$$

where τ is the workpiece material flow stress, b is the local cutting width, β is friction angle, α is local rake angle, ϕ is local shear angle. The local shear angle and local rake angle are related by cutting ratio rc given in (3.12). The shear angle could be found from measurements of cut chip thickness t_c.

$$rc = \frac{t_c}{t} = \frac{\sin(\phi)}{\cos(\phi - \alpha)} \tag{3.12}$$

The friction angle is calculated from the friction coefficient in boundary lubrication:

$$\beta = \tan^{-1}(\mu) \tag{3.13}$$

From geometrical relationship,

$$dt_1 = r\cos\alpha d\alpha \tag{3.14}$$

The local width of cut for each individual grain is:

$$b = 2r\cos\alpha, \text{ if } t < t_{nom};$$
$$b = 2\left(r\cos\alpha_{nom} + \frac{t - t_{nom}}{\tan(-\alpha)} \right), \text{ if } t > t_{nom} \tag{3.15}$$

By integration of the incremental tangential and normal forces per unit width in the two dimensional simplified configuration, the chip formation force of each grit is calculated. The total tangential and normal force can thus be expressed as:

When $t < t_{nom}$,

$$
\begin{aligned}
F_{tg,chip} &= \int_{\alpha_{cr}}^{\alpha_s} \frac{\tau \cos(\beta-\alpha)}{\sin\phi\cos(\phi+\beta-\alpha)} 2r^2\cos^2\alpha d\alpha \\
F_{ng,chip} &= \int_{\alpha_{cr}}^{\alpha_s} \frac{\tau \sin(\beta-\alpha)}{\sin\phi\cos(\phi+\beta-\alpha)} 2r^2\cos^2\alpha d\alpha
\end{aligned}
\tag{3.16}
$$

When $t > t_{nom}$,

$$
\begin{cases}
F_{tg,chip} = \int_{\alpha_{cr}}^{\alpha_{nom}} \frac{\tau \cos(\beta-\alpha)}{\sin\phi\cos(\phi+\beta-\alpha)} 2r^2\cos^2\alpha d\alpha \\
\qquad + \int_{t_{nom}}^{t} \frac{2\tau\left(r\cos\alpha_{nom} + \left(t-t_{nom}\right)/\tan(-\alpha)\right)\cos(\beta-\alpha_{nom})}{\sin\phi\cos(\phi+\beta-\alpha_{nom})} dt_1 \\
F_{ng,chip} = \int_{\alpha_{cr}}^{\alpha_{nom}} \frac{\tau \sin(\beta-\alpha)}{\sin\phi\cos(\phi+\beta-\alpha)} 2r^2\cos^2\alpha d\alpha \\
\qquad + \int_{t_{nom}}^{t} \frac{2\tau\left(r\cos\alpha_{nom} + \left(t-t_{nom}\right)/\tan(-\alpha)\right)\sin(\beta-\alpha_{nom})}{\sin\phi\cos(\phi+\beta-\alpha_{nom})} dt_1
\end{cases}
\tag{3.17}
$$

In the grinding process, the workpiece is subjected to deformation at high strains and strain rates and sometimes high temperature. To incorporate these effects, the calculation of strain and strain rate in single grit interaction is important. The model based on slip line analysis in machining with an edge-rounded tool proposed [58] has been applied to calculate the strain and strain rate in this study due to the similarity between a single grit and edge-rounded tool. The schematic for the slip line analysis is shown in Figure 3.3.

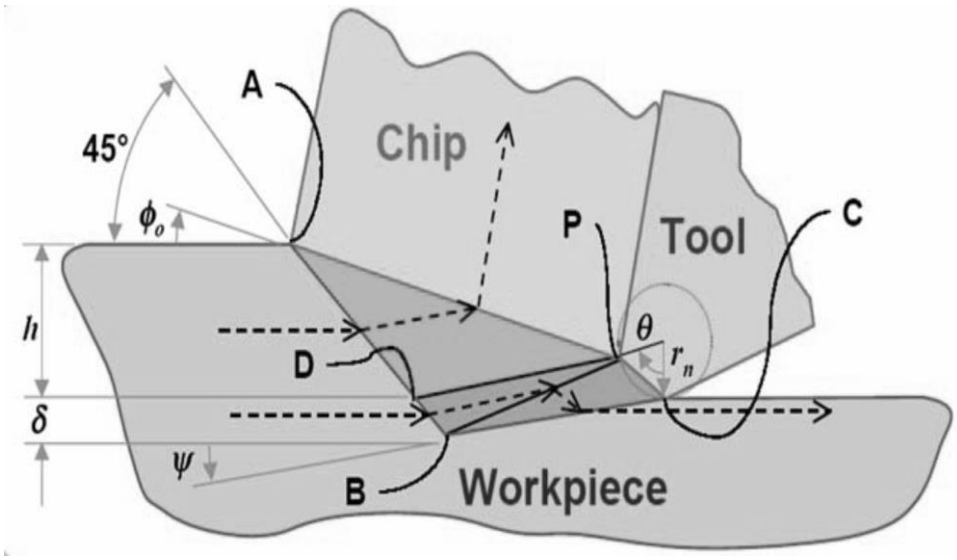

Figure 3.3 Geometric model of the cutting process with an edge radius tool [58]

In this model, the strain for the deformation zone is obtained from the strains imposed in the chip and the work weighted by their respective deformation volumes, given as:

$$\varepsilon = \frac{1}{\sqrt{3}}\left(\frac{\upsilon_{chip}\gamma_{chip}}{\upsilon_{chip}+\upsilon_{work}} + \frac{\upsilon_{work}\gamma_{work}}{\upsilon_{chip}+\upsilon_{work}} \right) \tag{3.18}$$

The shear strains for the chip and the workpiece are given by:

$$\gamma_{chip} = \frac{\sqrt{2}\sin(\theta_{PD})}{\sin(\frac{\pi}{4}+\theta_{PD})} + \frac{\cos(\gamma_{avg}+\theta_{PD})}{\cos(\gamma_{avg}-\phi)\sin(\phi+\theta_{PD})} \tag{3.19}$$

$$\gamma_{work} = \frac{\sqrt{2}\sin(\theta_{PD})}{\sin(\frac{\pi}{4}+\theta_{PD})} + \frac{\sin(\theta_{PD}+\frac{\theta}{2})}{\cos(\theta_{PD}+\frac{\pi}{2})\sin(\theta_{PD}+\theta_{PB})} + \frac{\sin(\frac{\theta}{2})}{\sin(\psi)\sin(\psi+\frac{\theta}{2})} \tag{3.20}$$

where υ_{chip} and υ_{work} is the volume of the chip and workpiece deformation zone, γ_{avg} is the average rake angle, θ_{PD} is the inclination angle of PD, θ_{PB} is the inclination angle of

PB, ψ is the inclination angle of BC as shown in Figure 3.3. These parameters could be calculated by geometrical relationships based on the tool radius, undeformed chip thickness and cutting ratio [58].

Similarly, the strain rate is calculated from the strain rate in chip and work zone by a weighting function:

$$\dot{\varepsilon} = \frac{1}{\sqrt{3}}\left(\frac{\upsilon_{chip}\dot{\gamma}_{chip}}{\upsilon_{chip}+\upsilon_{work}} + \frac{\upsilon_{work}\dot{\gamma}_{work}}{\upsilon_{chip}+\upsilon_{work}} \right) \tag{3.21}$$

The strain rates of the chip and workpiece deformation are given as:

$$\dot{\gamma}_{chip} = 2V \frac{\gamma_{chip}}{\sqrt{2}\sin(\frac{\pi}{4}+\theta_{PD})\overline{\mathrm{PD}}} \tag{3.22}$$

$$\dot{\gamma}_{work} = 2V \frac{\gamma_{work}}{\sqrt{2}\sin(\frac{\pi}{4}+\theta_{PD})\overline{\mathrm{PD}} + \frac{\sin(\psi+\theta/2)}{\sin\psi}\overline{\mathrm{P}C}} \tag{3.23}$$

where V is the cutting velocity, $\overline{\mathrm{PD}}$ is the length of PD, and $\overline{\mathrm{PC}}$ is the length of PC. The strain and strain rate calculations will be incorporated in the Johnson-Cook model to calculate the flow stress of the workpiece during grinding as described in section 4.3.

The workpiece material below critical undeformed chip thickness is plastically deformed in front of the grit without chip formation. This phenomenon is referred to as the ploughing effect. Shaw [59] adapted a Brinell indentation hardness test to describe this mechanism since the behavior of material beneath a Brinell ball resembles the material deformation below a grit with a rounded tip as shown in Figure 3.4.

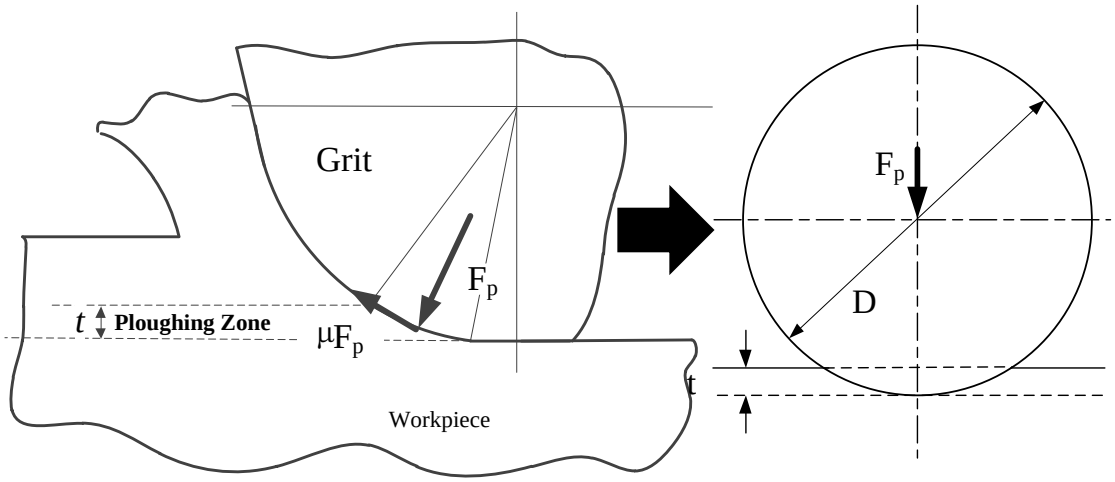

Figure 3.4 Brinell hardness test resemblance of ploughing force

The Brinell hardness number, HB, is defined as the ratio of the load to the curved area of indentation:

$$HB = \frac{F_p}{\pi D t} \tag{3.24}$$

where F_p is the indentation force.

In the grinding process, the plastically deformed zone by the singe grit rotates in the direction of movement. Therefore, the ploughing force can be calculated from the indentation force acting in the direction of half of the critical rake angle with respect to the normal direction. Additionally, a friction force between the grit and the workpiece is generated due to the relative movement. The tangential and normal ploughing forces per grit can thus be estimated by considering the indentation effect and the friction reaction as:

$$\begin{aligned} F_{tg,ploughing} &= F_p\left(\sin\left(\frac{\alpha_{cr}}{2}\right) + \mu\cos\left(\frac{\alpha_{cr}}{2}\right)\right), \\ F_{ng,ploughing} &= F_p\left(\cos\left(\frac{\alpha_{cr}}{2}\right) + \mu\sin\left(\frac{\alpha_{cr}}{2}\right)\right) \end{aligned} \tag{3.25}$$

The rubbing force is caused by the elastic or elastic-plastic contact of grit wear flat area with the workpiece surface [3]. Experimental investigations proved that the grinding force varies with different wear area [60]. In most of the grinding force models [61, 62, 63], the rubbing forces are calculated from friction coefficient, contact pressure and wear area. However, there models are based on the empirical relationship between average contact pressure and difference in radius of curvature [64]. This study proposed an analytical approach to estimate the normal and shear stress in the wear flat area adapted from calculation of cutting force of worn tool [11]. The forces in the grinding direction $F_{tg,rubbing}$ and in the normal direction $F_{ng,rubbing}$ can be calculated by integrating the normal stress and shear stress, respectively.

$$\begin{aligned} F_{tg,rubbing} &= b\int_0^{L_{VB}} \sigma_w(x)\,dx, \\ F_{ng,rubbing} &= b\int_0^{L_{VB}} \tau_w(x)\,dx \end{aligned} \tag{3.26}$$

where

$$\begin{aligned} &\sigma_w(x) = \sigma_0\left(\left(L_{VB}-x\right)/L_{VB}\right)^2 \quad \text{for} \quad 0 < x < L_{VB} \\ &\tau_w(x) = \tau_0 \quad \text{for } 0 < x < L_{VB}\left(1-\sqrt{\tau_0/\sigma_0}\right) \\ &\tau_w(x) = \mu\sigma_w(x) \quad \text{for } L_{VB}\left(1-\sqrt{\tau_0/\sigma_0}\right) < x < L_{VB} \end{aligned} \tag{3.27}$$

where L_{VB} is the wear flat length as shown in Fig 1. The flow stresses σ_0 and τ_0 are given in Waldorf's worn tool force model [11].

The total single grit forces in the tangential and normal directions are the summations of the forces due to chip formation, ploughing, and rubbing, that is:

$$\begin{aligned} F_{tg} &= F_{tg,chip} + F_{tg,ploughing} + F_{tg,rubbing}, \\ F_{ng} &= F_{ng,chip} + F_{ng,ploughing} + F_{ng,rubbing} \end{aligned} \tag{3.28}$$

When the undeformed chip thickness is smaller than critical undeformed chip thickness, only ploughing and rubbing forces contribute to the single grit force. After the critical undeformed chip thickness is reached, chip formation force increases rapidly and become the dominant factor at large undeformed chip thickness. Since not all the grit have same engagement depth, the information of undeformed chip thickness distribution is necessary here to solve for the average single grit force.

3.3 Distribution of Undeformed Chip Thickness

Due to the randomness of grit distribution on the wheel surface, grits will have different engagement depths in the grinding process which result in different single grit forces. To calculate the average single grit force, it is necessary to know the distribution of undeformed chip thickness. This distribution was described by a Rayleigh probability density function (p.d.f.) [65].

$$f(t) = \begin{cases} \left(t / \sigma^2\right) \exp\left(-t^2 / 2\sigma^2\right) & t \geq 0 \\ 0 & t < 0 \end{cases} \tag{3.29}$$

The expected value and variance is expressed as:

$$\begin{aligned} E(t) &= \sqrt{\pi / 2}\sigma \\ sd(t) &= \sqrt{0.429}\sigma \end{aligned} \tag{3.30}$$

The parameter σ, that completely defines this p.d.f., was calculated as a function of the grinding wheel microstructure (grain shape, static grit density), dynamic effects (local grain deflection and wheel-workpiece contact deflection), and grinding conditions (wheel depth of cut, wheel and workpiece tangential velocity):

$$\sigma = \sqrt{\frac{aV_w}{2V_s l_c C_d \tan(\theta)}} \tag{3.31}$$

where a is wheel depth of cut, V_s is wheel speed, V_w is workpiece speed, l_c is the real contact length due to wheel-workpiece contact deformation, and C_d is the dynamic grit density.

The workpiece and tool deflection can produce a change in the real length of the contact zone as shown in Fig. 20. Rowe et al. [66] proposed a real contact length model given as:

$$l_c = \left(a d_s + 8 R_r^{\,2} F_n' d_s \left(K_s + K_w \right) \right)^{1/2} \tag{3.32}$$

where d_s is the wheel diameter, F_n' is the normal force per contact length, R_r is a constant that represents the roughness of the surfaces in contact. A good agreement between predicted and experimental contact lengths was found by the author using $R_r = 5$. K_s and K_w are the wheel and workpiece elasticity, respectively. They are calculated as:

$$K_i = \frac{1 - \nu_i^2}{\pi E_i} \qquad i = s(wheel), w(workpiece) \tag{3.33}$$

where E_i is the modulus of elasticity and ν_i is the Poisson's ratio for the wheel and the workpiece material.

In order to calculate dynamic grit density C_d , static grit density should be obtained first. The static grit density could be estimated from direct measurement on the wheel surface, with a general expression as:

$$C_s = A z^k \tag{3.34}$$

where z is the radial distance measured into the wheel, the adjusted parameters A and k depend on the grit number, wheel type and dressing conditions. The measurement technique will be discussed in section 6.1. The dynamic grit density which depends on static number of cutting edges and also the on the kinematic and dynamic grinding conditions is calculated by [49] and is given as:

$$C_{d(z^*)} = \frac{C_{s(z^*)}}{1 + \frac{C_{s(z^*)}}{4} \frac{\tan(\theta)}{\tan(\varepsilon_z)} \frac{\sigma^3}{z^*}} \tag{3.35}$$

where the radial distance into the wheel, z^*, is equal to the maximum value of the undeformed chip thickness that could be approximated by:

$$z^* = E(t) + 3sd(t) \tag{3.36}$$

The parameter $\tan(\varepsilon_z) = 2V_w a / V_s d_e$ reflects the kinematic effects where d_e is the equivalent wheel diameter. The modeling details can be found in Hecker's work [6, 67].

Two regions of interest separated by the critical undeformed chip thickness t_{cr} can be observed, i.e., the rubbing and ploughing region and the chip formation region as shown in Figure 3.5. It is important to remark that what here is referred to as the undeformed chip thickness is actually the depth of engagement of each individual active grit regardless of whether it is ploughing or removal material. The Rayleigh distribution has the advantage of being uniquely defined by only one parameter σ.

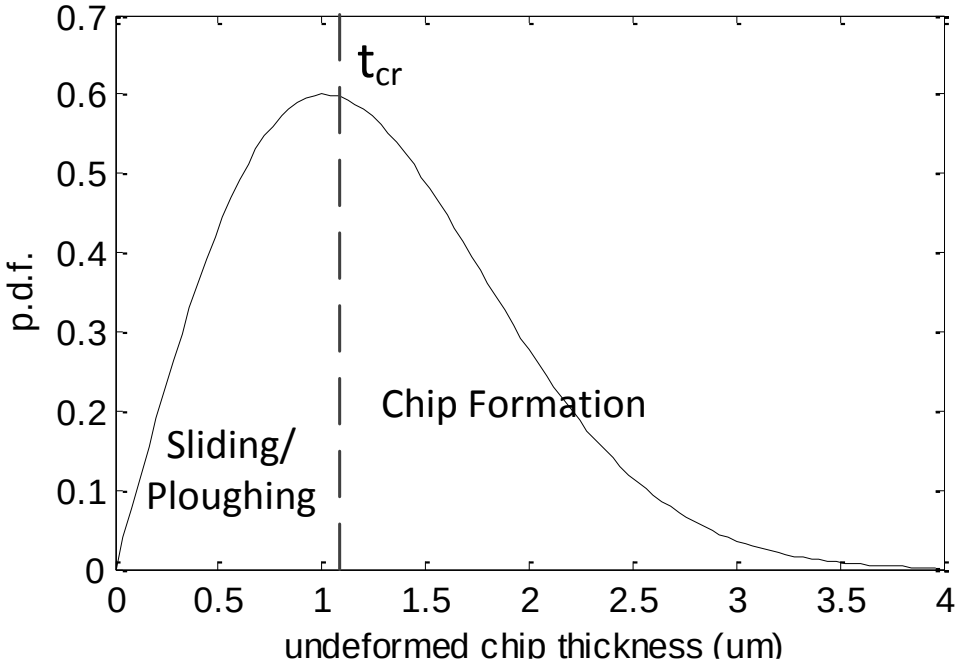

Figure 3.5 Schematic of undeformed chip thickness distribution

With the undeformed chip thickness distribution, the average single grit force or expectation of single grit force distribution are calculated by integration:

$$\begin{cases} E(F_{tg}) = \int_0^\infty f(t)F_{tg}(t)dt \\ E(F_{ng}) = \int_0^\infty f(t)F_{ng}(t)dt \end{cases} \tag{3.37}$$

The total grinding forces are then calculated as multiplication of average single grit force and the number of active cutting edges:

$$\begin{cases} F_t = C_d w l_c E(F_{tg}) \\ F_n = C_d w l_c E(F_{ng}) \end{cases} \tag{3.38}$$

where F_t is the total tangential grinding force, F_n is the total normal grinding force, and w is the grinding width.

3.4 Summary

This chapter presented the modeling technique for grinding forces under minimum quantity lubrication. Section 3.1 describes the mechanism of MQL lubrication and the calculation of friction coefficient under MQL condition. Boundary lubrication theory has been applied to model the tribological behavior in the contact zone between the workpiece and cutting edges.

Section 3.2 presents the single grit force model based on the interaction between individual grit and the workpiece. Three force components have been taken into account: chip formation force, ploughing force, and rubbing force. The single grit forces served as the basis for determining the mechanical loading stresses.

Section 3.3 introduces the grinding kinematics and dynamics modeling for extrapolating the single grit interaction to multiple grit interactions. The probabilistic distribution of undeformed chip thickness is used to calculate the average single grit forces and the dynamic grit density is calculated for accurate prediction of total grinding forces.

The grinding energy input resulted from grinding forces transformed into heat generation in the contact zone which will result in a temperature rise. In the following chapter, the modeling technique for grinding temperature is introduced. Followed by the residual stress modeling based on mechanical and thermal loading stresses calculated from grinding forces and temperature distribution.

CHAPTER 4

TEMPERATURE MODELING IN MQL GRINDING

In this chapter, a complete thermal analysis of MQL effect in grinding process is developed. As noted previously grinding is a process with very high specific energy. Virtually all of this energy is dissipated as heat. The heat in grinding is generated in the contact zone and conducted into the workpiece. Most of the temperature distribution models in grinding are based on Jaeger's moving heat source model [68]. Modifications of the model include the change of heat flux distribution. A triangular flux is approximate where the volume of chips is proportional to the depth of cut for grinding. The experiments results of measured grinding temperatures [69] supported this triangular flux approximation. The solution for moving heat source elements can be represented by Bessel functions by summing over the length of the contact surface.

4.1 Temperature Distribution in the Workpiece

The moving heat source model is used to calculate the temperature distribution in the workpiece. Considering the heat input, there have been many discussions about the heat flux distribution. Early assumptions of a uniform heat distribution are not supported by temperature measurements. According to Rowe [70], triangular heat distribution should be used to avoid significant errors. In this work, a triangular heat source moving along the grinding direction and an additional uniform heat loss from MQL effect is

modeled. The schematic diagram and coordinate system of temperature calculation is shown in Figure 4.1.

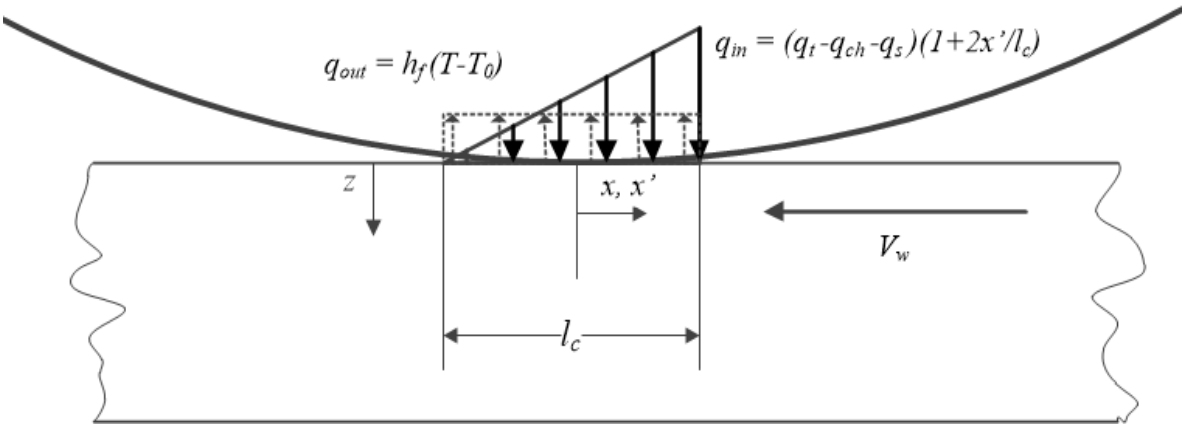

Figure 4.1 Temperature Modeling Schematic

The solution for the moving heat source can be represented by Bessel functions and obtained by summing over the length of the contact zone. The temperature at any point (x,z) in the workpiece is given as [70]:

$$T_{(x,z)} = \int_{-l_c/2}^{l_c/2} \frac{q_{in} - q_{out}}{\pi k_w} \exp\left(\frac{V_w(x-x')}{2\alpha_w}\right) K_0 \left\{ \frac{V_w\left[(x-x')^2 + z^2\right]^{1/2}}{2\alpha_w} \right\} dx' \qquad (4.1)$$

where q_{in} is the total heat flux into the workpiece and fluid given as:

$$q_{in} = (q_t - q_{ch} - q_s)(1 + 2x'/l_c) \qquad (4.2)$$

and q_{out} is the heat flux taken away by fluid given as:

$$q_{out} = h_f (T - T_0) \qquad (4.3)$$

Here k_w is the thermal conductivity of the workpiece, α_w is the thermal diffusivity given by $\alpha_w = k_w / \rho_w c_w$, where ρ_w is the workpiece density, c_w is the

workpiece specific heat, and K_0 is the modified Bessel function of the second kind of order zero. In order to calculate the temperature distribution in the workpiece, the next step is to calculate q_{in} and q_{out} from energy partition analysis.

4.2 Energy Partition in MQL Grinding

In grinding process, the total heat in the contact zone flow into four heat sinks: the workpiece, the wheel, the chips and the fluid as shown in Figure 4.2.

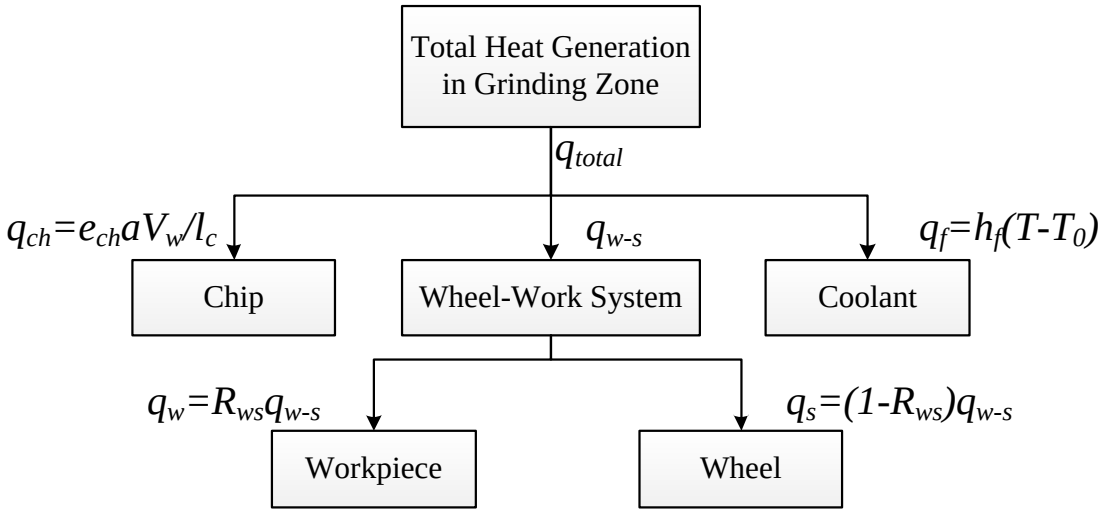

Figure 4.2 Heat flux partitioning during grinding

The total heat flux generated in the grinding zone is conducted into these mediums:

$$q_t = q_w + q_s + q_{ch} + q_f \tag{4.4}$$

The total heat flux is calculated from the grinding power as:

$$q_t = F_t V_s / (w l_c) \tag{4.5}$$

where w is grinding width. So, partition ratios can be defined as the proportions of these fluxes to the total flux. Based on the Hahn partitioning model for a grain sliding on a workpiece [71], a "workpiece-wheel" partition ratio, R_{ws} is defined as:

$$R_{ws} = q_w / (q_w + q_s) = \left(1 + 0.97 k_g / \left(\sqrt{k_w \rho_w c_w}\sqrt{r_0 V_s}\right)\right)^{-1} \tag{4.6}$$

where k_g is the grain thermal conductivity, r_0 represents an effective radius of contact of the abrasive grains, here it is assumed to be equal to the grain tip radius. The ratio R_{ws} remains reasonably constant for a particular abrasive material and workpiece material, whereas the heat flux q_w entering the workpiece, taking account of the chips and fluid is highly variable. Based on arguments by [3], the flux to the chips is assumed to be close to the limiting chip energy e_{ch}. For ferrous materials, this value is 6.21 J/mm^2. The flux convected by the chips is the rate of chip energy divided by the area of the grinding contact and is therefore:

$$q_{ch} = e_{ch} a V_w / l_c \tag{4.7}$$

To estimate the heat flux entering workpiece, the last step is the estimation of fluid convection. The heat flux taken by the MQL/fluid out of the contact zone is:

$$q_f = h_f (T - T_0) \tag{4.8}$$

where h_f is the convection heat transfer coefficient of MQL/fluid, T_0 is the ambient temperature, T is the workpiece temperature. For estimation of h_f in conventional flood cooling, Kim et al. [72] estimated values of 20000 ahead and 15000 W/m^{2}K behind the grinding zone for downfeed creep grinding at relatively low temperatures. Rowe [70] estimated the values of 10000 W/m^{2}K for oil-in-water emulsion, and 4000 W/m^{2}K for

neat oils. Hadad and Sadeghi [22] measured a value of 43400 W/m^{2}K for water-based coolants; for MQL fluid, a value of 1400 to 1630 W/m^{2}K is obtained for different sets of MQL parameters. To analytically estimate the heat transfer coefficient, Hadad and Sadeghi [22] proposed a spraying cooling convection heat transfer model and considered the vaporization effect to estimate the heat transfer coefficient change from the trailing edge to the leading edge in MQL grinding. In this study, the convection effect is considered as a fluid flow passing through parallel flat surfaces. The average heat transfer coefficient in the above equation can be estimated by the semi empirical model [73]:

$$Nu = h_f l_c / k_f = 0.664 Pr^{1/3} Re^{1/2} \tag{4.9}$$

$$Pr = \mu_f c_f / k_f \tag{4.10}$$

$$Re = u_f \rho_f l_c / \mu_f \tag{4.11}$$

where Nu is the Nusselt number, Pr is the Prandtl number, and Re is the Reynolds number, k_f is the thermal conductivity, μ_f is the dynamic viscosity, c_f is the specific heat capacity, u_f is the velocity of the fluid and ρ_f is the density of fluid.

To estimate the MQL properties, a homogeneous two-phase flow is assumed here since the fluid drops have very high velocity and pressure [22]. In the homogeneous two-phase flow model, the air-oil mixture is considered as a single-phase flow with homogenous properties. The density, dynamic viscosity, thermal conductivity and specific heat capacity of the two-phase flow can be expressed as:

$$\rho_f = \left(\frac{\bar{\chi}}{\rho_g} + \frac{1-\bar{\chi}}{\rho_l} \right)^{-1} \tag{4.12}$$

$$\mu_f = \left(\frac{\bar{\chi}}{\mu_g} + \frac{1-\bar{\chi}}{\mu_l} \right)^{-1} \tag{4.13}$$

$$k_f = \left(\frac{\bar{\chi}}{k_g} + \frac{1-\bar{\chi}}{k_l} \right)^{-1} \tag{4.14}$$

$$c_f = \left(\frac{\bar{\chi}}{c_g} + \frac{1-\bar{\chi}}{c_l} \right)^{-1} \tag{4.15}$$

where gas weight fraction is given as:

$$\bar{\chi} = \frac{\rho_g \dot{V}_g}{\rho_g \dot{V}_g + \rho_l \dot{V}_l} \tag{4.16}$$

where $\dot{V}_g$ and $\dot{V}_l$ are the volumetric flow rate of air and oil. The volume metric flow rate of the air could be calculated from the air velocity and nozzle cross sectional area as:

$$\dot{V}_g = v_g \pi \left(\frac{d_{nozzle}}{2} \right)^2 \tag{4.17}$$

The air velocity is related to air pressure by Bernoulli Principle:

$$P_g = \frac{\rho_g v_g^2}{2} \tag{4.18}$$

The volumetric flow rate of the oil is controlled by the MQL supply system. Then the thermal properties of the gaseous-liquid two-phase flow could be estimated from the properties of the air and oil. The fluid velocity u_f could be different at the entering and exiting area of the contact zone. The entering velocity of fluid velocity is approximated by the average of the wheel speed and the jet speed, the exiting velocity is assumed to be equal to the wheel speed. The average Reynolds number in the contact zone is estimated based on the average of entering and exiting velocity. After calculating the Reynolds

number, Prandtl number and Nusselt number, the average heat transfer coefficient in the grinding zone could be calculated based on (4.9).

After the heat partition analysis been completed, the temperature distribution in the workpiece could be calculated. A typical temperature profile below the ground surface is shown in Figure 4.3. The exact temperature profile depends on the cutting parameters and the thermal properties of the workpiece material.

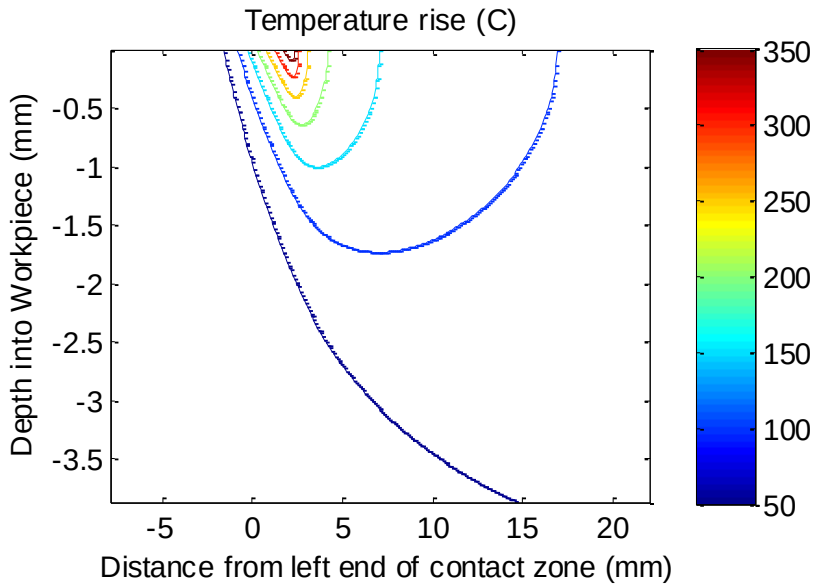

Figure 4.3 Temperature distribution in workpiece

4.3 Grinding Force and Temperature Coupling

Grinding process is usually associated with high temperature, strain and strain rate. The material behavior, especially the flow stress, is sensitive to these conditions. To incorporate strain, strain rate and temperature influences, the Johnson-Cook model is applied to calculate the flow stress on the shear plane in the grinding process.

$$\sigma = \left(A + B\varepsilon_p^n\right)\left(1 + C\ln\left(\frac{\dot{\varepsilon}_p}{\dot{\varepsilon}_0}\right)\right)\left(1 - \left[\frac{\left(T - T_r\right)}{\left(T_m - T_r\right)}\right]^m\right) \tag{4.19}$$

The terms *A*, *B*, *C*, *m*, *n*, and $\dot{\varepsilon}_0$ are material constants. Strain and strain rate calculation for grinding process are given in section 3.2. The temperature effect to the flow stress is incorporated in an iterative manner since the force calculation will influence the energy input for the temperature.

To summarize, the overall algorithm for the force and temperature modeling is shown in Figure 4.4. The C_d , μ , and l_c are calculated in the iterative calculation of undeformed chip thickness distribution and single grit force. The coupling effect of force and temperature is also realized in an iterative manner through the application of J-C material constitutive model.

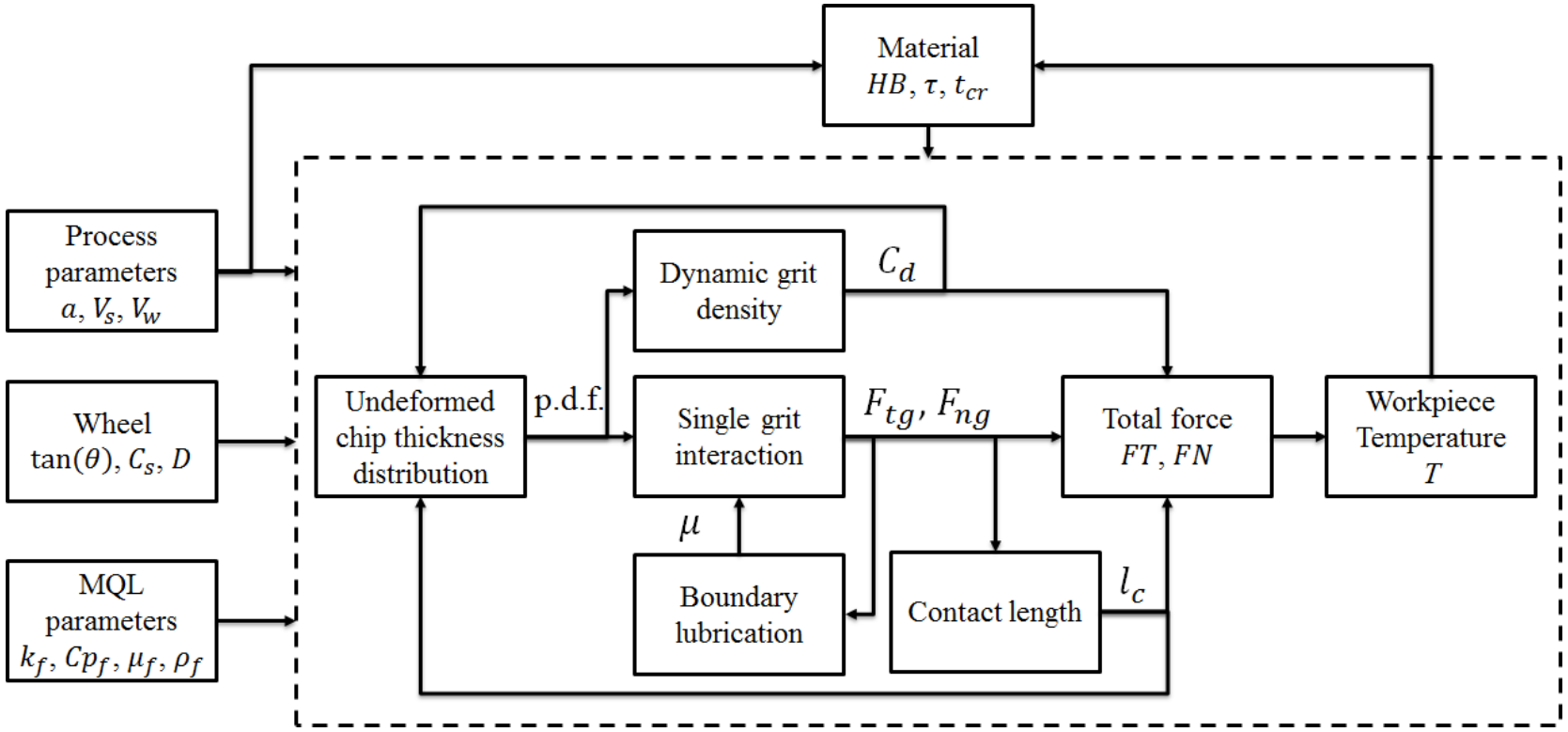

Figure 4.4 Overall algorithm for force and temperature calculation

4.4 Summary

This chapter presents the temperature modeling in grinding under MQL condition. Section 4.1 introduces the moving heat source model that will be used to solve for the temperature distribution in the workpiece analytically. The cooling effect of MQL coolant is modeled as a convective heat loss.

Section 4.2 describes the energy partition in grinding. The heat partition into wheel, chip, workpiece, and coolant is discussed. The estimation of heat transfer coefficient of MQL coolant is based on the calculation of Nusselt number. The thermal properties of MQL coolant is evaluated based on two-phase homogenous flow.

Section 4.3 describes the coupling of force and temperature calculations. The Johnson-Cook material constitutive model is used to predict the flow stress behavior under high temperature and high strain rate condition. An iterative approach is used to calculate the grinding forces and temperature.

In the next chapter, the mechanical and thermal loading stress will be calculated from the grinding forces and temperature distribution. A hybrid algorithm is then utilized to predict the residual stress generation in grinding process.

CHAPTER 5

RESIDUAL STRESS MODELING IN MQL GRINDING

Based upon the grinding force and temperature model developed in CHAPTER 3 and CHAPTER 4, this chapter describes in detail the predictive model of residual stress due to the thermo-mechanical loading for MQL grinding. The mechanical loading stress distribution are first estimated founded on 2D contact mechanics model [74]. The thermal loading stress are then calculated based on Timoshenko thermoelasticity theory [75]. The rolling/sliding contact algorithm developed by McDowell [76] are then adapted and modified to calculate the residual stress profile in the workpiece.

5.1 Stress History Modeling

In order to model residual stresses, the stress history experienced by the workpiece needs to be known. The cause for residual stresses in ground workpiece are majorly from mechanical deformation, thermal expansion and contraction and material phase transformation [28]. The residual stress induced by phase transformation is ignored in this research assuming that the grinding zone temperature doesn't reach the phase transformation triggering temperature. This model assumes that every location at a specified depth in the workpiece experiences the same thermo-mechanical loading history.

The mechanical induced stress is due to localized interactions of abrasive grains with the workpiece. The workpiece is modeled as a semi-infinite, homogeneous,

isotropic, elasto-plastic material with a von Mises yield surface. The elastic modulus and the Poisson's ratio of the workpiece are E and ν, and the coefficient of thermal expansion is α. Assuming a state of plain strain in y direction $(\varepsilon_{yy} = 0)$, at the local scale, the single grit forces are modeled as distributed load with tangential pressure $p(s)$ and normal pressure $q(s)$ as shown in Figure 5.1. Assuming the stress profiles are known, the stresses in the workpiece are computed by integrating the Boussinesq solution for normal and tangential point loads in semi-infinite bodies over the region of contact as given in (5.1).

$$\begin{aligned}
\sigma_{xx}^{mech}(x,z) &= -\frac{2z}{\pi}\int_{-a}^{a}\frac{p(s)(x-s)^2 ds}{((x-s)^2+z^2)^2} - \frac{2}{\pi}\int_{-a}^{a}\frac{q(s)(x-s)^3 ds}{((x-s)^2+z^2)^2} \\
\sigma_{zz}^{mech}(x,z) &= -\frac{2z^3}{\pi}\int_{-a}^{a}\frac{p(s)ds}{((x-s)^2+z^2)^2} - \frac{2z^2}{\pi}\int_{-a}^{a}\frac{q(s)(x-s)ds}{((x-s)^2+z^2)^2} \\
\sigma_{xz}^{mech}(x,z) &= -\frac{2z^2}{\pi}\int_{-a}^{a}\frac{p(s)(x-s)ds}{((x-s)^2+z^2)^2} - \frac{2z}{\pi}\int_{-a}^{a}\frac{q(s)(x-s)^2 ds}{((x-s)^2+z^2)^2} \\
\sigma_{yy}^{mech}(x,z) &= \nu(\sigma_{xx}^{mech}(x,z) + \sigma_{zz}^{mech}(x,z))
\end{aligned} \tag{5.1}$$

where the span of the integrals $[-a,a]$ is a function of the grit tip radius, wear flat length and undeformed chip thickness.

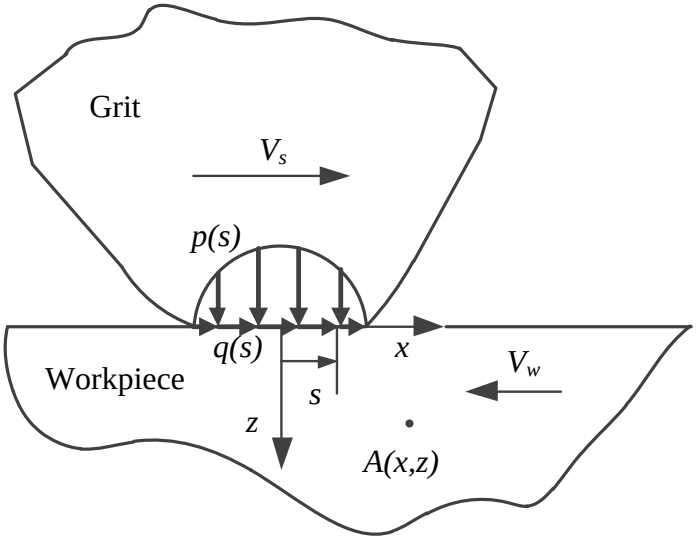

Figure 5.1 Stress resulting from single grit interaction at grit scale

To simplify the problem, the normal contact pressure in the contact region due to the grit-workpiece interaction is assumed to be two-dimensional Hertzian since the contact area is small compared to the sizes of the objects and the stresses are highly concentrated in this area. The half span a is assumed to be The maximum Hertzian pressure p_0 due to the normal load of single grit s shown in (5.2). The shear stress p_0 at the interface is assumed to be uniformly distributed and proportional to the tangential load of the single grit.

$$p_0 = 3F_{ng} / (2\pi a^2), \quad \tau = F_{tg} / (\pi a^2) \tag{5.2}$$

On the other hand, the thermally induced stress field due to non-uniform temperature distribution T are calculated based on the Timoshenko thermoelasticity theory [75]. He proposed a three steps approach to calculate the total thermal stresses by superposing the following components:

(a) Stresses due to body force $X = -\dfrac{\alpha E}{1-2\nu}\dfrac{\delta T}{\delta x}$ and $Z = -\dfrac{\alpha E}{1-2\nu}\dfrac{\delta T}{\delta z}$ along the x and z directions.

(b) Stresses due to a normal surface traction of $\alpha ET/(1-2\nu)$ on the boundary $z = 0$.

(c) A hydrostatic stress of $-\alpha ET/(1-2\nu)$.

The resulting thermal stress components are given as [77]:

$$\sigma_{xx}^{therm}(x,z) = -\frac{\alpha E}{1-2\nu}\int_0^{\infty}\int_{-\infty}^{\infty}\left(G_{xh}\frac{\partial T}{\partial x}(x',z') + G_{xv}\frac{\partial T}{\partial z}(x',z')\right)dx'dz' + \frac{2z}{\pi}\int_{-\infty}^{\infty}\frac{p(t)(t-x)^2}{\left((t-x)^2+z^2\right)^2}dt - \frac{\alpha ET(x,z)}{1-2\nu}$$

$$\sigma_{zz}^{therm}(x,z) = -\frac{\alpha E}{1-2\nu}\int_0^{\infty}\int_{-\infty}^{\infty}\left(G_{zh}\frac{\partial T}{\partial x}(x',z') + G_{zv}\frac{\partial T}{\partial z}(x',z')\right)dx'dz' + \frac{2z^3}{\pi}\int_{-\infty}^{\infty}\frac{p(t)}{\left((t-x)^2+z^2\right)^2}dt - \frac{\alpha ET(x,z)}{1-2\nu} \tag{5.3}$$

$$\sigma_{xz}^{therm}(x,z) = -\frac{\alpha E}{1-2\nu}\int_0^{\infty}\int_{-\infty}^{\infty}\left(G_{xzh}\frac{\partial T}{\partial x}(x',z') + G_{xzv}\frac{\partial T}{\partial z}(x',z')\right)dx'dz' + \frac{2z^2}{\pi}\int_{-\infty}^{\infty}\frac{p(t)(t-x)}{\left((t-x)^2+z^2\right)^2}dt$$

$$\sigma_{yy}^{therm}(x,z) = \nu(\sigma_{xx}^{therm} + \sigma_{zz}^{therm}) - \alpha ET(x,z)$$

where

$$p(t) = \frac{\alpha E T(x, z = 0)}{1 - 2\nu} \tag{5.4}$$

and $(G_{xh}, G_{zh}, G_{xzh}, G_{xv}, G_{zv}, G_{xzv})$ are the plain strain Green's functions [78]. For example, $G_{xh}(x, z, x', z')$ is the stress $\sigma_{xx}(x, z)$ due to a unit load acting along the x direction applied at (x', z').

The stress history experienced by the workpiece due to combined effect of mechanical and thermal stress is further discussed here.

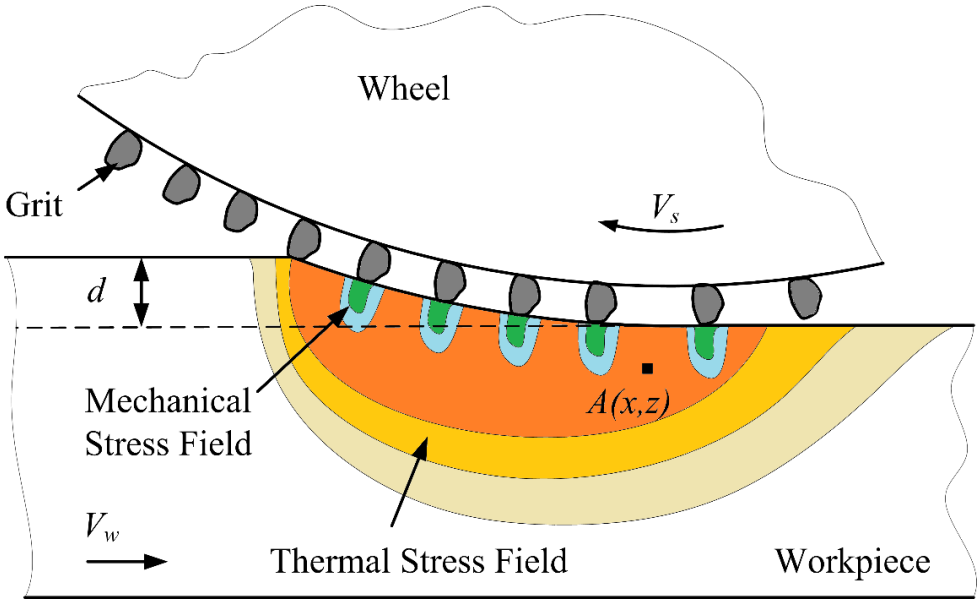

Figure 5.2 Stress history illustration

As shown in Figure 5.2, the grit is travelling at a much higher speed $(V_w + V_s)$ than the moving speed of wheel-workpiece contact zone V_w. In other words, during the time that the contact zone travels a certain length, many loading passes of the single grit interactions have been experienced by the workpiece. Therefore, the residual stress

induced by mechanical deformation should be modeled as multiple loading passes. The number of loading passes n_{pass} is determined by the contact length l_c, the average distance between active grits l_0, and the speed ratio $(V_w + V_s)/V_w$.

$$n_{pass} = (l_c / l_0)((V_w + V_s)/V_w) \tag{5.5}$$

Different form the mechanical loading, the thermal stress field is modeled from a larger scale considering the total heat input from all the grits in the wheel/workpiece contact zone. Therefore, the temperature field is moving at the speed of V_w and the stress history due to thermal stress field are obtained for a single loading pass.

The mechanical loading stress by an individual grit is calculated using (5.1). An example is given in Figure 5.3. It is discovered that plastic deformation induced by grit interactions only happen at the place very close to the surface (<0.1 mm) as shown from the calculated single grit stress. In comparison, the thermal stress in the same condition is calculated using (5.3) based on the temperature distribution in the workpiece. The thermal loading stress is reaching to a larger depth underneath the surface.

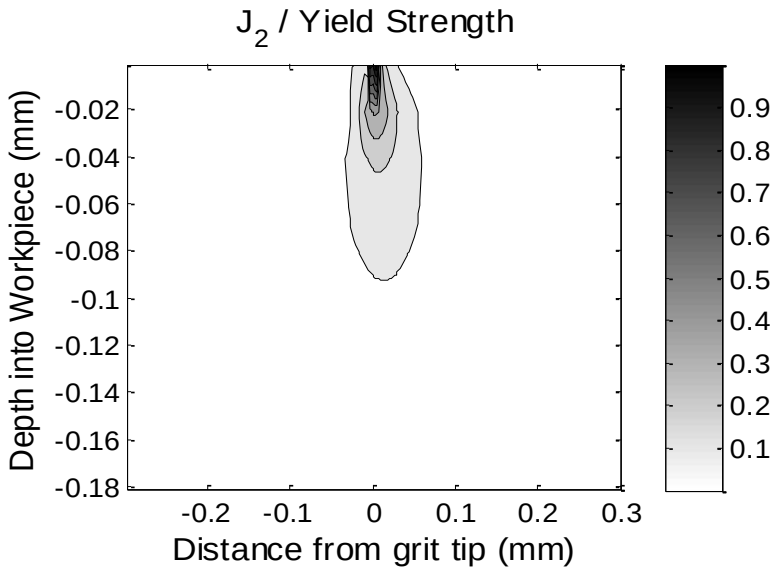

(a) Mechanical stress field

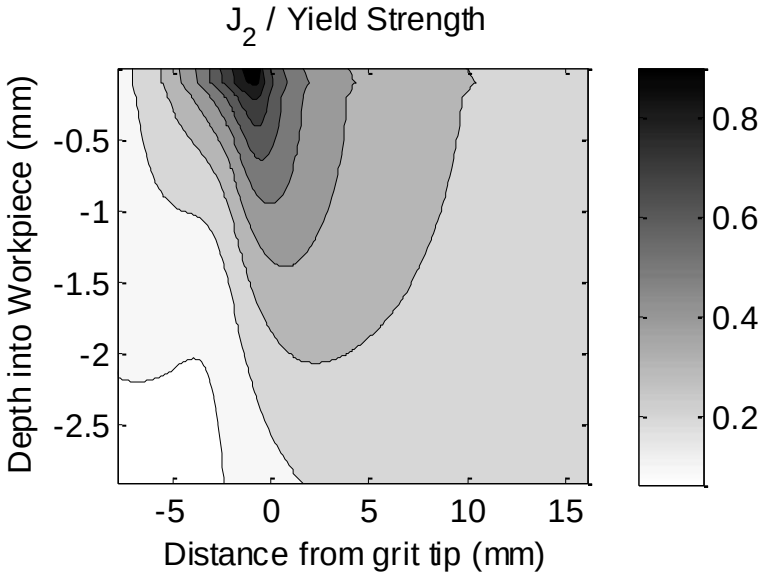

(b) Thermal stress field

Figure 5.3 Mechanical and thermal stress field

Therefore, the total stress history should be obtained as the coupling of multiple single grit contact stress fields and thermal stress field because of the difference in strain rate and number of passes. As a result, hundreds of mechanical stress fields need to be

superposed with a single thermal stress field. The residual stress should be then calculated based on this fully coupled stress history. However, due to the huge difference in the stress field scale and large number of single grit contacts, this requires very fine calculation of the temperature and thermal stress field which cannot be satisfied by the current computational power. Also this approach is not necessary at subsurface areas since the mechanical effect is localized near the surface.

Therefore, a separate calculation of mechanical and thermal induced residual stress was carried in this study. The final residual stress result is obtained as the superposition of mechanical and thermal induced residual stress. For mechanical induced residual stress calculation, the residual stresses and strains of the first pass are calculated and assigned to be the initial values for the next passage of the load. Although it is possible that the second grit will start engage with the workpiece before the first grit disengage with the workpiece, it is still valid to make this assumption since the length scale of local stress field created by single grit interaction is much smaller comparing to the distance between successive grits. This approach may lead to inaccurate calculation of residual stress near the surface where mechanical effect is strong. In the subsurface area, where the thermal effect is the only dominant factor, this approach is expected to achieve the same result.

5.2 Residual Stress Modeling

Here, a hybrid algorithm developed by McDowell [76] is modified and utilized to compute the residual stresses in MQL grinding. The model provides a robust, stable prediction of subsurface plasticity and residual stresses over a wide range of loading

conditions. This algorithm uses a blending function Ψ which is dependent on the instantaneous value of the modulus ratio h/G, where h is the plastic modulus, G is the elastic shear modulus and κ is an algorithm constant. The blending function is given as:

$$\Psi = 1 - \exp\left(-\kappa\left(3h/2G\right)\right) \tag{5.6}$$

A rate-independent cyclic plasticity framework is employed here, based on a von Mises yield surface given as:

$$F = \frac{3}{2}(S_{ij} - \alpha_{ij})(S_{ij} - \alpha_{ij}) - R^2 = 0 \tag{5.7}$$

where $S_{ij} = \sigma_{ij} - (\sigma_{kk}/3)\delta_{ij}$ is the deviatoric stress, α_{ij} is the backstress and R is the uniaxial normalized radius of the yield surface. Linear kinematic hardening is utilized in the model and the evolution of the backstress is given by:

$$\dot{\alpha}_{ij} = \left\langle \dot{S}_{mn} n_{mn} \right\rangle n_{ij} \tag{5.8}$$

Johnson-Cook material constitutive model is used to capture the yield surface change due to thermal and strain rate effect.

$$R = \left(A + B\right)\left(1 + C\ln\left(\frac{\dot{\varepsilon}_{effective}}{\dot{\varepsilon}_0}\right)\right)\left(1 - \left[\frac{\left(T - T_r\right)}{\left(T_m - T_r\right)}\right]^m\right) \tag{5.9}$$

The yield surface is calculated at every incremental step to account for local strain rate and temperature effect. It should be noted that the mechanical and thermal strain rate are different due to the difference in the moving speed of the stress field. The effective plastic strain rate is calculated as:

$$\dot{\varepsilon}_{effective} = \sqrt{\frac{2}{3}\left(\dot{\varepsilon}_{xx}^{p\,2} + \dot{\varepsilon}_{yy}^{p\,2} + \dot{\varepsilon}_{zz}^{p\,2} + 2\dot{\varepsilon}_{xz}^{p\,2}\right)} \tag{5.10}$$

The normality flow rule is used to calculate plastic strain rate:

$$\dot{\varepsilon}_{ij}^{p} = \frac{1}{h}\left\langle \dot{S}_{mn} n_{mn} \right\rangle n_{ij} \tag{5.11}$$

with $n_{ij} = \sqrt{(3/2)}(S_{ij} - \alpha_{ij})/R$, $\langle\ \rangle$ is the MacCauley bracket defined as $\langle x \rangle = 0.5(x + |x|)$.

For elasic-plastic loading, the blending function is used to describe the strain rate in the grinding direction as shown in (5.12).

$$\begin{aligned} \dot{\varepsilon}_{xx} &= \frac{1}{E}\left[\dot{\sigma}_{xx} - \nu\left(\dot{\sigma}_{yy} + \dot{\sigma}_{zz}^{*}\right)\right] + \frac{1}{h}\left(\dot{\sigma}_{xx} n_{xx} + \dot{\sigma}_{yy} n_{yy} + \dot{\sigma}_{zz}^{*} n_{zz} + 2\dot{\tau}_{xz}^{*} n_{xz}\right) n_{xx} \\ &= \Psi\left(\frac{1}{E}\left[\dot{\sigma}_{xx}^{*} - \nu\left(\dot{\sigma}_{yy} + \dot{\sigma}_{zz}^{*}\right)\right] + \frac{1}{h}\left(\dot{\sigma}_{xx}^{*} n_{xx} + \dot{\sigma}_{yy} n_{yy} + \dot{\sigma}_{zz}^{*} n_{zz} + 2\dot{\tau}_{xz}^{*} n_{xz}\right) n_{xx}\right) \end{aligned} \tag{5.12}$$

The quantities superscripted with asterisks represent the elastic solution. Similarly, the plane-strain condition is imposed as given in(5.13).

$$\dot{\varepsilon}_{yy} = \frac{1}{E}\left[\dot{\sigma}_{yy} - \nu\left(\dot{\sigma}_{xx} + \dot{\sigma}_{zz}^{*}\right)\right] + \frac{1}{h}\left(\dot{\sigma}_{xx} n_{xx} + \dot{\sigma}_{yy} n_{yy} + \dot{\sigma}_{zz}^{*} n_{zz} + 2\dot{\tau}_{xz}^{*} n_{xz}\right) n_{yy} = 0 \tag{5.13}$$

The equations are solved simultaneously to determine the increments of stress for $\dot{\sigma}_{xx}$ and $\dot{\sigma}_{yy}$. The stress increments are integrated over the passage of the load to determine the residual stresses. At the end of each pass, the stresses are relaxed to satisfy boundary conditions as described by Merwin and Johnson [79] as shown in (5.14).

$$\begin{aligned} &\left(\varepsilon_{xx}\right)_r = 0 \qquad \left(\sigma_{xx}\right)_r = f_1(z) \qquad \left(\varepsilon_{yy}\right)_r = 0 \qquad \left(\sigma_{yy}\right)_r = f_2(z) \\ &\left(\varepsilon_{zz}\right)_r = f_3(z) \qquad \left(\sigma_{zz}\right)_r = 0 \qquad \left(\gamma_{xz}\right)_r = f_4(z) \qquad \left(\tau_{xz}\right)_r = 0 \end{aligned} \tag{5.14}$$

In order to maintain the equilibrium condition, the non-zero components $\sigma_{zz}{}^{R}$, $\tau_{xz}{}^{R}$, and $\varepsilon_{xx}{}^{R}$ are incrementally relaxed to meet the boundary conditions. If M steps are used for the relaxation process, then the stress increments are

$$\Delta\sigma_{zz} = -\frac{\sigma_{zz}^{R}}{M}, \qquad \Delta\tau_{xz} = -\frac{\tau_{xz}^{R}}{M}, \qquad \Delta\varepsilon_{xx} = -\frac{\varepsilon_{xx}^{R}}{M}. \tag{5.15}$$

At the end of the relaxation procedure, both σ_{xx} and σ_{yy} will be non-zero. These values are the true residual stresses that remain in the body.

During relaxation, there are two possibilities for material behavior: purely elastic relaxation and elastic-plastic relaxation. For purely elastic relaxation, $F<0$ or $F=0$ and $dS_{ij}n_{ij}<0$, the elastic relaxation increments for σ_{xx} and σ_{yy} are given by Equation (5.16).

$$\begin{aligned}\Delta\sigma_{xx} &= \frac{\Delta\sigma_{zz}\nu(1+\nu)-E\Delta\varepsilon_{xx}}{(1-\nu^2)}\\ \Delta\sigma_{yy} &= \nu(\Delta\sigma_{xx}-\Delta\sigma_{zz})\end{aligned} \tag{5.16}$$

For elastic-plastic case, $F=0$ and $dS_{ij}n_{ij}\geq 0$, the elastic relaxation increments for σ_{xx} and σ_{yy} are given by Equation(5.17).

$$\begin{aligned}\Delta\sigma_{yy} &= \frac{\left(-\frac{\nu}{E}+\frac{n_{xx}n_{yy}}{h}\right)C-\left(\frac{1}{E}+\frac{n_{xx}^2}{h}\right)D}{\left[\left(-\frac{\nu}{E}+\frac{n_{xx}n_{yy}}{h}\right)^2-\left(\frac{1}{E}+\frac{n_{xx}^2}{h}\right)\left(\frac{1}{E}+\frac{n_{yy}^2}{h}\right)\right]}\\ \Delta\sigma_{xx} &= \frac{D-\left(\frac{1}{E}+\frac{n_{yy}^2}{h}\right)\Delta\sigma_{yy}}{\left(-\frac{\nu}{E}+\frac{n_{xx}n_{yy}}{h}\right)}\end{aligned} \tag{5.17}$$

where

$$\begin{aligned}C &= -\Delta\varepsilon_{xx}-\Delta\sigma_{zz}\frac{\nu}{E}+\frac{1}{h}\Delta\sigma_{zz}n_{zz}n_{xx}+\frac{2}{h}\Delta\tau_{xz}n_{zz}n_{xx}\\ D &= -\frac{\nu}{E}\Delta\sigma_{zz}+\frac{1}{h}\Delta\sigma_{zz}n_{yy}n_{xx}+\frac{2}{h}\Delta\tau_{xz}n_{zz}n_{xx}\end{aligned} \tag{5.18}$$

For modeling the mechanical induced residual stress, the same routine is repeated for the number of passes in (5.5) with the previous residual stresses assigned to be the

initial values for the next passage of the load. The residual stress will reach a stabilized state after some passes. The thermally induced residual stress is calculated from one loading passage as mentioned above. The final residual stress profile is from the superposition of mechanically induced and thermally induced residual stresses.

5.3 Summary

This chapter introduces the predictive models of residual stress generation in grinding condition. Section 5.1 describes the approach for estimating the loading stresses due to mechanical interaction and temperature gradient in the workpiece. The total loading history resulted from thermos-mechanical stresses will be used as the driving force in residual stress prediction. The mechanical and thermal residual stresses are calculated separately in this work due to the large scale difference between these two stress sources.

Section 5.2 introduces the McDowell algorithm for calculation of residual stresses. The evolution of yield surface is based on linear kinematic hardening law. The Johnson-Cook material constitutive model is also utilized to capture the temperature and strain effect on the yield surface size change. An elastic-plastic relaxation procedure is forced at the end to meet the boundary conditions.

In the next chapter, the model predictions of grinding forces, temperature as well as residual stresses will be validated by experiments.

CHAPTER 6

EXPEPRIMENTAL CALIBRATION AND VALIDATION OF MQL GRINDING MODEL

In this chapter, the modeling techniques described in CHAPTER 3 though CHAPTER 5 are implemented and compared with experimental data. A series of experiments were performed in surface grinding, with different wheels, workpiece materials, lubrication conditions, as well as process parameters. The grinding setup as well as measurement techniques are first introduced. The parameters of the tool condition, material properties and lubrication condition are taken from literature and experimental measurement. Cutting forces, temperature and residual stresses comparison results under different grinding conditions are then presented.

6.1 Experiment Setup

Since it is very difficult to measure grinding forces and temperatures in cylindrical grinding, the model validation is carried out on surface grinding tests. The workpiece materials implemented in the experimental study are AISI 1018 steel and AISI 1045 steel. The workpiece materials are cut into rectangular bars of 9.5mm width and around 150mm length. The surface to be tested on was ground on a surface grinder to ensure surface finish and dimensional accuracy. To prevent the residual stress generated

from previous cold-working processes from affecting the experimental result, all the workpieces are stress relieved in a vacuum furnace.

The experiments were performed on the Bridgeport GX 480 vertical milling center in Precision Machining Research Center at Georgia Tech. The CNC milling center is able to precise control the spindle rotational speed (Up to 10000RPM) and work speed with positional accuracy of 0.002 mm. Since the stiffness of a milling machine is generally lower than a grinding machine, relatively low material removal rate has been used in the experimental study to avoid high grinding load. It should be mentioned that single pass experiment is employed in this study since in multiple passes experiment, the residual stresses generated from previous passes may influence the result of current pass. The surface to be ground is achieved by several pre-test grinding steps. These grinding steps are carried at extremely low material removal rate (specific MRR: 2.15e-3 mm^2/s) to avoid introducing large subsurface residual stress to the workpiece. It is assumed that the residual stress affected zone due to pre-test grinding steps is localized at the surface and will be removed by the experimental grinding pass.

Dry, MQL and flood cooling tests have been pursued. The range of wheel speed, material removal rate are chosen based on the specification of the tool, and pre-grinding tests to ensure stable grinding process. The grinding wheel employed in this study was a vitrified-bond aluminum oxide wheel (Norton 38A120-KVBE). The diameter of the wheel is 150mm and the wheel width is 12.7mm. The experimental setup is shown in Figure 6.1. The wheel was dressed by single point diamond dresser with 16 μm dressing depth and overlap ratio of 1.68 same as in the experimental tests. The grinding wheel was dressed before each experiment set.

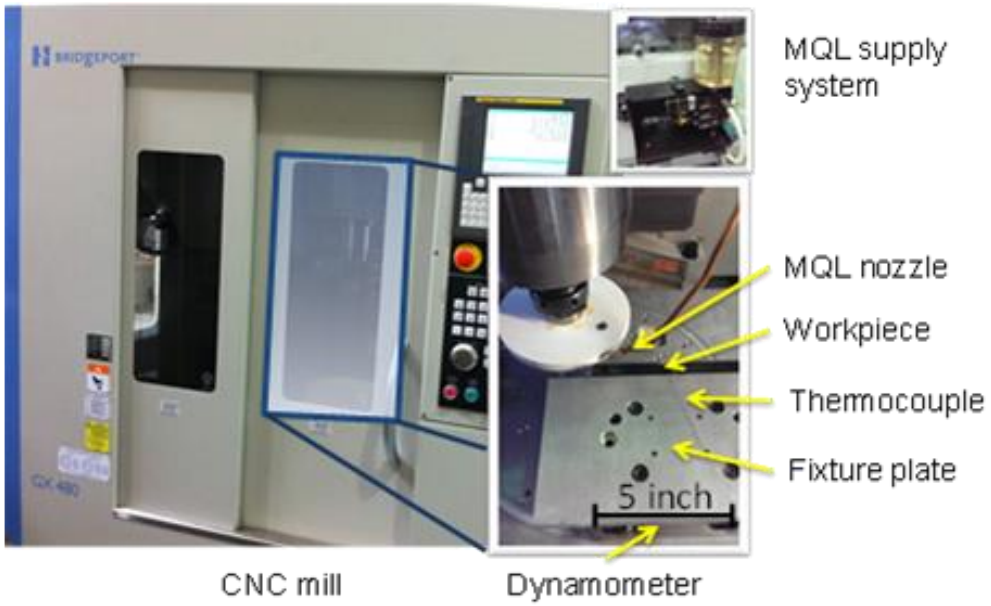

Figure 6.1 Experiment Set-up

Figure 6.2 MQL supply system

The MQL controlling system was Coolubricator^{TM} manufactured by UNIST, Inc. as shown in Figure 6.2. The lubrication medium is vegetable oil and flow rate constant at

396ml/hr. The pressurized air pressure was supplied externally at 4bars. The nozzle distance to the contact zone was 40mm and the impingement angle is 10°. The angle of nozzle relative to the workpiece surface was 10°. The flow rate as well as air pressure was adjusted to order to achieve effective MQL grinding process.

6.1.1 Wheel Surface measurement

The grinding wheel surface must be characterized to understand its interaction with the workpiece material during chip generation process. An important parameter that characterize the grinding process is the dynamic grit density. As suggested in section 3.3, the dynamic grit density depends on static distribution of grits on the wheel surface as well as kinematic conditions. The static grit distribution must be evaluated first in order to correctly model the dynamic distribution of cutting edges.

Due to the poor optical property and geometrical constraints, the grinding wheel surface can't be directly measured by interferometry. The current work utilize the imprint method to obtain the wheel surface geometry. The lead sample is polished and pressed onto wheel surface to print the outmost cutting edges. Since the lead sample is very soft and it is assumed that no local grit deflection due to the indentation force. The 3-D surface texture of the grinding wheel is scanned with Zygo Newview white light interferometer as shown in Figure 6.3. In order to have a sufficient number of grains, a surface area of 2.4mm by 1.8mm was measured. The pixel resolution is 2.2μm by 2.2μm. The digitalized image is analyzed in MATLAB R2013 with customized processing functions to extract the desired wheel surface information. The main parameters to be extracted are the average cutting edge geometry and the static cutting edge density $C_{s(z)}$

as a function of radial distance measured into the wheel z . A wheel surface measurement example is shown in Figure 6.4.

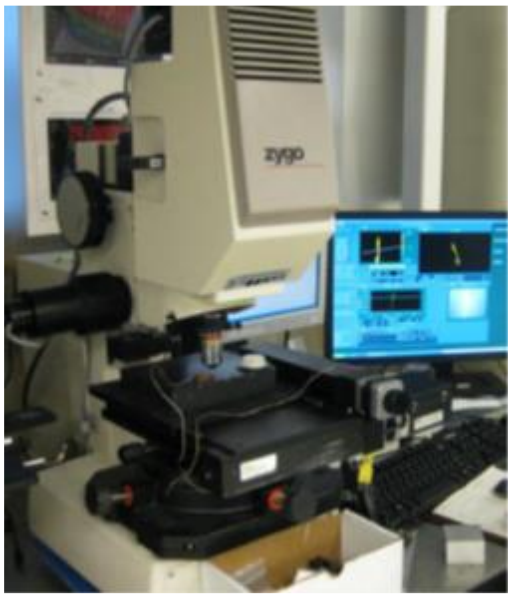

Figure 6.3 Zygo Interferometer

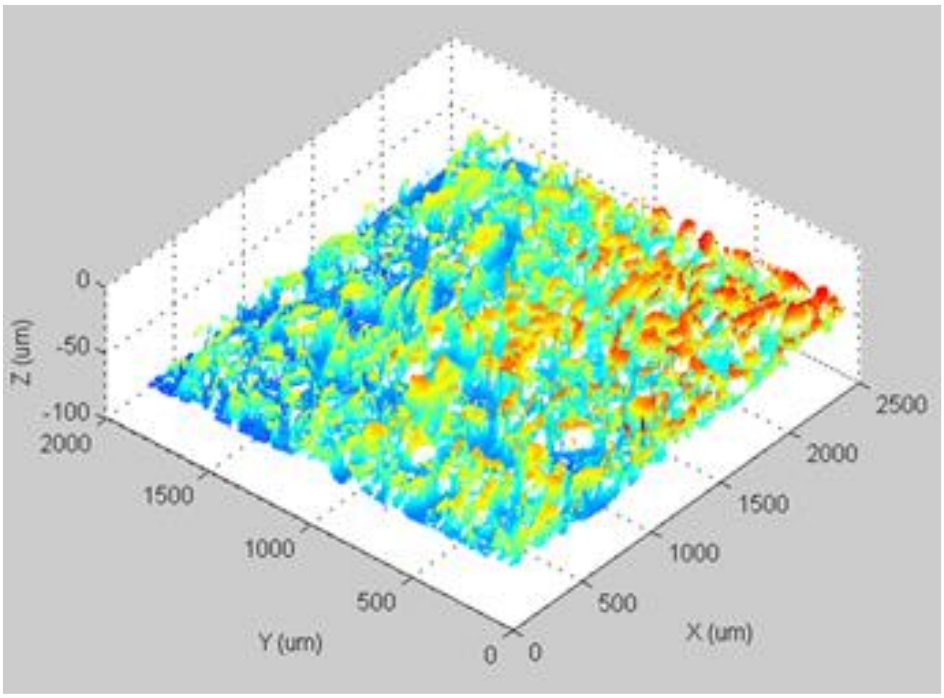

Figure 6.4 Example of wheel surface measurement

6.1.2 Grinding Force Measurement

The grinding force components were recorded using a piezo-electric transducer based dynamometer (type Kistler 9257B). The grinding force measurement set up is shown in Figure 6.5. As shown in the figure, the workpiece was mounted on the side of an aluminum plate which was fixed on top of the dynamometer. During the grinding test, the force signal is transformed into charge signal. The charge signal was amplified and collected by the DAQ system, and then processed using Simulink software. There are three orthogonal force components collected by the dynamometer, only two of which are of interest: the tangential grinding force F_t and the normal grinding force F_n.

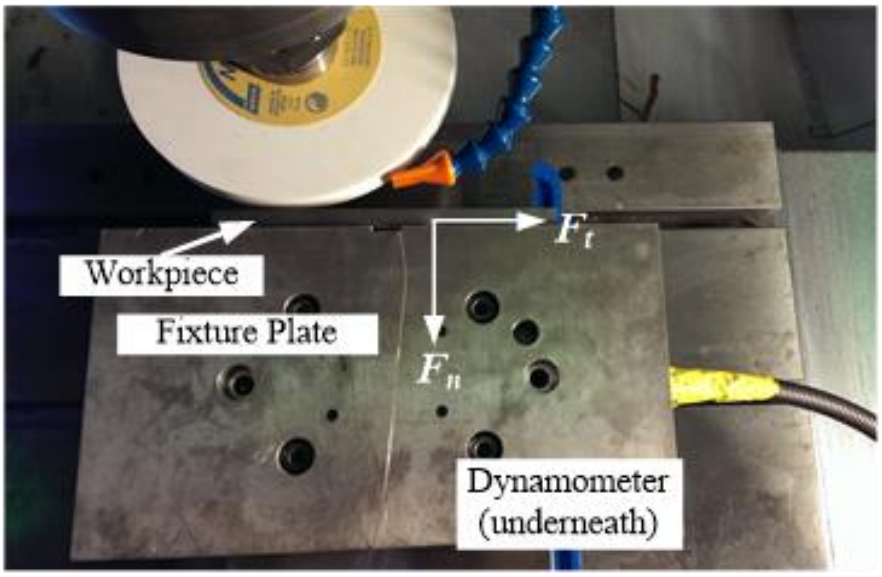

(a) Top view

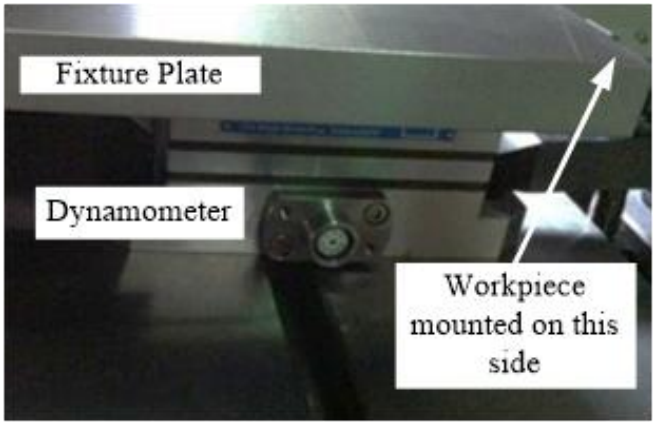

(b) Side view

Figure 6.5 Illustration of grinding force measurement.

6.1.3 Grinding Temperature Measurement

Two different method of temperature measurement has been utilized in this study: thermocouple and thermal camera. As shown in Figure 6.6, the hot junction of the thermocouple was welded by thermal epoxy to the bottom of a blind hole with 1.5mm distance to the ground surface. The thermocouple used in this experiment was Omega type K thermocouple (5TC-TT-K-36-36) with a maximum working temperature of 590 ℃ and the DAQ system was Omega OM-DAQ-USB-2401 with a sampling frequency range of 1-10000 Hz. The diameter of the thermocouple wire is 0.127 mm and the time constant is 0.01s. The thermal camera used was FLIR SC6000 infrared camera. As shown in Figure 6.7, the thermal camera fixed on the tripod was placed at the side of the machine. Since the infrared light couldn't pass through glass, a custom made acrylic panel with cut-out was used for the thermal camera to capture the temperature. The emissivity of thermal camera setting was calibrated by placing the workpiece on a hot plate with temperature measurements by thermocouples.

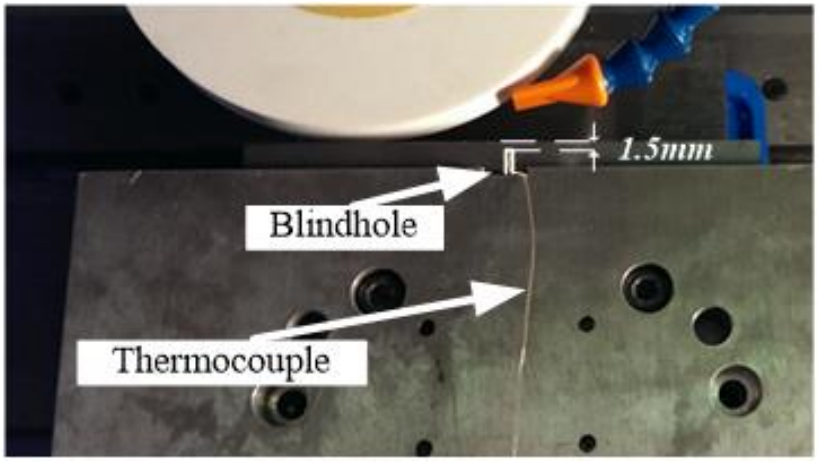

Figure 6.6 Thermocouple set-up

Figure 6.7 Infrared camera set-up

6.1.4 Residual Stress Measurement

The residual stresses in tangential and traverse direction were measured on PROTO LXRD 2000 X-ray diffraction machine as shown in Figure 6.8. The source is 3kW ceramic/metal Model XRT 60 X-ray tube with Cr anode and the detector is

proprietary dual position sensitive scintillation detectors (PSSD). The measurement was taken with seven psi tilt angles from -20 °to 20 °.

In sample preparation process, PROTO Electropolisher Model 8818-V3 was used for residual stress with depth determination by removing layers from the specimen without incurring cold-working stresses as shown in Figure 6.9. The input voltage, current, electrolyte and polishing time was tested and adjusted to ensure constant polishing depth. The polishing depth was measured by a 3-D optical profilometer. The residual stress at 0 mm is measured directly on the ground surface without polishing.

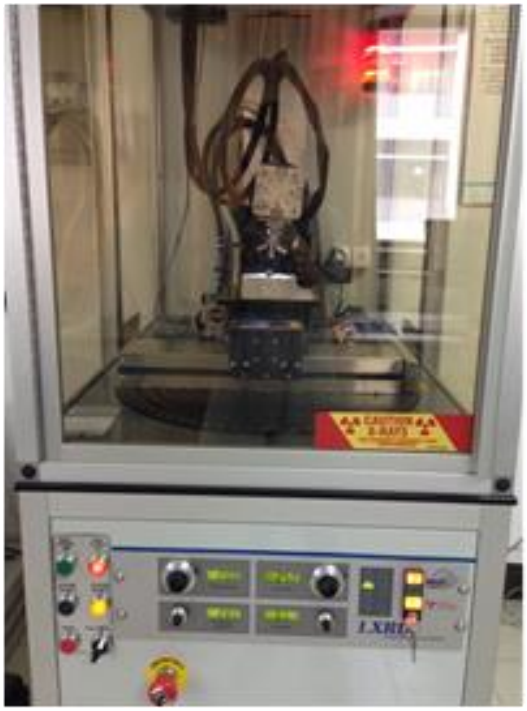

Figure 6.8 X-ray diffractometer

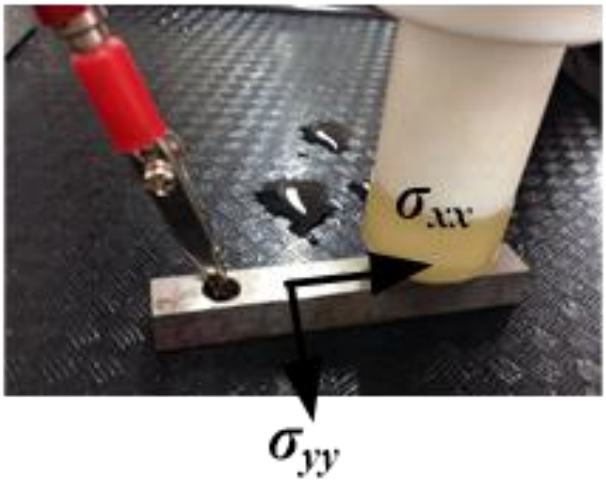

Figure 6.9 Electropolishing of workpiece

6.2 Parameter Analysis

The set of equations to predict the grinding force, temperature and residual stress presented in the previous chapters requires the knowledge of tool condition, material properties and lubrication condition. The parameter analysis are presented in this section. Some of the properties are taken from literature and some are from experimental measurement as discussed in the following sections.

6.2.1 Wheel and Workpiece Material Properties

The properties of the wheel and the workpiece are needed for the physical models. For the vitrified bond aluminum oxide wheel, the necessary mechanical and thermal properties are summarized in Table 6.1. For the workpiece material, Johncon-Cook flow stress parameters for the materials used for model validations are listed in Table 6.2. Additional material properties used to model residual stresses and forces are provided in Table 6.3.

Table 6.1 Properties of vitrified bond aluminum oxide grinding wheel [66]

Parameter	E (GPa)	ν	k (W/m ℃)	C_P (J/kg ℃)	ρ (kg/m^3)
Value	49.6 (vitrified bond)	0.22 (vitrified bond)	46 (Al_2O_3)	765 (Al_2O_3)	3970 (Al_2O_3)

Table 6.2 Johnson-Cook parameters for materials used [80] [81]

Material	A (MPa)	B (MPa)	n	C	m
AISI 1018	520	269	0.282	0.0476	0.553
AISI 1045	553	601	0.234	0.0134	1.0

Table 6.3 Additional material properties used in the model

Material	E (GPa)	ν	H (Brinell)	ρ (kg/m^3)	k (W/m ℃)	C_P (J/kg ℃)	α (℃$^{-1}$)	T_m (℃)
AISI 1018	200	0.29	131	7870	51.9	486	12e-6	1470
AISI 1045	206	0.29	197	7850	49.8	486	11e-6	1733

6.2.2 Wheel Surface Parameters

The 3-D surface measurement data is processed and analyzed with Matlab code. During wheel surface scanning, the measuring table was adjusted to position the sample horizontally. The 3-D imaging process includes: 1) Filling the missing data based on neighborhood information, 2) noise reduction, and 3) removal of spatial orientation of the plane of reference. Figure 6.10 shows a reproduction of five grains on the wheel surface. It could be observed that some grains presents more than one cutting edge.

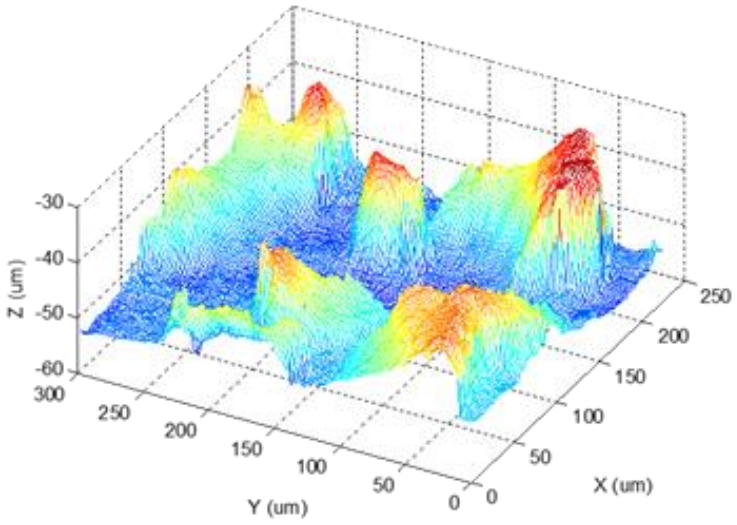

Figure 6.10 Wheel surface measurement after image processing

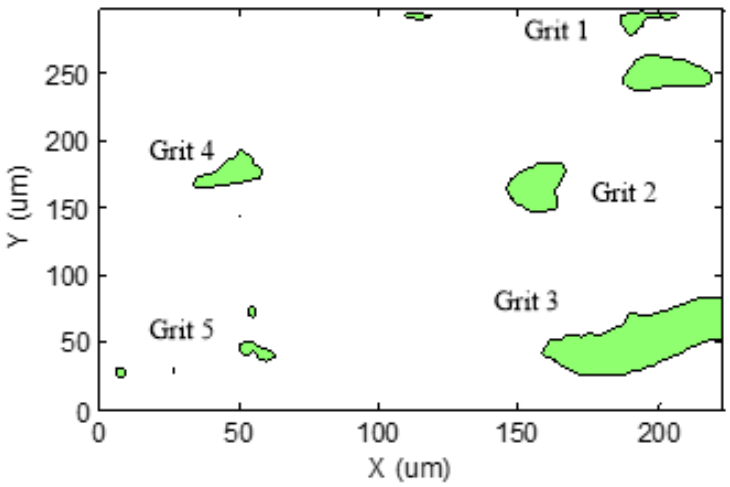

Figure 6.11 A cross-sectional image of wheel surface

6.2.2.1 Static grit density

The static grit density is determined by counting the number of grits that appears in radial direction from the grinding wheel outmost surface, and dividing that number by the total area observed. In order to exactly estimate the number of grits as a function of depth into the wheel, a series of 2-D images are generated intersecting the 3-D image

with horizontal planes at 1μm resolution. A cross-sectional image of the grits in Figure 6.10 is shown in Figure 6.11. Since some of the grains may have multiple cutting edges, the grit number of all the cross section planes are counted manually.

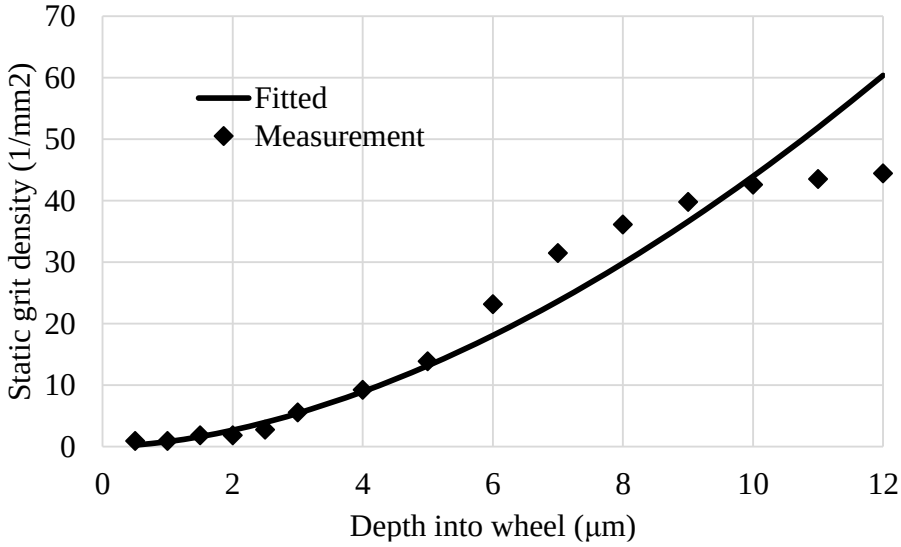

Figure 6.12 Static grit density

Figure 6.12 shows the static grit density as a function of the depth of penetration into the wheel. For the 120 grit wheel used in the experiment, the fitted result for the static grit density is:

$$C_s = 0.80z^{1.74} \tag{6.1}$$

In (6.1) the unit of C_s is *number of grits/mm*^{2}, and the unit of z is μm. It should be mentioned that the equation (6.1) is a monotonically increasing function, but in reality the grit number can't be infinite. The maximum grit number should be defined to prevent overestimating the grit density at large engagement depth. Based on the result from

Figure 6.12, the maximum static grit density number for the 120 grit wheel is about 44.4mm^{-2}.

6.2.2.2 Grit geometry

The shape of the grinding grit is random, however, a simple geometry need to be assumed for the purpose of analysis. In this study, the grit shape is assumed to be a conical shape with a rounded tip as shown in Figure 6.13. Two important parameters need to be determined: the cone angle and the grit tip radius.

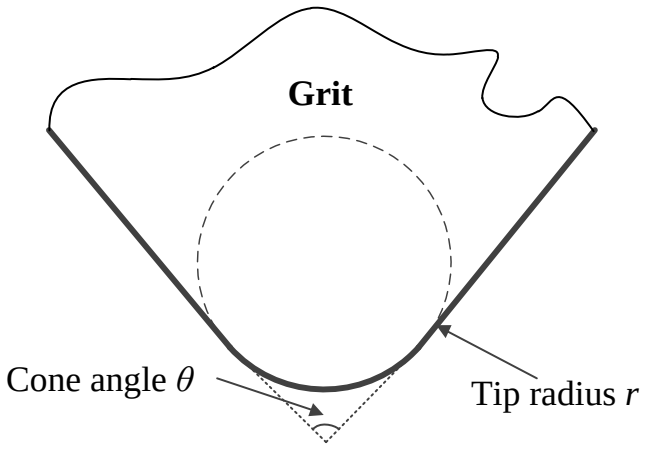

Figure 6.13 Grit shape assumption

The method for estimation of grit tip radius is modified from Hecker's work [49]. A number of 20 grits have been randomly chosen for estimating the grit tip geometry. To estimate the grit tip radius, the sectional area of the grit is obtained as a function of the depth measured from the highest point of the grit, and the diameter of the grit tip d_g is calculated by fitting the following equation:

$$A_g = \pi d_g h_g - \pi h_g^2 \tag{6.2}$$

where A_g is the cross-sectional area of a sphere at depth h_g. Figure 6.14 shows the cross sectional area as a function of the depth from the top of each individual grit, where the grit number 2 and 4 are from Figure 6.11. The estimated average grit tip radius is 28.01μm, which is significantly smaller than 63.3μm which is estimated from the grit size calculation given as [3]:

$$d_g = 15.2M^{-1} \tag{6.3}$$

where M is the grit number. Similar results have been achieved by others [82].

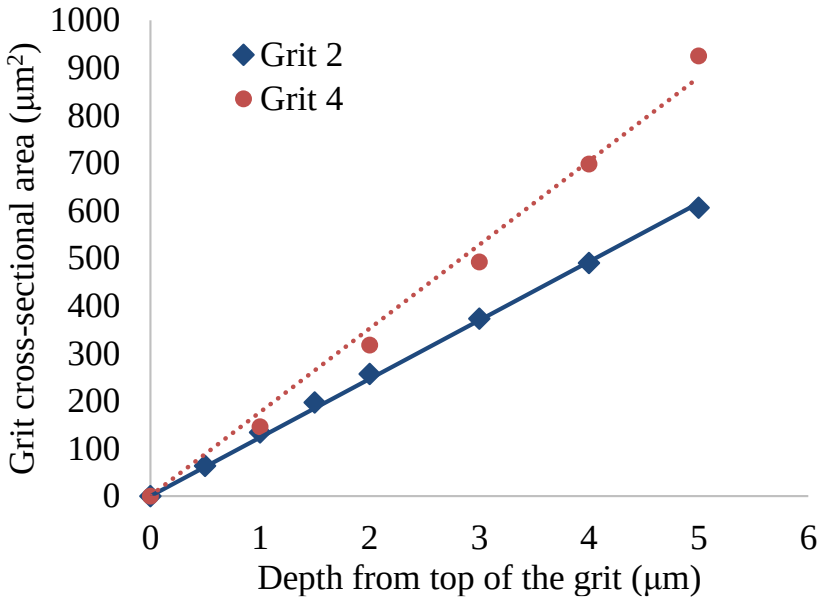

Figure 6.14 Experimental and fitted cross sectional area of two grits as a function of depth from the top of the grit

Since the grit shape was assumed to be conical with a rounded tip, the cone angle need to be estimated as well. The assumption of conical shape is for the robustness of the prediction model. Since if the grit tip radius is too small and is comparable to undeformed chip thickness, a rounded tip assumption would result in incorrect single grit force

estimation due to the local rake angle calculation. Assume the cone angle is θ and the depth h_g is larger enough to excel the rounded part, then the following equation can be used to estimate the cone angle:

$$\begin{aligned} A_g &= \pi \left\{ \frac{d_g}{2}\cos(\theta/2) + \left[h_g - \frac{d_g}{2}\left(1-\sin(\theta/2)\right) \right] \tan(\theta/2) \right\}^2 \\ &= \pi \left[h_g \tan(\theta/2) + \frac{d_g}{2}\left(\frac{1-\sin(\theta/2)}{\cos(\theta/2)} \right) \right]^2 \end{aligned} \tag{6.4}$$

The mean square error method was used to calculate the best θ for each grit, the average result is about 136.6°. This result coincide with the result from Hecker [49] of about 144° but is much higher than the result from Yan et al. [82] of about 77.4°.

6.2.3 Boundary Lubrication Parameters

In calculation of friction coefficient in boundary lubrication, some of the parameters in 3.1 should be determined. The shear strength of the adsorbed lubricant film s_b can be estimated by:

$$s_b = \nu \rho \dot{\gamma} \tag{6.5}$$

where ρ is the density of the lubricant film, ν is the kinematic viscosity, and $\dot{\gamma}$ is the shear strain rate. Here it is assumed that the shear strain rate of the lubricant film equals to the shear strain rate of the workpiece material in the shear zone. The representative value of the coefficient C_2 is determined to be 0.5 according to Kato et al. [50]. The parameter C_3 could then be determined from the estimation of C_1, C_2 and s_b.

The estimation of the contact parameters are discussed here. At the grit-workpiece contact surface, the number and geometry asperities are determined by the grit shape and

the dressing conditions. As observed from Figure 6.10, many grits have multiple cutting edges due to the dressing. The total asperity number n_0 on the grit-chip contact area is calculated as:

$$n_0 = A_0 z^2 \tag{6.6}$$

where A_0 is the contact area between the grit and the workpiece which can be estimated from the grit size and undeformed chip thickness; z is the linear asperities density. The linear asperity number is estimated from the measurement of 50 different grits and is found to be 20mm^{-1}. The maximum asperity height $H_{\max}$ and radius R are also estimated from the wheel surface measurements. The adsorbed lubricant film thickness t_b is associated with the flow rate of the MQL lubricant, air pressure, as wheel as wheel/workpiece material and the geometry of the grit. It is to be calibrated by experiment. To summarize, the estimated and measured parameters for predicting the friction coefficient in boundary lubrication in grinding are listed in Table 6.4.

Table 6.4 Parameters in boundary lubrication

Parameter	C_2	H_{max} (μm)	R (μm)	D	Z (mm^{-1})	ρ (kg/m^3)	v (mm^2/s)
Value	0.5	10	20	1.5	20	980	38.63

6.3 Grinding Force Validation

6.3.1 Test Conditions

The validation of grinding forces is verified by measuring the grinding forces with the dynamometer while grinding AISI 1045 steel and AISI 1018 steel under various grinding conditions as shown in Table. Here, 'wet' represents the conventional flood cooling condition. A typical measurement of the grinding force is shown here as in Figure 6.15. Every test for grinding force validation is repeated three times. The average grinding force is extracted from the recorded force data. The average of the grinding force in the three tests was used for comparison to the predictive models.

Table 6.5 Test Conditions for grinding force validation

Test no.	V_s (m/s)	V_w (m/min)	a (μm)	Speed ratio (V_s/V_w)	Specific MRR (aV_w) (mm^{-2})	Lubrication	Material
1	31.92	2.032	15.24	942.5	0.516	Dry	AISI 1045
2	31.92	4.064	15.24	471.3	1.032	Dry	AISI 1045
3	31.92	2.032	7.62	942.5	0.258	Dry	AISI 1045
4	15.96	2.032	7.62	471.3	0.258	Dry	AISI 1045
5	31.92	2.032	15.24	942.5	0.516	MQL	AISI 1045
6	31.92	4.064	15.24	471.3	1.032	MQL	AISI 1045
7	31.92	2.032	7.62	942.5	0.258	MQL	AISI 1045
8	15.96	2.032	7.62	471.3	0.258	MQL	AISI 1045
9	31.92	2.032	15.24	942.5	0.516	Wet	AISI 1045
10	31.92	4.064	15.24	471.3	1.032	Wet	AISI 1045
11	31.92	2.032	7.62	942.5	0.258	Wet	AISI 1045
12	15.96	2.032	7.62	471.3	0.258	Wet	AISI 1045
13	23.94	1.524	15.24	942.5	0.387	Dry	AISI 1018
14	23.94	0.762	15.24	1885.0	0.194	Dry	AISI 1018

Table 6.5 continued

15	23.94	1.524	7.62	942.5	0.194	Dry	AISI 1018
16	23.94	1.524	15.24	942.5	0.387	MQL	AISI 1018
17	23.94	0.762	15.24	1885.0	0.194	MQL	AISI 1018
18	23.94	1.524	7.62	942.5	0.194	MQL	AISI 1018
19	23.94	1.524	15.24	942.5	0.387	Wet	AISI 1018
20	23.94	0.762	15.24	1885.0	0.194	Wet	AISI 1018
21	23.94	1.524	7.62	942.5	0.194	Wet	AISI 1018

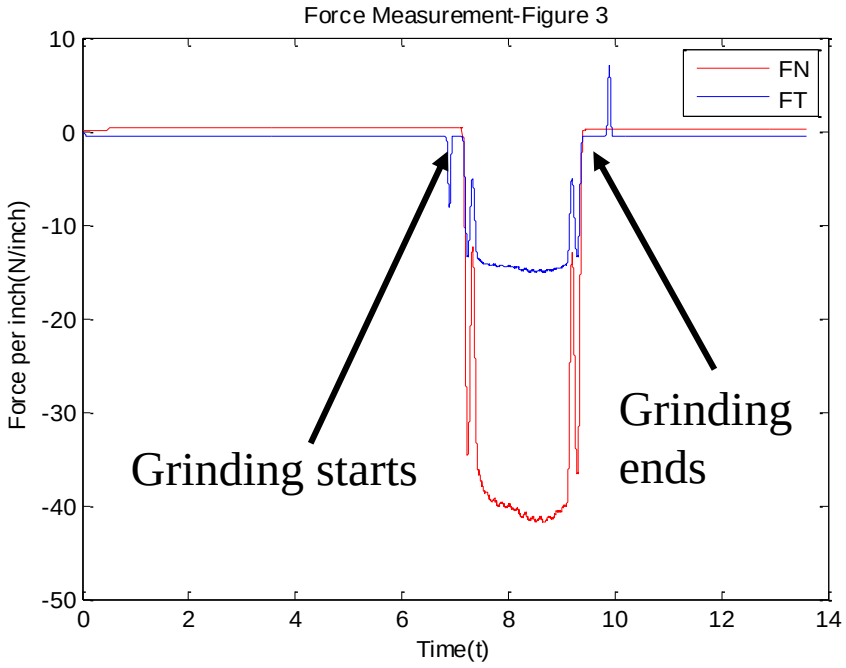

Figure 6.15 Grinding force measurement

The grinding conditions are selected in the ranges of grinding wheel speed = 15.96 m/s to 31.92 m/s, workpiece speed = 0.762 m/min to 4.064 m/min, depth of cut = 7.62 μm to 15.24 μm. The speed ratio and specific material removal rate are given in the table for reference since they are the important factors for the grinding process. The design of experiment in to investigate the individual effect of wheel speed, workpiece

speed, and depth of cut as well as the combined effect as suggested in speed ratio and specific material removal rate. The grinding wheel speed and depth of cut are selected based on the tool requirement as well as conventional parameters for finish surface grinding. The relatively low material removal rate was chosen to avoid high grinding loads for machine stiffness concerns. Due to the time and cost constraint, the other relevant parameters such as dressing conditions, types of grinding wheels, and MQL parameters have not been fully addressed by this study.

6.3.2 Grinding Test of AISI 1045 Steel

The predicted and measured tangential and normal grinding forces for the grinding tests on AISI 1045 steel are given in Table 6.6.

Table 6.6 Grinding force comparison for AISI 1045 steel

Test no.	F_t (Predicted) (N)	F_n (Predicted) (N)	F_t (Measured) (N)	F_n (Measured) (N)
1	10.79	29.77	10.91	27.28
2	19.31	59.65	32.65 (Loaded)	97.83 (Loaded)
3	5.99	15.60	5.28	14.49
4	10.99	32.55	8.65	26.55
5	8.79	22.82	8.29	26.50
6	15.10	40.97	14.01	40.60
7	4.99	12.83	5.47	16.09
8	8.69	23.06	8.71	24.52
9	8.01	22.58	8.78	22.23
10	13.72	38.56	14.60	35.21
11	4.59	12.99	4.74	13.08
12	7.81	21.88	8.65	19.62

It is observed that the forces in dry cases produces the highest grinding forces both in tangential and normal directions. The MQL condition generally produces slightly higher tangential force and similar normal forces. The prediction matches with the experimental measurements fairly well except for the dry grinding test no. 2 since the wheel loading happened and caused extra forces. The wheel loading influence will be discussed later.

From the experimental and predicted results, it is noticed that when all other conditions are the same, higher depth of cut, higher workpiece speed or lower wheel speed would results in higher tangential and normal grinding forces. This is because a higher depth of cut or higher workpiece speed all contribute to higher material removal rate, the total amount of material removed is higher and the resulting energy input would increase. A lower wheel speed or a higher workpiece speed will also result in a lower speed ratio. With a small speed ratio, less grit will be engaged and each grit would carry more load due to the increase of engagement depth. As a result, the total grinding force would increase. Another reason is higher wheel speed would lead to higher grinding zone temperature due to higher energy input, the higher temperature tend to soften the material and resulting in a smaller grinding force.

Due to the random distribution of grinding grits, the friction coefficient and single grit forces also have a distribution. The estimation of average friction coefficient, average single grit tangential and normal forces, dynamic grit density, contact length and expected value of undeformed chip thickness in the predictive model is given in Table 6.7.

Table 6.7 Model parameters in force prediction

Test no.	μ	F_{tg} (N)	F_{ng} (N)	C_d (mm^{-2})	l_c (mm)	$E(t)$ (μm)
1	0.1800	0.190	0.524	3.48	1.72	0.93
2	0.1800	0.233	0.718	4.60	1.90	1.08
3	0.1800	0.175	0.456	2.95	1.22	0.84
4	0.1800	0.221	0.654	3.91	1.34	0.99
5	0.1379	0.156	0.406	3.52	1.68	0.93
6	0.1444	0.187	0.508	4.72	1.80	1.10
7	0.1345	0.147	0.378	2.98	1.20	0.85
8	0.1418	0.178	0.472	3.99	1.29	1.00
9	0.0974	0.143	0.403	3.53	1.67	0.93
10	0.1084	0.172	0.483	4.75	1.77	1.11
11	0.0924	0.135	0.382	2.98	1.20	0.85
12	0.1030	0.161	0.451	4.02	1.27	1.00

There are two parameters need to be calibrated before the calculation. The average friction coefficient in dry grinding, which is equals to C_1 according to (3.8) and the critical undeformed chip thickness t_{cr}. Test no. 1 and 3 has been used to calibrate these two numbers, the calibrated values are: C_1 = 0.18 and t_{cr} = 1.54μm. For the average friction coefficient in dry grinding condition, two model predictions has been compared here. Base on Sin and Suh's [53] sliding sphere model, the estimated friction coefficient is around 0.1149. Based on Bhushan's [54] sliding cylinder model, the estimated friction coefficient is around 0.1348. The experimentally calibrated friction coefficient is higher than these estimations, probably due to the interaction between the chip and tool face since both of these models assumes only contact between the tool and the workpiece.

The estimation of the friction coefficient in MQL and flood cooling condition are based on the boundary lubrication theory as mentioned before. One important parameter

that needs to be determined is the adsorbed lubricant film thickness t_b . Test no. 5 and no. 9 has been chosen to calibrate the t_b under MQL and flood cooling condition. In the studied cases, under MQL condition, t_b is found to be around 0.5μm while under flood cooling condition, t_b is found to be around 1μm. Comparing to the estimation of adsorbed lubricant film thickness in machining process [52], these values are higher in the present study. The possible reason could be the porous structure of the grinding wheel could carry and store the lubricant much easier than the high pressure tool-chip interface in machining condition. Thus the lubricant film is easier to form and the thickness is increased.

The predicted and measured specific tangential forces and normal forces of the tested conditions are compared in Figure 6.16. The error range for tangential force prediction is from 0.23% to 27.05% (exclude test no. 2), and the average error is 8.13%. The error range for normal force prediction is from 0.69% to 22.60%, and the average error is 9.43%. As it can be seen from the comparison, the predicted grinding forces matches with experimental measurements very well.

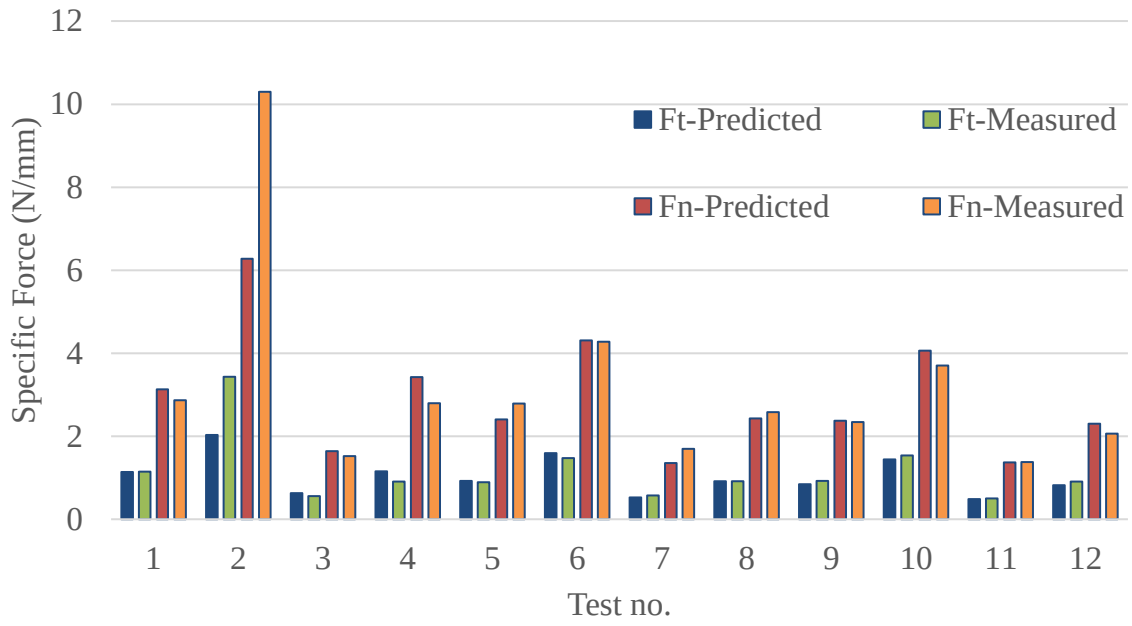

Figure 6.16 Predicted and measured forces in grinding of AISI 1045 steel

6.3.3 Grinding Test of AISI 1018 Steel

The predicted and measured tangential and normal grinding forces for the grinding tests on AISI 1018 steel are given in Table 6.8.

Table 6.8 Grinding force comparison for AISI 1018 steel

Test no.	F_t (Predicted) (N)	F_n (Predicted) (N)	F_t (Measured) (N)	F_n (Measured) (N)
13	13.99	78.02	42.21 (Loaded)	129.31 (Loaded)
14	7.86	37.30	39.22 (Loaded)	114.23 (Loaded)
15	7.74	40.26	32.97 (Loaded)	78.53 (Loaded)
16	14.92	75.42	17.42	70.06
17	8.06	35.43	11.47	42.13
18	8.15	38.60	8.54	33.56
19	11.48	39.70	13.94	39.17
20	6.15	19.70	10.85	36.26
21	6.24	22.01	6.52	19.55

Test no. 18 and no.21 was used to calibrate the model parameters assuming the same lubricant film thickness as in the previous grinding tests with AISI 1045 steel. The calibration results are: C_1 = 0.23 and t_{cr} = 1.04μm. During the experiment, the dry grinding sets all experienced severe wheel loading and resulted in extremely high force. The wheel surface images after dry, MQL and wet conditions are shown in Figure 6.17. As shown in Figure 6.17(a), the wheel surface was all covered by chips after grinding and Figure 6.17(b) shows that the clogging phenomenon was very obvious after cleaning the adhering chips. The reason maybe that the friction coefficient between AISI 1018 and the grit is high and the single grit forces are large. The higher energy input in the grinding zone results in high temperature generation. Plus the fact that the melting point of AISI 1018 is significantly lower than AISI 1045, at a higher temperature, the chips are easier to clog the wheel pores. Since the wheel surface is severely clogged and covered by metal chips, there is no active cutting actions but only excessive friction between the loaded wheel and the workpiece. Comparing to dry condition, the high pressure air flow and oil lubrication in MQL grinding removed the chips efficiently.

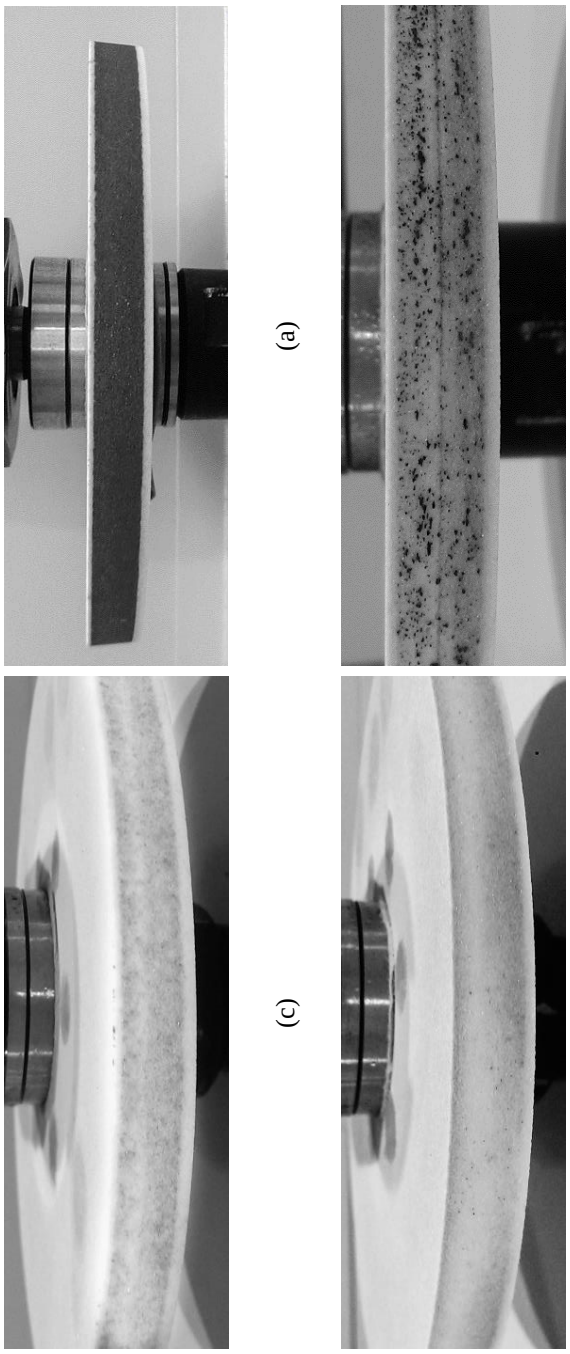

Figure 6.17 Grinding wheel loading (a) after dry grinding, (b) after cleaning the chips in dry grinding, (c) after MQL grinding, (d) after flood cooling grinding

The estimation of average friction coefficient, average single grit tangential and normal forces, dynamic grit density, contact length and expected value of undeformed chip thickness in the predictive model is given in Table 6.9. Due to the significantly

higher friction coefficient, the tangential and normal forces in MQL condition are higher than that of flood cooling conditions.

Table 6.9 Model parameters in force prediction

Test no.	μ	F_{tg} (N)	F_{ng} (N)	C_d (mm^{-2})	l_c (mm)	$E(t)$ (μm)
13	0.2300	0.225	1.257	3.25	2.01	0.89
14	0.2300	0.206	0.979	2.25	1.78	0.71
15	0.2300	0.207	1.077	2.77	1.42	0.81
16	0.1906	0.244	1.231	3.29	1.96	0.89
17	0.1823	0.194	0.852	2.50	1.75	0.77
18	0.1851	0.214	1.018	2.81	1.42	0.82
19	0.1402	0.198	0.758	3.43	1.78	0.92
20	0.1213	0.152	0.488	2.56	1.66	0.78
21	0.1357	0.177	0.623	2.86	1.30	0.83

The predicted and measured specific tangential forces and normal forces of the tested conditions are compared in Figure 6.18. The error range for tangential force prediction is from 4.29% to 43.32% (exclude test no. 13, no. 14 and no. 15), and the average error is 18.98%. The error range for normal force prediction is from 7.65% to 45.67%, and the average error is 16.36%. The biggest prediction errors are found in flood cooling condition. The possible reason may be the neglect of the hydrodynamic force induced by the coolant flow. Another reason maybe the misinterpretation of boundary lubrication theory in predicting friction coefficient in flood lubrication since the frictional behavior may not be the same as in MQL condition.

It is concluded from the experimental validation that by using boundary lubrication theory, the grinding forces under MQL condition has been accurately

predicted. However, the validity of boundary lubrication may not hold in flood cooling as large differences between experimental and predicted results have been noticed.

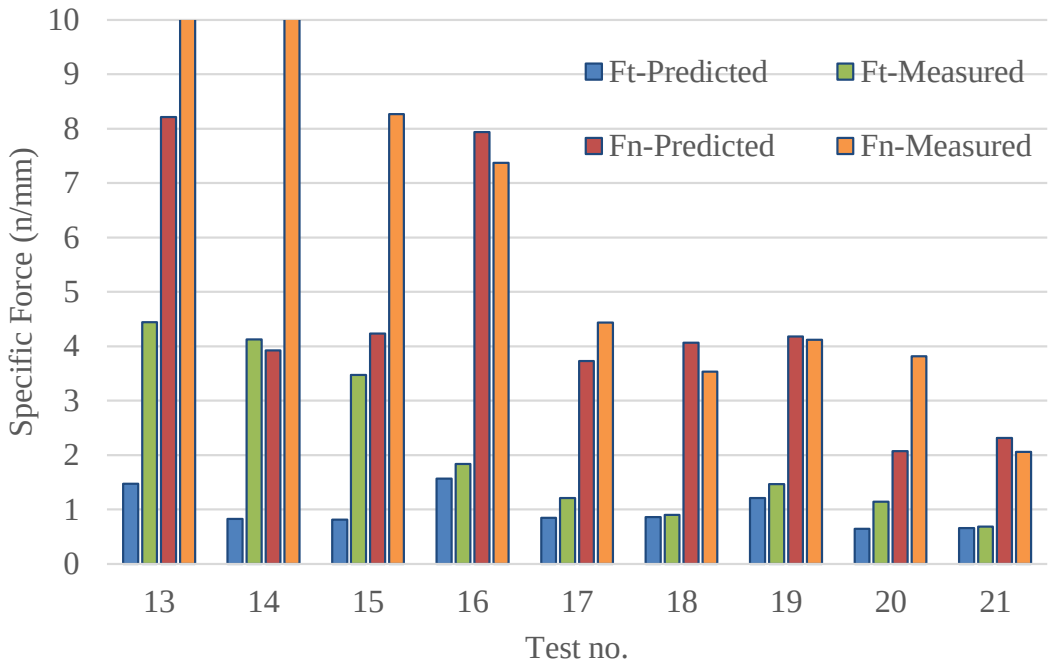

Figure 6.18 Predicted and measured forces in grinding of AISI 1018 steel

6.4 Grinding Temperature Validation

6.4.1 Estimation of MQL heat transfer coefficient

The validation of grinding temperature is verified by measuring the temperature in the workpiece with thermocouple or thermal camera. Before calculating the temperature, the thermal properties of the air-oil mixture should be estimated based on the two-phase homogeneous flow as described in section 4.2. The thermal properties of the coolant and air used in this study is given in Table 6.10.

Table 6.10 Properties of air and oil

Material	Thermal conductivity (W/m K)	Density (kg/m^3)	Specific heat (J/kg K)	Dynamic viscosity (Pa s)
Air	0.026	1.16	1007	1.8e-5
Vegetable oil	0.17	980	1675	38.63e-3

The diameter of nozzle used in the experiment was measured to be 0.762 mm. The volumetric flow rate of the air flow can be related to air pressure based on (4.17) and (4.18). The calculated results are given in Table 6.11. The volumetric flow rate of the MQL lubricant is directly controlled by the MQL system. The MQL lubricant flow rate is 1.1e-7 m^3/s. Based on these parameter, the density, dynamic viscosity, thermal conductivity and specific heat capacity of the two-phase air-oil flow is calculated in Table 6.12.

Table 6.11 Volumetric flow rate and jet speed at the nozzle exit for MQL condition

Air pressure	2	3	4	5	6
Volumetric flow rate $\dot{V}_g$ (m^3/s)	0.085e-3	0.104e-3	0.120e-3	0.134e-3	0.147e-3
Jet speed (m/s)	186	227	262	294	322

Table 6.12 Properties of air-oil mixture

Material	Thermal conductivity (W/m K)	Density (kg/m^3)	Specific heat (J/kg K)	Dynamic viscosity (Pa s)
Air	0.041	2.06	1036	3.19e-5

In order to estimate the convection heat transfer coefficient of air-oil mixture h_f, the Nusselt number, Prandtl number, and Reynolds number need to be calculated. The

heat transfer coefficient in flood cooling conditions is assumed to be around 40,000 W/(m^2 K) based on [3]. In dry grinding condition, the heat loss is removed from the prediction model. For the MQL conditions (test no. 5-8 and no. 16-18), the estimation of the parameters related to heat transfer coefficient are shown in Table 6.13. The estimations agrees with Hadad's work [22].

Table 6.13 Estimation of MQL heat transfer coefficient

Test no.	Reynolds number	Prandtl number	Nusselt number	h_f (W/(m^2 K)
5	968	8.02	38.85	955
6	1033	8.02	40.12	925
7	692	8.02	32.85	1129
8	643	8.02	30.21	969
16	1053	8.02	39.76	839
17	977	8.02	38.29	871
18	736	8.02	33.25	1003

6.4.2 Temperature Validation

In order to validate the grinding temperature distribution, two method are discussed here: thermal camera and thermocouple measurement. A typical thermal camera measurement is shown in Figure 6.19 and a typical thermocouple measurement is shown in Figure 6.20.

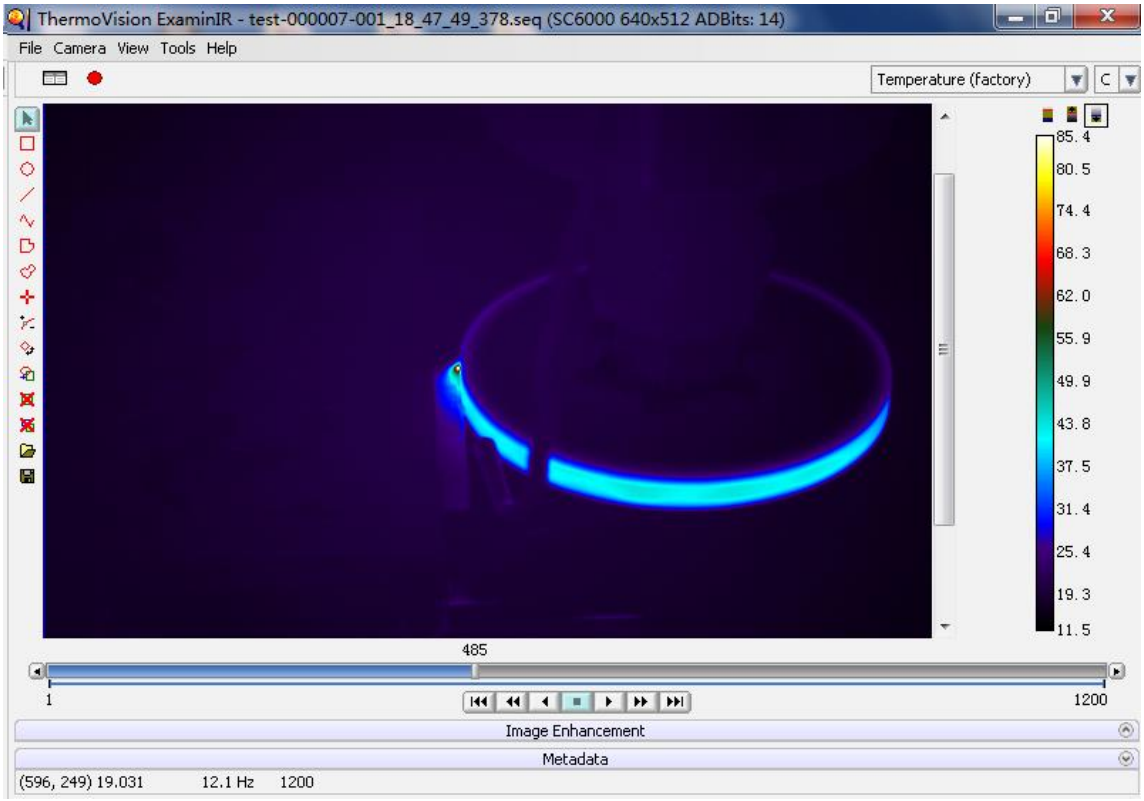

Figure 6.19 Thermal camera measurement

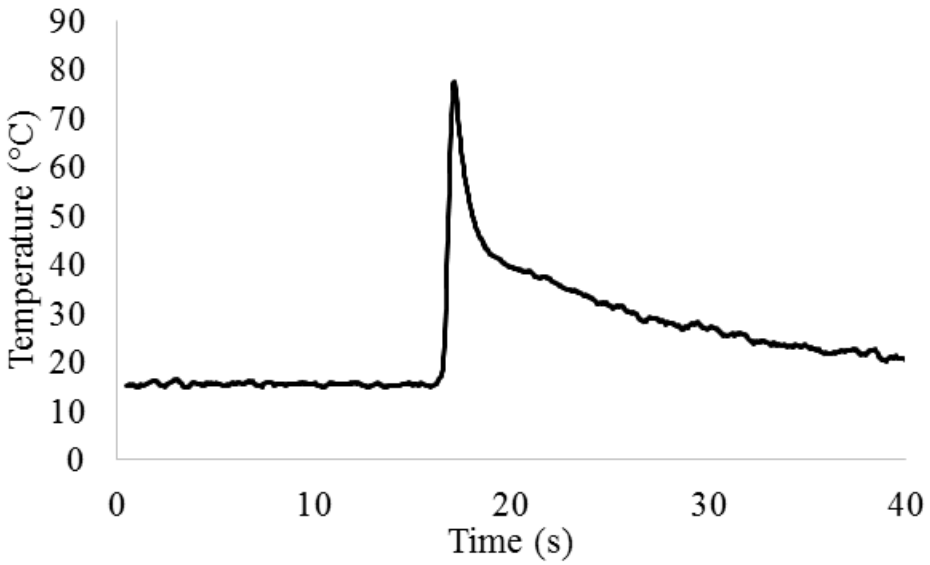

Figure 6.20 Thermocouple measurement

The advantage of thermal camera is the capability of capturing real time temperature field. It is a direct measurement of the temperature distribution in the workpiece while the thermocouple is recording the temperature history. The thermocouple provides much more information than the thermocouple measurements since the thermocouple could only measure the temperature at a certain depth and is very difficult to measure the temperature near the workpiece surface. The major limitation of thermal camera measurement is that it is hard to place the camera close enough to the grinding zone. Besides, it can't be used for flood cooling condition measurement since the coolant would block the infrared light. Since the resolution of the camera is only 640*512, only a rough comparison could be made due to the poor thermal image quality. An example is given here of comparing the predicted and measured temperature distribution in the workpiece for test no. 17. The rest of the temperature validation will be based on thermocouple measurements at 1.5mm depth.

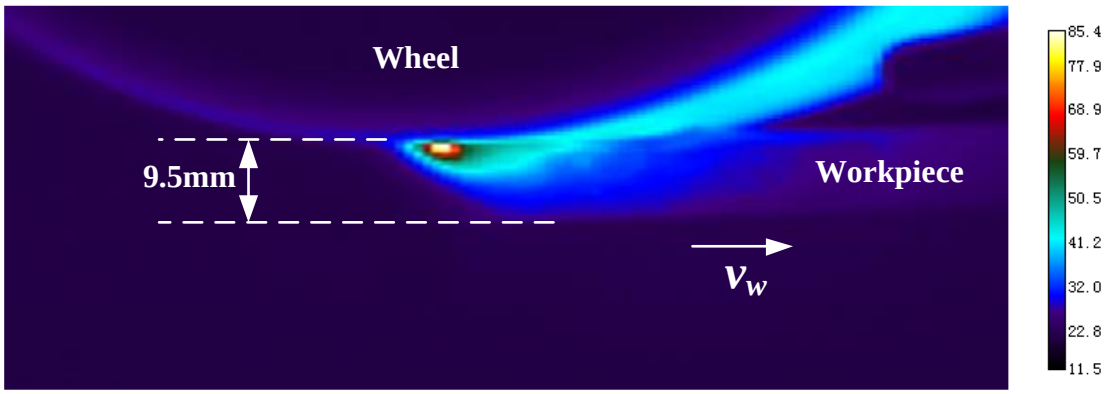

(a) Thermal camera measurement

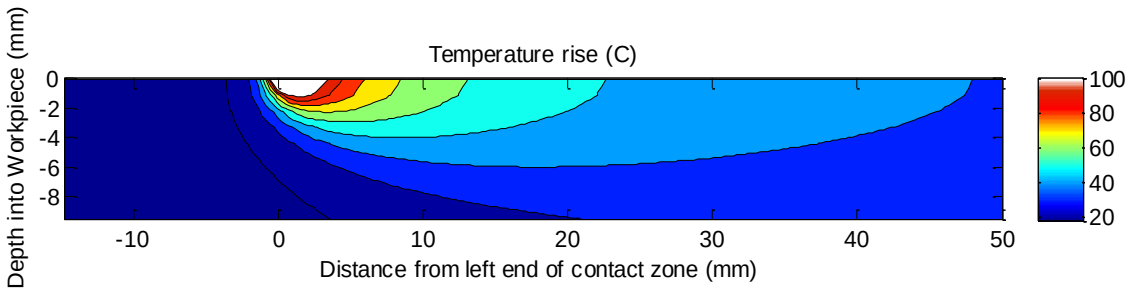

(b) Model prediction

Figure 6.21 Comparison between prediction and thermal camera measurement of temperature field of test no. 17

In Table 6.14 shows the comparison of temperature rise at 1.5mm depth between experimental and simulation and the estimated maximum temperature rise at the workpiece surface and energy partition ratio to the workpiece.

Table 6.14 Comparison between predicted and measured max temperature rise

Test no.	Energy partition ratio to the workpiece	Predicted total energy generation (W)	Predicted surface temperature rise (°C)	Predicted temperature rise at 1.5mm depth (°C)	Measured temperature rise at 1.5mm depth (°C)
1	0.808	344.4	331.7	70.7	65.7
2 (Loaded)	0.811	616.3	433.5	65.6	123.6
3	0.813	191.2	214.0	39.3	33.7
4	0.784	175.4	180.1	34.4	28.3
5	0.791	280.6	272.3	55.9	47.2
6	0.784	482.0	342.0	49.6	40.2
7	0.789	159.3	175.2	32.0	25.7
8	0.750	138.7	135.6	26.3	19.4
9	0.433	255.7	133.6	27.5	12.6
10	0.471	437.9	186.1	27.4	9.7
11	0.486	146.5	98.2	18.0	5.8
12	0.437	124.6	76.2	13.4	3.7

Table 6.14 continued

13 (Loaded)	0.832	334.9	397.2	100.2	185.1
14 (Loaded)	0.839	188.2	286.5	92.9	296.7
15 (Loaded)	0.838	185.3	244.8	57.5	126.4
16	0.824	357.2	365.6	95.1	86.3
17	0.816	192.9	252.7	86.0	77.0
18	0.821	195.1	226.1	51.5	36.4
19	0.407	274.8	147.2	37.1	12.4
20	0.365	147.2	85.3	28.1	11.2
21	0.470	149.4	96.0	21.2	5.5

From the predicted values, it is found that dry grinding would generate the highest grinding temperature and flood cooling the lowest under the same conditions. The Energy partition of dry grinding is from 0.784 to 0.839 depends on the grinding conditions, comparing to 0.784 - 0.824 of MQL grinding and 0.365 – 0.486 of flood cooling. Although the heat partition ratio in MQL is very close to dry grinding, the total grinding power is reduced due to lubrication effect. The predicted temperature rise for MQL condition is 5.1% to 24.4% less than the dry grinding. Conventional flood cooling generates 44.8% to 67.3% lower temperature than MQL grinding due to the superior cooling action of abundant fluid.

The comparison between predicted and measured temperature rise is shown in Figure 6.22. The predictions in test no. 2 and no. 13-15 are very low compare to the measurement due to excessive friction heat generation caused by wheel loading. The predictions for flood cooling conditions are generally much higher than the measured temperature rise. The reason may be that the workpiece used in the experiment is very

small and the side flow could take away most of the heat conducted into the workpiece. The error range for the predictions of MQL conditions (test no. 5-8 and 16-18) is from 10.20% to 41.48%, and the average error is 23.61%.

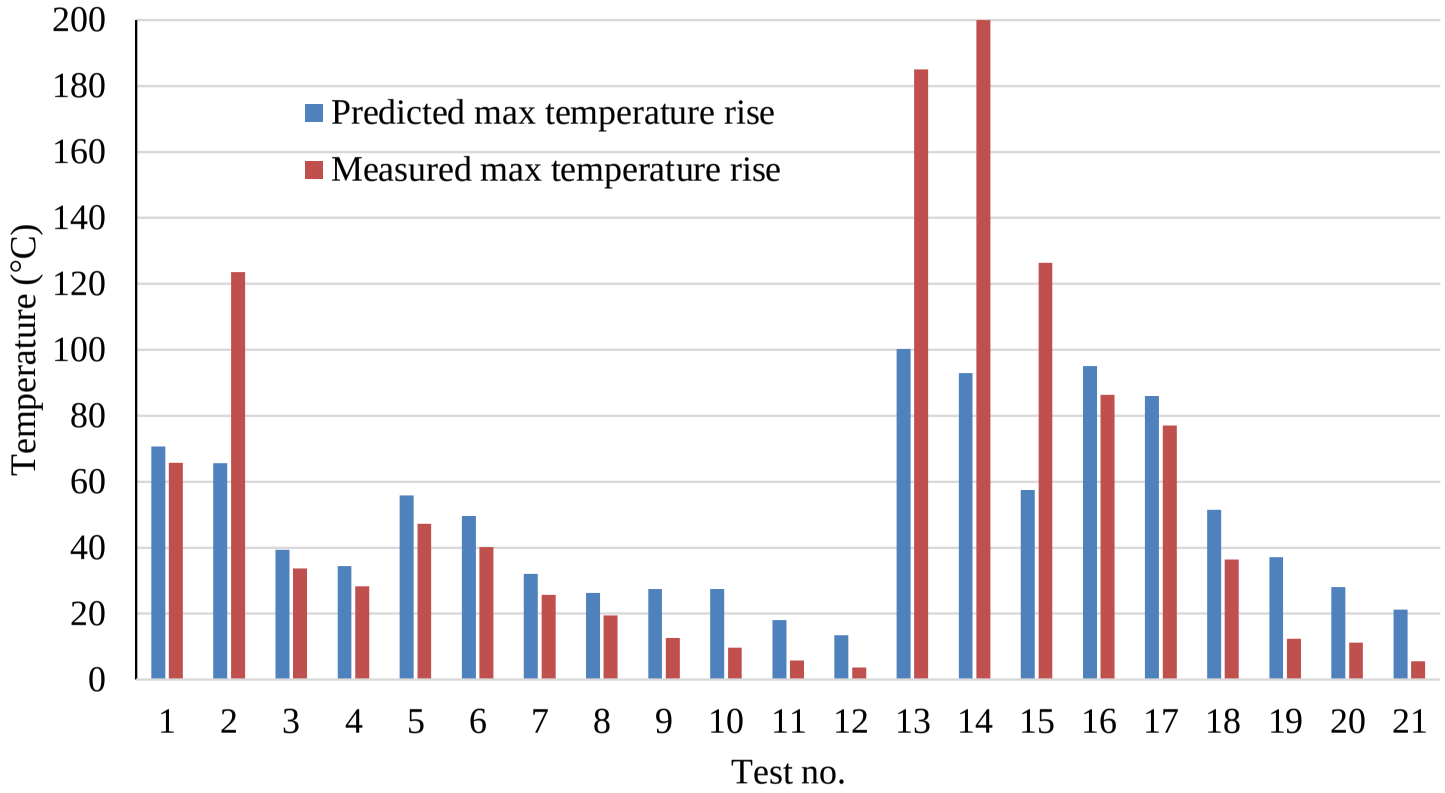

Figure 6.22 Comparison between prediction and thermocouple measurement

6.5 Residual Stress Validation

6.5.1 Validation of Residual Stress Profile

The validation of residual stress is verified by comparing the predicted residual stress results with XRD measurements and by comparing the predicted tensile stress transitional temperature with literature. Due to the time and cost constraint, only 9 test sets (test no. 13-21) with AISI 1018 steel have been selected for residual stress profile validation. The tensile stress versus grinding temperature data is extracted from the literature [28].

6.5.1.1 Dry grinding

It is noticed that due to the wheel loading, the measured grinding force and temperature are much higher than the model prediction. Thus the residual stress under these conditions are calculated based on the mechanical and thermal loading stress estimation from the measured force and temperature.

The comparison between predicted and measured residual stress profile for test no. 13 is shown in Figure 6.23. The predicted maximum tensile residual stress in tangential direction is 642MPa, and the maximum tensile residual stress in traverse direction is 282MPa. Both agrees with experimental measurement. The general trend and magnitude of the residual stress predictions in tangential and normal directions are in consistent with the measured results. Very high tensile residual stress appeared near the surface due to the extremely high temperature generated.

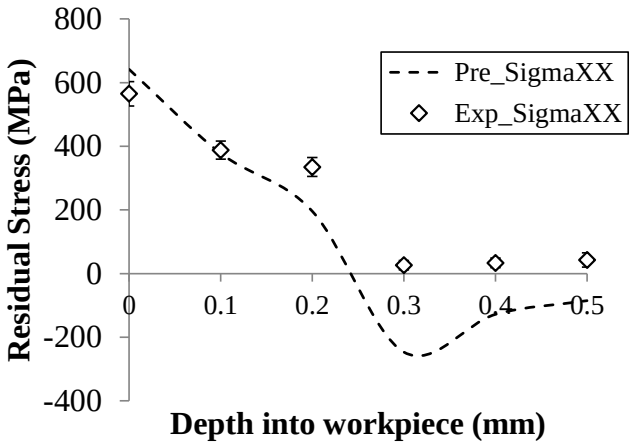

(a) Tangential direction

5

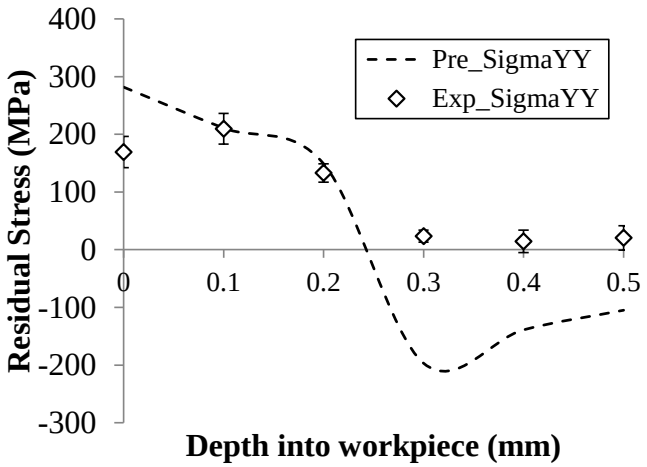

(b) Normal direction

Figure 6.23 Comparison of residual stresses in experiment and simulation of test no. 13

The comparison between predicted and measured residual stress profile for test no. 14 is shown in Figure 6.24. The predicted maximum tensile residual stress in tangential direction is 582MPa, and the maximum tensile residual stress in traverse direction is 176MPa. Both agrees with experimental measurement. The predicted residual stress profile has a larger tensile residual stress depth than the measured profile. The

difference may due to phase transformation near the surface triggered by high temperature or the oxidation layer formed at high grinding temperature. The general trend and magnitude of the residual stress predictions in tangential and normal directions are in consistent with the measured results.

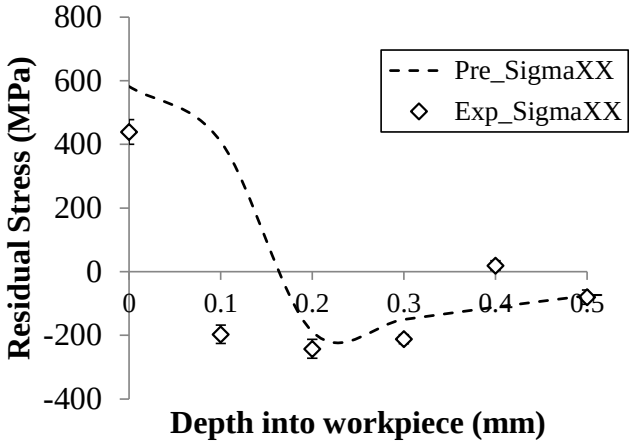

(a) Tangential direction

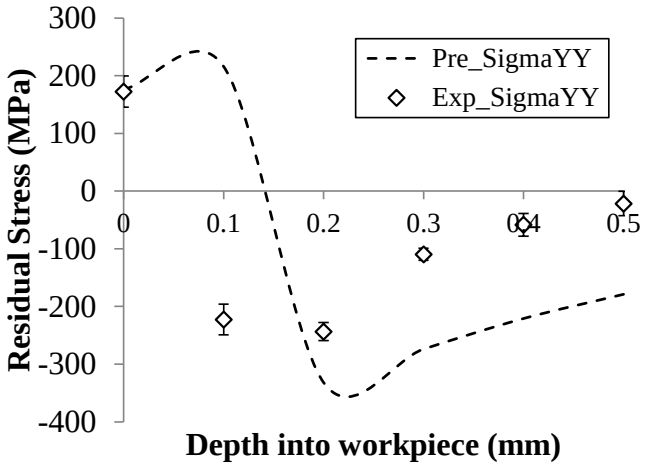

(b) Normal direction

Figure 6.24 Comparison of residual stresses in experiment and simulation of test no. 14

The comparison between predicted and measured residual stress profile for test no. 14 is shown in Figure 6.25. The predicted maximum tensile residual stress in tangential direction is 500MPa, and the maximum tensile residual stress in traverse direction is 311MPa. Both agrees with experimental measurement. The general trend and magnitude of the residual stress predictions in tangential and normal directions are in consistent with the measured results.

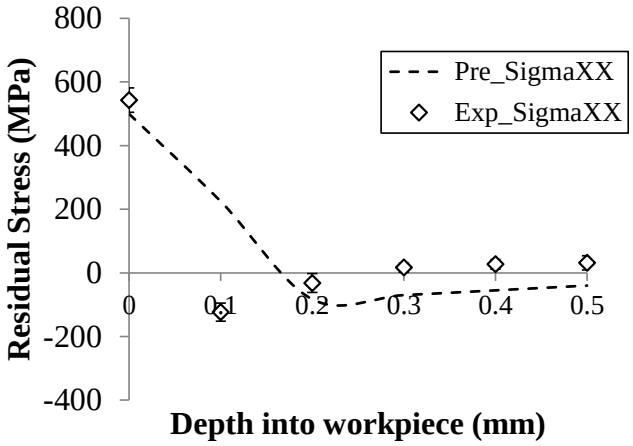

(a) Tangential direction

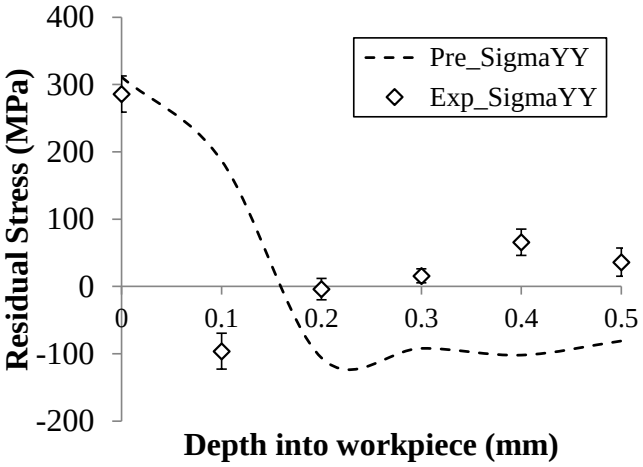

(b) Normal direction

Figure 6.25 Comparison of residual stresses in experiment and simulation of test no. 15

It is concluded that in dry grinding due to wheel loading, it has generated very high tensile residual stress near the surface area which will impair the surface quality of the workpiece. The high temperature is the dominant factor for the tensile residual stress. The predictive model have successfully captured the trend and magnitude of the residual stress distribution in the workpiece.

6.5.1.2 MQL grinding

The comparison between predicted and measured residual stress profile for test no. 13 is shown in Figure 6.26. The predicted maximum compressive residual stress in tangential direction is -221MPa, and the maximum compressive residual stress in traverse direction is -342MPa. The residual stresses approaches to 0 near 0.3μm. The general trend and magnitude of the residual stress predictions in tangential and normal directions are in consistent with the measured results. It is observed that, different from dry grinding, the compressive residual stresses are generated on the workpiece surface. The efficient lubrication and cooling have limited the temperature generation and the mechanical effect plays a dominant role in generating compressive residual stresses. The subsurface tensile stresses may be attribute to the thermal effect since the mechanical stress only influences up to 0.05μm depth.

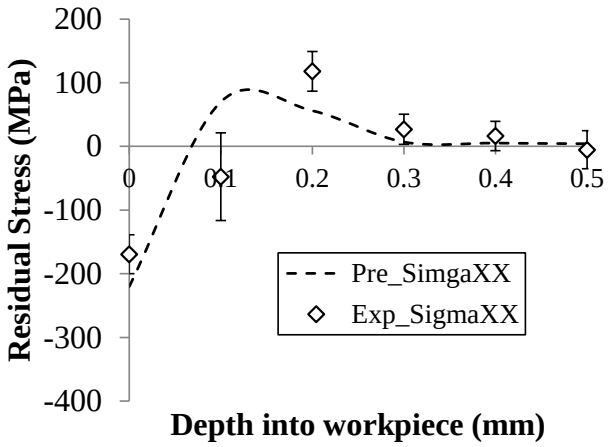

(a) Tangential direction

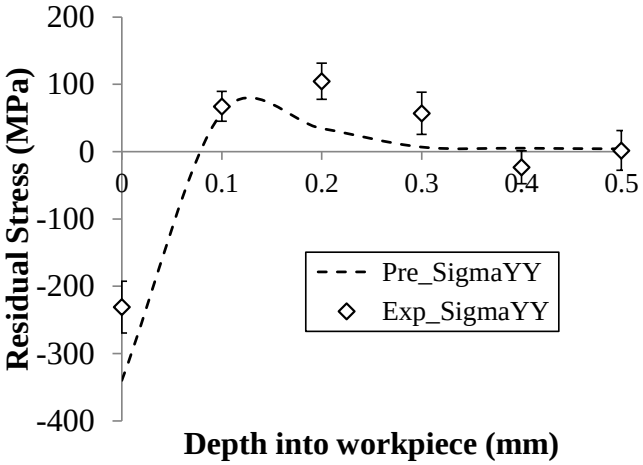

(b) Normal direction

Figure 6.26 Comparison of residual stresses in experiment and simulation of test no. 16

The comparison between predicted and measured residual stress profile for test no. 13 is shown in Figure 6.27. The predicted maximum compressive residual stress in tangential direction is -268MPa, and the maximum compressive residual stress in traverse direction is -402MPa. The residual stresses approaches to 0 near 0.2μm. Comparing to test no. 16, the tensile residual stress in the subsurface area is much smaller since the grinding temperature in test no. 17 is lower. The general trend and magnitude of the

residual stress predictions in tangential and normal directions are in consistent with the measured results.

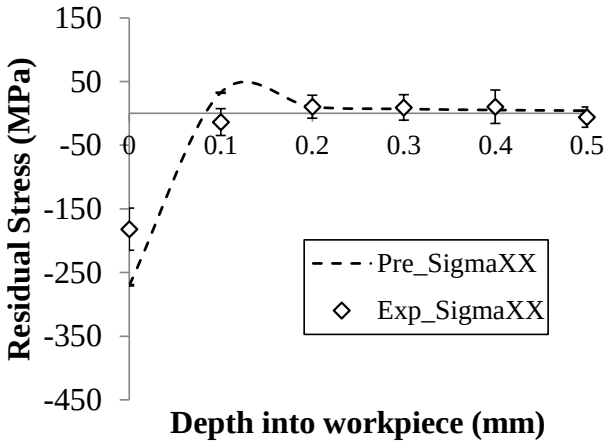

(a) Tangential direction

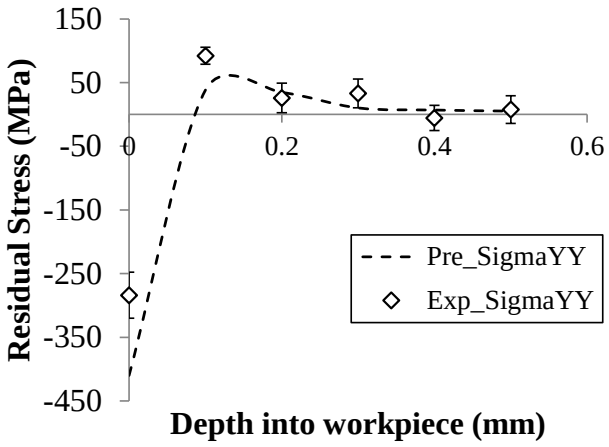

(b) Normal direction

Figure 6.27 Comparison of residual stresses in experiment and simulation of test no. 17

The comparison between predicted and measured residual stress profile for test no. 13 is shown in Figure 6.28. The predicted maximum compressive residual stress in tangential direction is -263MPa, and the maximum compressive residual stress in traverse

direction is -375MPa. Both agrees with experimental measurements. It is observed that the tensile residual was eliminated in test no. 18 since the grinding temperature was too low to trigger any plastic deformation. The general trend and magnitude of the residual stress predictions in tangential and normal directions are in consistent with the measured results.

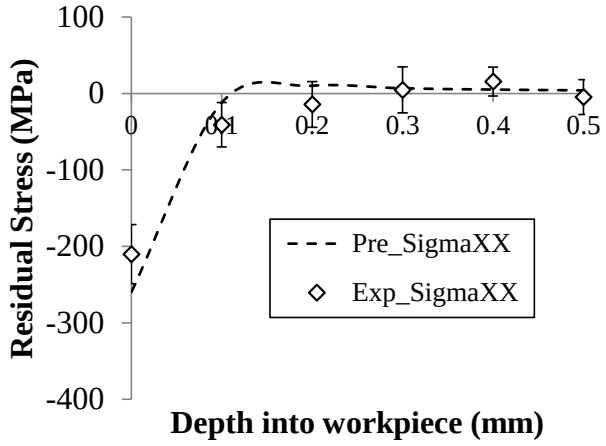

(a) Tangential direction

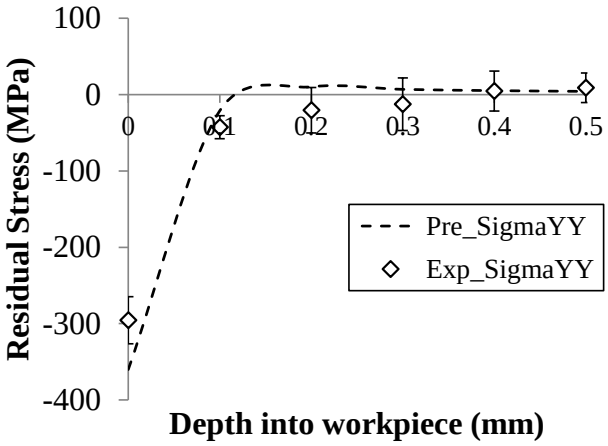

(b) Normal direction

Figure 6.28 Comparison of residual stresses in experiment and simulation of test no. 18

6.5.1.3 Flood cooling grinding

Since the behavior of residual stress profile in flood cooling is very similar, they are discussed together here. In flood cooling grinding, similar to test no. 18, the tensile residual stresses are eliminated due to the low temperature rise. The general trend and magnitude of the residual stress predictions in tangential and normal directions are in consistent with the measured results.

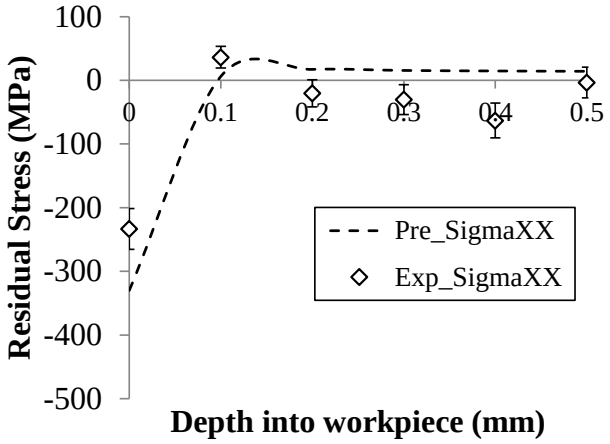

(a) Tangential direction

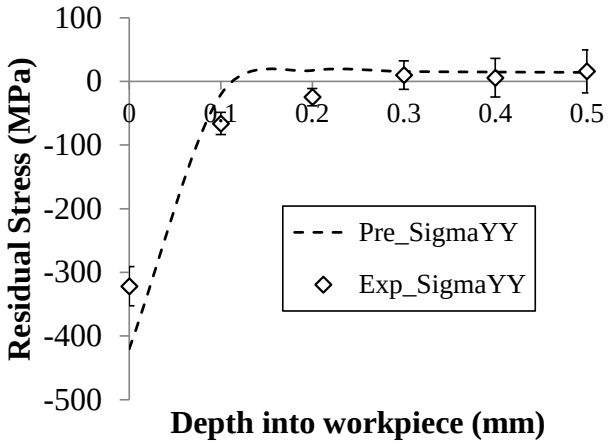

(b) Normal direction

Figure 6.29 Comparison of residual stresses in experiment and simulation of test no. 19

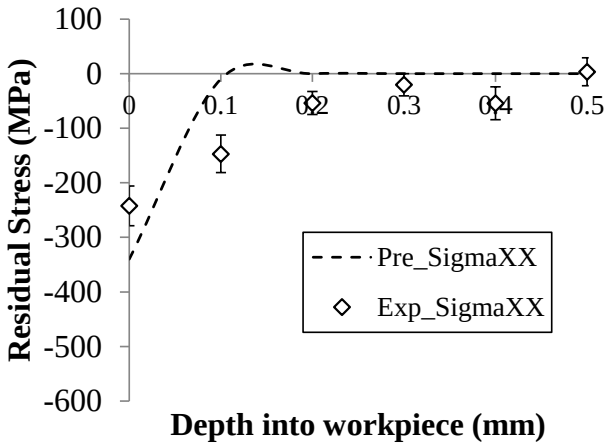

(a) Tangential direction

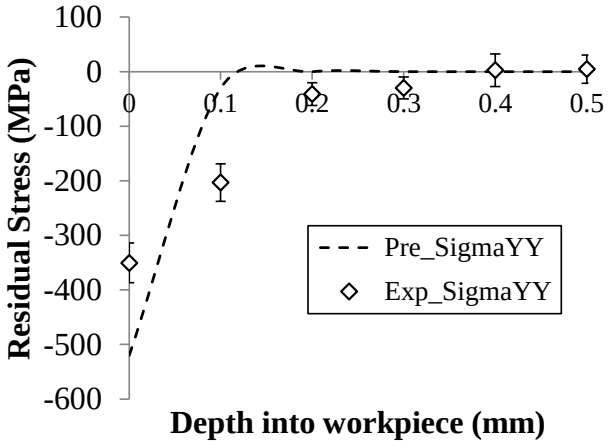

(b) Normal direction

Figure 6.30 Comparison of residual stresses in experiment and simulation of test no. 20

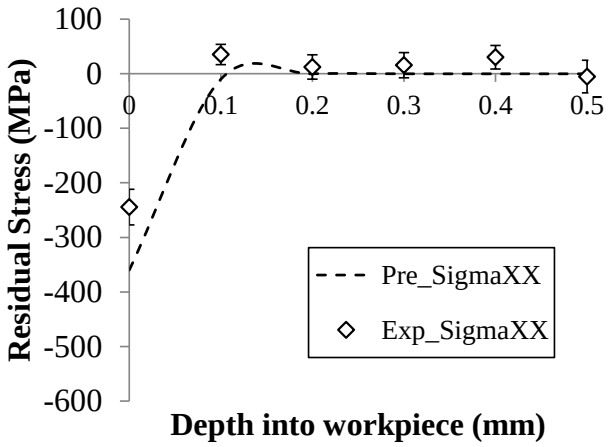

(a) Tangential direction

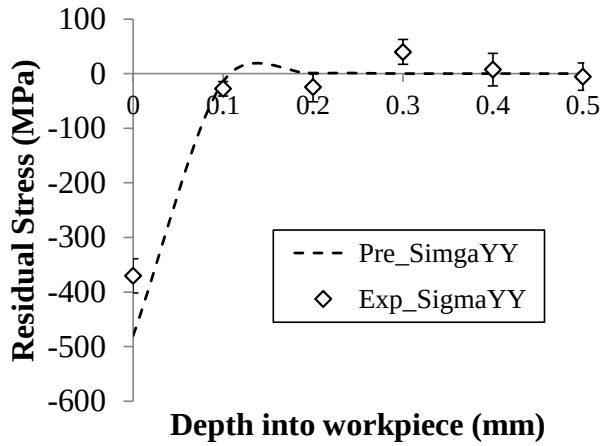

(b) Normal direction

Figure 6.31 Comparison of residual stresses in experiment and simulation of test no. 21

It can be seen from the comparison that prediction results agree with experimental measurements reasonably well in both dry, MQL and flood cooling situations. Several remarks are made here:

1) High tensile residual stresses were generated in dry grinding. It is mainly due to the high temperature caused by wheel loading. The influence of thermally induced stress exceed the effect of mechanical stress and results in high tensile residual stresses.

2) Surface residual stresses in MQL and flood cooling conditions are compressive in the studied circumstances. The reason is that mechanical stress on the workpiece surface took the dominant position under these conditions while the surface temperature is not very high. It is suggested in previous studies [28] that a critical temperature exists for the transition from compressive to tensile surface residual stress. When the surface temperature exceeds the critical point, tensile residual stress will be generated on the workpiece surface. Due to the fact that MQL generates much higher surface temperature [83] under same grinding parameters, it is expected that lower material removal rate is needed to reach transitional temperature for MQL grinding comparing to flood cooling. This is indicated in this study by that the residual stresses are more “tensile” in MQL condition which represents the thermal effect on the surface residual stress.

3) Moderate tensile stresses were generated in the subsurface area in MQL grinding of test no. 16 and no. 17. The reason is that thermally induced stress could affect deeper subsurface areas while the mechanical stress affected areas are localized and very close to the surface. Since the temperature effect is negligible in test no. 18-21, tensile residual stress are almost eliminated in the subsurface areas.

4) The larger material removal rate in test no. 16 and no. 19 results in a larger grinding energy and temperature under MQL condition. Consequently, the residual stresses are more “tensile” in test no. 16 and no. 19 comparing to test no. 17, 18 and no.

20, 21. However, the effect of large material removal rate under flood cooling condition is not obvious since the temperature is not high enough to induce large thermal stresses.

6.5.2 Validation of Transitional Temperature for Tensile Residual Stress

During the grinding process, the residual stresses generation process is slightly different from other manufacturing process such as machining. The large amount of heat generated is playing a key role in the definition of the type of residual stresses. As presented in the previous section, the residual stress profile become more tensile with the increasing temperature. It is expected that when the temperature reaches a threshold value called tensile onset temperature [28], the thermal effect would exceed the effects of mechanical loading and generate tensile residual stress on the surface. The tensile onset temperature is the temperature beyond which the residual stress generated in ground surface is tensile.

The proposed model was validated by the experimental results obtained by [27]. The same cutting conditions and materials systems were implemented in both model-prediction and experimentation. Grinding tests were carried out on one side of each sample on an Abwood HS5025CP grinding machine. An aluminum oxide wheel was used. Three wheel speeds (Vs = 20, 30 and 40ms^{-1}) and three workpiece speed (Vw = 0.1, 0.2 and 0.3ms^{-1}) were used. Depths of cut were in the range 0.53–10.63μm. Table 6.15 and Table 6.16 present the material physical properties and Johnson-Cook flow stress model coefficients that were used in the computational implementation from [84].

Table 6.15 Material properties for AISI 52100

Material	E (GPa)	ν	H (Brinell)	ρ (kg/m^3)	k (W/m ℃)	C_P (J/kg ℃)	α (℃$^{-1}$)	T_m (℃)
AISI 52100	200	0.29	183	7833	46.6	475	11e-6	1480

Table 6.16 Johnson-Cook parameters for AISI 52100

Material	A (MPa)	B (MPa)	n	C	m
AISI 52100	775	134.5	0.371	0.0173	3.17

The grinding force and power were calculated based on the grinding parameters and the heat partition into the workpiece was calibrated using the maximum grinding zone temperature. Figure 6.32 and Figure 6.33 shows the obtained results.

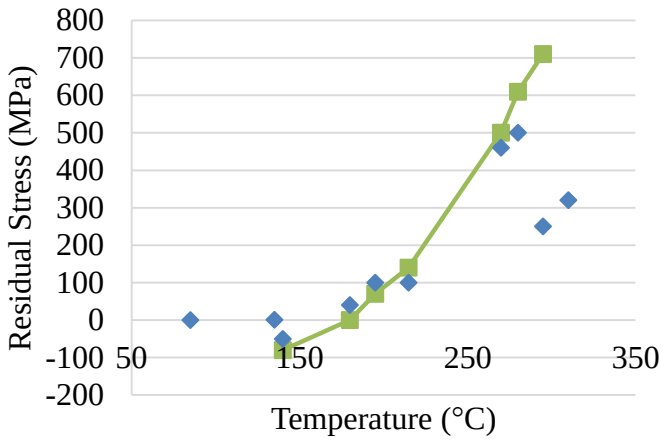

Figure 6.32 Residual stress vs. grinding temperature in tangential direction

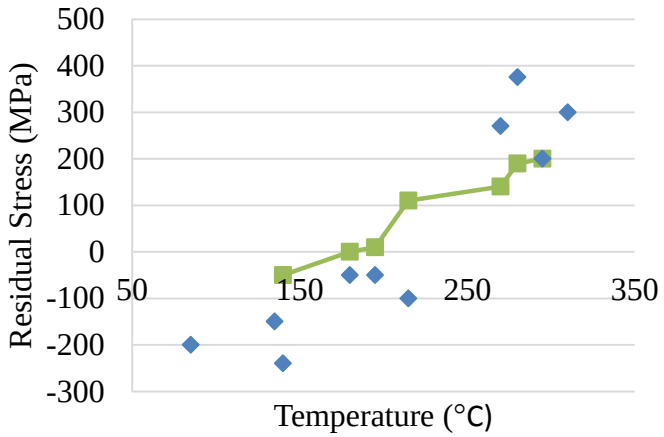

Figure 6.33 Residual stress vs. grinding temperature in traverse direction

As shown in Figure 6.32 and Figure 6.33, it can be observed that the onset temperature for the hardened steel AISI 52100 was 190 °C for both traverse and cutting directions. The model-based simulations agree with the experimental data of surface residual stresses under different grinding temperature. The model-experimental comparison further justifies the fact that thermally induced stresses rather than mechanical stresses has a great effect on the tensile residual stress generation.

6.6 Summary

In this chapter, the predictive models developed through Chapters 3~5 is validated by experiments.

In section 6.1, the experimental setup is described. The static characteristics of the grinding wheel is first measured by interferometry. The grinding forces and temperature in the workpiece is recorded by dynamometer and thermocouple/thermal camera during

the grinding process. The residual stresses are finally measured by x-ray diffraction technique.

In section 6.2, some of the important parameters is determined. The wheel and workpiece mechanical and thermal properties are extracted from literature. Wheel surface characterization including the grit geometry and distribution is then discussed. Followed by the parameter characterization in boundary lubrication.

Section 6.3 and 6.4 gives the grinding force and temperature validation results. The influence of different materials, process conditions and lubrication conditions has been pursued. Section 6.5 describes the residual stress measurement results. The measured residual stress profile agrees with model predictions.

CHAPTER 7

SURFACE CHARACTERISTICS MODELING

In grinding of high performance ceramics, lowering grinding costs by using faster removal rates is constrained mainly by surface damage to the ceramic workpiece which leads to strength degradation. Developing of methodologies for selecting process parameters requires a fundamental knowledge of the prevailing grinding mechanisms and their influence on the resulting surface finish and mechanical properties. A quantitative analysis is required for the process planning and optimization to maximize removal rate while controlling surface integrity in grinding of high performance ceramics. In this chapter, an analytical approach has been proposed to estimate the surface characteristics in ceramic grinding by applying indentation fracture mechanics analysis to realistic grinding operations.

The surface roughness prediction model is developed based on the ductile-brittle mixed surface generation mechanism in ceramic grinding. The lateral crack system has been utilized to calculate the brittle mode surface roughness generation. In addition to surface roughness prediction, a model describing the strength degradation in ceramic grinding is proposed. The median crack system combined with grinding kinematics model is used to predict the strength degradation due to surface damage introduced by grinding process.

7.1 Ceramic Grinding Mechanism

7.1.1 Indentation Fracture Mechanics Models

The grinding mechanism of ceramic materials is shown to be a combination of ductile flow and brittle fracture [4]. Since brittle material removal is analogous to indentation of the brittle material by a hard indentor, the indentation fracture mechanics models have been utilized to predict the crack generation and propagation due to individual grit in grinding. Two crack systems have been identified by Lawn et al. [44] and Marshall et al. [45]. These calculations have built a solid physics foundation to the problems that are aimed to solve in this chapter. A short introduction is given here.

From indentation fracture observations, two principal crack systems emanate from the plastic zone directly under the indentor as shown in Figure 7.1.

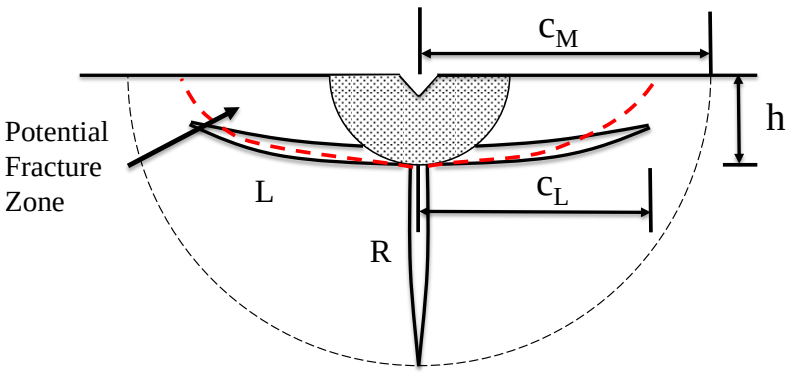

Figure 7.1 Stress resulting from single grit interaction at grit scale

Median/radial cracks are usually associated with strength degradation, and lateral cracks with material removal [4]. The characteristics of the lateral crack system such as

lateral crack size, c_L, and plastic zone depth, h, can be calculated from process parameters and material properties [45]. The lateral crack size, c_L, is given as:

$$c_L = c^l \left[1 - \left(\frac{P_0}{P} \right)^{1/4} \right]^{1/2} \tag{7.1}$$

where

$$P_0 = \left(\frac{\zeta_0}{A^2} \right) (\cot\psi)^{-2/3} \left(\frac{K_c^4}{H^3} \right) \left(\frac{E}{H} \right) \tag{7.2}$$

$$c^l = \left\{ \zeta_L (\cot\psi)^{5/6} A^{-1/2} (K_c H)^{-1} E^{3/4} \right\}^{1/2} P^{5/8} \tag{7.3}$$

The plastic zone depth, h, is given as:

$$h = k \left[\frac{E^{1/2}}{H} \right] (\cot\psi)^{1/3} P^{1/2} \tag{7.4}$$

where E is the elastic modulus, K_c is the fracture toughness, H is the hardness, ζ_0, ζ_L, A are constants, k is also a constant calibrated from experiments. P is the single grit load which can be modeled from [85]:

$$P = \beta' \left(\frac{K_c^{1/2} H}{E^{2/5}} \right) \left(\frac{4t^2 l_c C_d \tan(\theta)}{\pi} \right)^{3/4} a_e^{-1/2} \tag{7.5}$$

where β' is the constant that includes information related to the wheel topography. The typical value of constants used in the calculation is listed in Table 7.1.

Table 7.1 Constants in lateral crack system [45]

Constants	β'	ζ_0	ζ_L	A	ψ
Typical value	0.85	1.2×10^3	25×10^{-3}	0.75	75°

On the other hand, median crack size is also related to normal loading *P*. Additionally, the tangential load *P'* is also shown to be important on the crack propagation [46]. The ratio of tangential to normal load is shown to have a strong influence on the median crack size propagation in the plane of motion ($\Phi = 0°$) as shown in Figure 7.2 while have almost no influence on the median crack size in the plane perpendicular to the motion ($\Phi = 90°$).

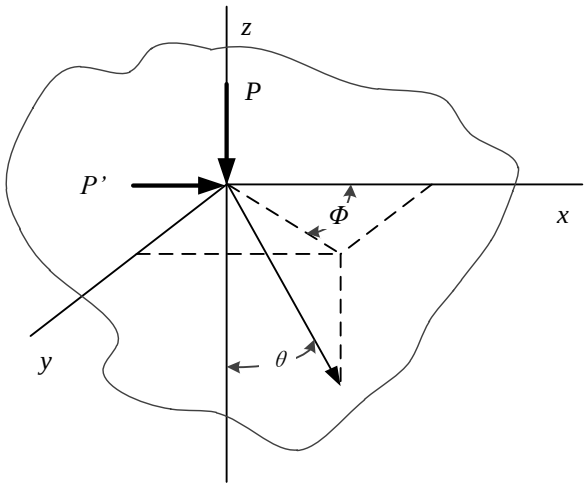

Figure 7.2 Coordinate system under moving indentor [46]

According to Conway Jr. and Kirchner [46], the median crack size in the plane of motion (*x*-*z* plane) under a moving indentor is given as:

$$c_M = \left(\frac{0.02PQ}{K_c Z_0} \right)^2 \tag{7.6}$$

where

$$Z_0 = kP^{1/2} \tag{7.7}$$

Here, Q represents the increase of out of plane hoop stress for a corresponding tangential-normal load ratio. A simple relationship between the load ratio and Q is given in Table 7.2.

Table 7.2 Relationship between load ratio and Q

Load ratio (P'/P)	0	1	2
Q	1.00	1.40	2.25

7.1.2 Brittle-Ductile Mixed Material Removal Mechanism

Due to the random distribution of grinding grits on the wheel surface, grits will have different engagement depth in the grinding process. In order to address the stochastic nature of the grinding process, the undeformed chip thickness distribution should be described based on the analysis in section 3.3. A description of undeformed chip thickness spectrum is necessary since the transition from brittle to ductile material-removal is directly related to the scale of the machining process. A critical-depth-of-cut model relating material properties and the ductile regime limit was established [40]. This critical-depth-of-cut is used as a measure of the brittle-ductile transitioning point. An expression for the critical depth of cut d_c corresponding to the threshold load per grain for fracture, was derived as:

$$d_c = \beta(\frac{E}{H})(\frac{K_c}{H})^2 \tag{7.8}$$

where β is a constant, E is elastic modulus of workpiece, H is hardness of workpiece and K_c is fracture toughness of workpiece. Experimental results with different ceramic materials followed (7.8) fairly well with $\beta = 0.15$, assuming that the depth of cut is

equal to the machine infeed. The material is assumed to be removed in brittle fracture for undeformed chip thickness greater than the critical undeformed chip thickness and otherwise in ductile flow.

To support the brittle-ductile combined modeling of surface finish proposed in this paper, another study by Chen, et al. [86] is investigated here. It is observed that with an increasing wheel speed (which represents a decreasing average undeformed chip thickness), the ground surface morphology changes from a mixture of brittle-ductile tracks to mostly ductile tracks as shown in Figure 7.3. It suggests that at different undeformed chip thickness, the surface generation mechanism will be different. Therefore, a purely ductile mode material removal assumption of the previous surface roughness models is not valid. In order to accurately model the surface roughness under different process conditions and different materials, it is necessary to consider the brittle-ductile combined effect in modeling effort.

V_s = 30 m/s V_s = 90 m/s V_s = 150 m/s

Figure 7.3 Micrographs of ground surface of Si_3N_4 at different wheel speeds (a_e = 40μm, v_w = 3m/min)

As shown in the experimental results, the higher undeformed chip thickness would result in more brittle fracture mode of material removal. The large surface fracture

percentage generally corresponds to rougher surface finish and more surface damage to the workpiece. By evaluating the crack size and the percentage of fractured surface, the physics-based surface roughness model is more accurate than the model without consideration of ductile-brittle combined material removal mechanism. The median crack size distribution could be estimated in a similar manner to estimate the strength degradation of the mechanical component.

7.2 Surface Roughness in Ceramic Grinding

Surface finish plays an important role in determining the performance of a ceramic component since it is closely related to crack nucleation and propagation, corrosion and wear. From analytical point of view, each protruding abrasive grit on a grinding wheel generates an intense local stress field upon contacting the workpiece surface. This stress field causes irreversible material deformation in the form of dislocations, cracks and voids [87]. The irreversible material-removal mechanisms can be divided into two types: brittle and ductile. In brittle mechanisms, material removal is accomplished through the crack propagation and intersection, while ductile mechanisms produce plastic flow of material in the form of severely sheared machining chips [40].

Regarding the surface generated in ceramic grinding, the grooves produced by ductile material removal can be characterized by clearly ploughed cutting paths generated by the grit. The grooves created by brittle fracture can be characterized by the lateral crack size c_L as well as the plastic zone depth h.

Since a complete description of the surface is very difficult due to the randomness of grit-workpiece interaction, the following assumptions have to be established in order

to simplify the calculation: (1) Grooves generated by ductile material removal is characterized by the undeformed chip thickness of individual grits; grooves generated by brittle material removal is characterized by the lateral crack system, the shape of the cracked groove is assumed to be a triangular of depth h and length $2c_L$. (2) There is no groove overlapping. (3) The groove of ductile material removal has a triangular shape that comes from the projection of the assumed conical shape for the active grit. (4) The surface roughness is estimated perpendicular to the grinding direction. Under these assumptions, the cross-section profile generated by different grits is shown in Figure 7.4.

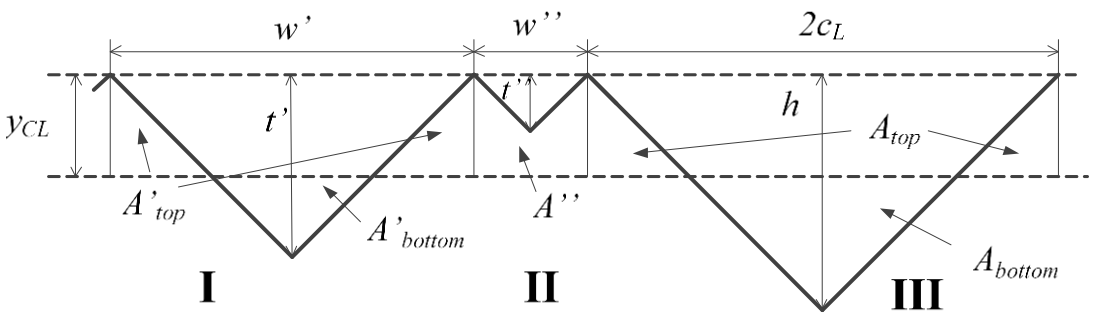

Figure 7.4 Theoretical surface profile generated by ductile and brittle grooves

In section I, the undeformed chip thickness is larger than the center line of the surface profile but smaller than the critical undeformed chip thickness; in section II, the undeformed chip thickness is smaller than the center line; in section III, the undeformed chip thickness is larger the critical undeformed chip thickness, thus brittle mode material removal will take place.

The surface roughness can be generally describe by the arithmetic mean value, R_a, defined as:

$$R_a = \frac{1}{L}\int_0^L |y - y_{CL}|\, dl \tag{7.9}$$

where y_{CL} is the position of the center-line so that the areas above and below the line are equal. By definition:

$$p'E(A'_{top}) + p''E(A'') + pE(A_{top}) = p'E(A'_{bottom}) + pE(A_{bottom}) \tag{7.10}$$

where p' and p'' are the probabilities of a groove depth to be less and greater than y_{CL} but smaller than critical undeformed chip thickness t_{cr}, and p is the probability of a grit engagement depth greater than critical undeformed chip thickness. These probabilities can be mathematically defined as:

$$p' = \int_{y_{CL}}^{t_{cr}} f(t)dt \tag{7.11}$$

$$p'' = \int_0^{y_{CL}} f(t)dt \tag{7.12}$$

$$p = \int_{t_{cr}}^{\infty} f(t)dt \tag{7.13}$$

The area above and below the center line in section I can be calculated as:

$$E(A'_{top}) = \tan\psi\, y_{CL}^2 \tag{7.14}$$

$$E(A'_{bottom}) = \tan\psi\left[E(t'^2) - 2y_{CL}E(t') + y_{CL}^2\right] \tag{7.15}$$

where t' represents groove with a depth larger than y_{CL} but less than t_{cr}.

The area above the center line in section II can be calculated as:

$$E(A'') = \tan\psi\left[2y_{CL}E(t'') - E(t''^2)\right] \tag{7.16}$$

where t'' represents groove with a depth less than y_{CL}.

The area above and below the center line in section III can be calculated as:

$$E(A_{top}) = y_{CL}^2 E(\frac{c}{h}) \tag{7.17}$$

and

$$E(A_{bottom}) = E(hc) - 2E(c)y_{CL} - y_{CL}^2 E(\frac{c}{h}) \tag{7.18}$$

After substitute equations (7.1), (7.4) to equations (7.17), (7.18) and then substitute equations (7.11) to (7.18) into equation (7.10), the center line position can be calculated numerically.

By definition, the surface roughness can be calculated by dividing the area between the profile and the centerline by total length. Therefore, the expected value of the surface roughness contribution of section I, section II and section III can be calculated by:

$$E(R'_a) = E\left(\frac{A'_{top} + A'_{bottom}}{2t' \tan\psi}\right) \tag{7.19}$$

$$E(R''_a) = E\left(\frac{A''}{2t'' \tan\psi}\right) \tag{7.20}$$

and

$$E(R_{a\_brittle}) = E\left(\frac{A_{top} + A_{bottom}}{2c}\right) \tag{7.21}$$

After calculation of the expectation of top and bottom areas as well as the groove length in all three sections, the surface roughness can be evaluated as a weighted contribution as in (7.22).

$$E(R_a) = p'E(R'_a) + p''E(R''_a) + pE(R_{a\_brittle}) \tag{7.22}$$

After substituting equations (7.11) to (7.13), (7.19) to (7.21) into equation (7.22), the surface roughness of brittle-ductile grinding of ceramics can be calculated numerically.

7.3 Strength Degradation in Ceramic Grinding

The brittle material removal not only generate a rougher surface, but also tends to introduce median cracks that will degrade the mechanical strength of the component. In this section, an approach is proposed to calculate the strength degradation based on the median crack development.

Based on [46], the depth of damage is seen to increase with a corresponding increase in horizontal load. For the plane perpendicular to the plane of motion of the tool, the tangential load does not affect the crack size (Q = 1). This indicates that the penny cracks will propagate to greater lengths in the plane of motion of the tool and results in more degradation in this direction. Thus, if the bending test is carried perpendicular to the grinding direction, the component would fail at a lower stress.

However, these has not been a reliable model to predict the tangential grinding force in brittle mode grinding. The tangential/normal load ratio is calibrated from experiment.

Assuming that the median crack size is the main factor influencing the fracture strength, according to fracture mechanics, the fracture strength of a component is determined by:

$$\sigma_F = \frac{K_c}{Yc_M^{1/2}} \tag{7.23}$$

where Y is the geometry factor. Experimental measurements [88] of grinding induced strength degradation follows an edge-notch crack geometry with $Y = 1.99$.

Since grinding is a random process, there will be a distribution of crack size due to the different engagement depth between the grit and the workpiece according to (7.6) and (7.7). The probability distribution of the crack size is directly calculated from the distribution of single grit load which is calculated from undeformed chip thickness based on (7.5).

This will also result in a probability distribution of remaining strength of the specific component according to (7.23). In realistic grinding situation, researchers have found a statistical distribution of the strength of brittle material as well. The tensile strength of a brittle material under uniform loading is found to follow the Weibull distribution [89], with probability of failure at stress σ given by:

$$P_f = 1 - \exp\left\{-V\left(\frac{\sigma - \sigma_u}{\sigma_0}\right)^m\right\} \tag{7.24}$$

where m is a parameter known as the Weibull modulus, V is the volume of the material, σ_0 is the characteristic strength of the component which corresponds to 63.2% fracture possibility, and σ_u is the stress below which there is zero probability of failure. The characteristic strength and fitted Weibull modulus can be used to validate the model.

7.4 Model Validation

7.4.1 Surface Roughness Experimental Results

7.4.1.1 Grinding Experiment of Silicon Carbide

The predictions of surface roughness using proposed mode is first compared to the non-physics-based model with existing experimental data in the literature (Agarwal and Rao, 2010). The experiments were conducted on a surface grinding machine with diamond grinding wheel (ASD240R100B2) and SiC workpiece. The wheel diameter is 250 mm and wheel speed is hold constant as 36.6m/s. Twenty-five sets of surface roughness measurements were obtained with different the depth of cut and workpiece feed rate. The experiment kinematic parameters and results are given in Table 7.3. Physics-based predictions proposed by this paper and non-physics-based predictions proposed by Rao (2005) were compared to the experimental results. Sets 1, 6, 11, 16, 21 were used for calibration. The parameter k in (7.4) is calibrated to be around 0.075 for SiC. The results are shown in Figure 7.6. The mean error for physics-based model is estimated to be 5.65% while the mean error for non-physics-based model is 9.00%. The composition of ductile and brittle generated surface profile is summarized in Figure 7.5. It can be seen that the brittle fracture generated surface plays an more important role when the undeformed chip thickness is larger.

Table 7.3 Experiment results and kinematic parameters in surface grinding of SiC

Exp. No.	a_e (μm)	v_s / v_w	R_a (μm)
1	5	440	0.164
2	5	293	0.229
3	5	220	0.271
4	5	176	0.311
5	5	146	0.329
6	15	440	0.206
7	15	293	0.244
8	15	220	0.297
9	15	176	0.339

Table 7.3 continued

10	15	146	0.367
11	25	440	0.213
12	25	293	0.271
13	25	220	0.331
14	25	176	0.369
15	25	146	0.4
16	35	440	0.253
17	35	293	0.324
18	35	220	0.351
19	35	176	0.394
20	35	146	0.426
21	45	440	0.312
22	45	293	0.353
23	45	220	0.396
24	45	176	0.432
25	45	146	0.493

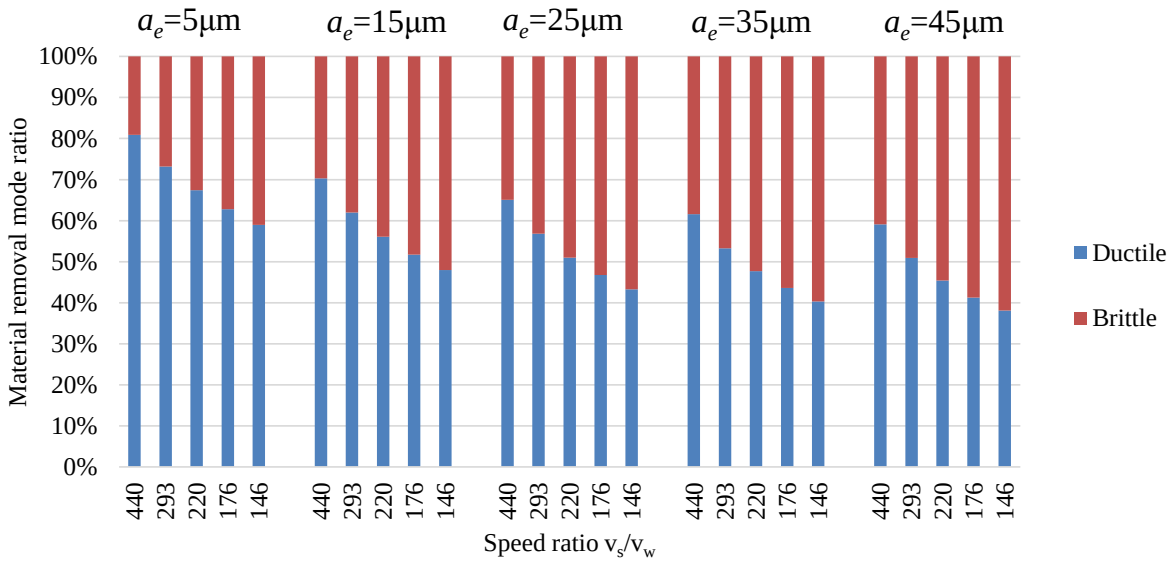

Figure 7.5 Composition of ductile and brittle surface

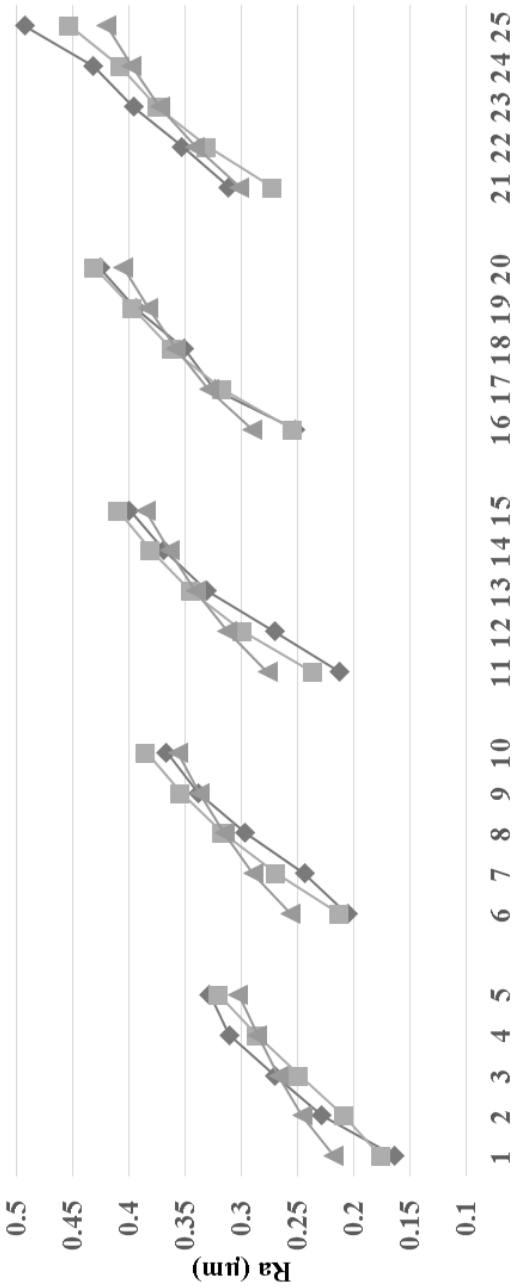

Figure 7.6 Comparison of predictions and experimental results in surface grinding of SiC

Besides validation from surface grinding experiment in literature, a series of experiments were performed on a cylindrical grinding machine to assess the validity of the model. In this experiment, a ceramic bonded diamond wheel with grit number 170 and diameter of 400mm was used. The workpiece was a SiC rod with 100 mm diameter.

The main kinematic parameters for each experiment are depth of cut, workpiece speed and wheel speed. The process parameters along with the measurement of surface roughness are shown in Table 7.4. The sets 1 and 5 were used for calibration. The results are shown in Figure 7.7. Set 1 and 5 was used for calibration. The mean error for physics-based model is estimated to be 13.37% while the mean error for non-physics-based model is 25.25%. To better understand the brittle-ductile combined material removal of ceramic grinding, the possibility and the expected value of surface roughness components in all three sections are listed in Table 7.5.

Table 7.4 Experiment results and kinematic parameters in cylindrical grinding of SiC

Exp. No.	a_e (μm)	v_s (m/s)	v_w (m/s)	R_a (μm)	Lubrication
1	13	80	0.08	0.148	Wet
2	13	60	0.08	0.165	Wet
3	13	40	0.08	0.191	Wet
4	13	20	0.08	0.331	Wet
5	3.8	80	0.267	0.276	Dry
6	5	60	0.2	0.295	Dry
7	7.5	40	0.133	0.308	Dry
8	15	20	0.067	0.335	Dry

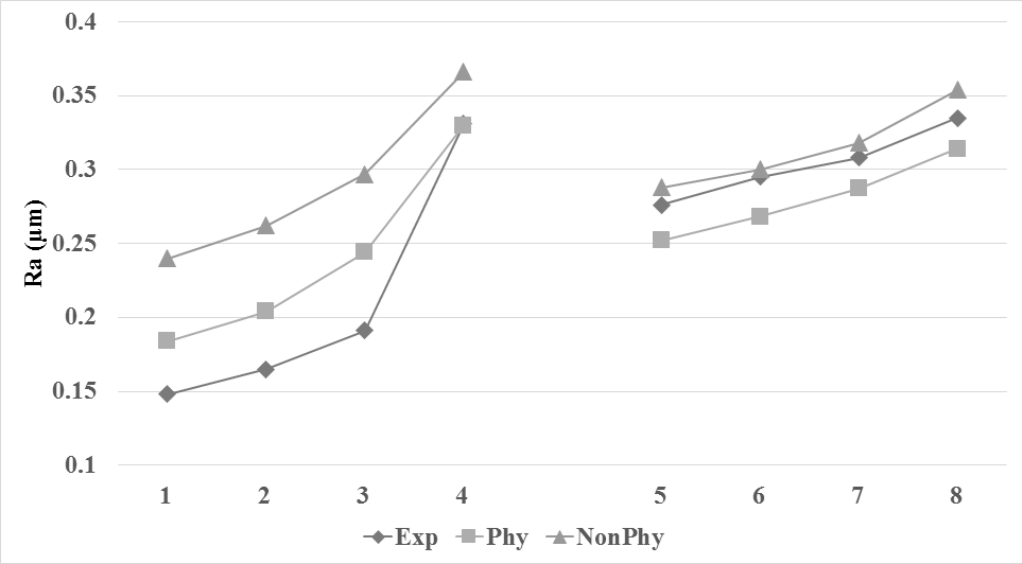

Figure 7.7 Comparison of predictions and experimental results in cylindrical grinding of SiC

Table 7.5 Surface roughness components in cylindrical grinding test of SiC

Exp. No.	$E(R_a)$ (μm)	p'	$E(R'_a)$ (μm)	p''	$E(R''_a)$ (μm)	p	$E(R_{a\_brittle})$ (μm)
1	0.184	56.44%	0.160	20.02%	0.200	23.46%	0.226
2	0.204	49.97%	0.167	20.36%	0.221	29.59%	0.255
3	0.244	41.49%	0.177	19.85%	0.247	38.58%	0.314
4	0.338	19.99%	0.250	26.45%	0.362	53.49%	0.344
5	0.252	43.41%	0.175	20.22%	0.242	36.29%	0.350
6	0.268	43.22%	0.172	17.38%	0.231	39.32%	0.392
7	0.287	37.37%	0.182	18.80%	0.257	43.74%	0.390
8	0.314	24.63%	0.226	23.98%	0.330	51.32%	0.350

In both comparisons the new model integrated with brittle-ductile transition has less error in the predictions. It has been noticed that while comparing the results under same depth of cut condition (for example, set 1-5 in surface grinding experiment), the physics-based model correctly captured the trend of surface roughness vs. speed ratio

while non-physics-based model failed. This is because the non-physics-based models as proposed by previous works (Agarwal and Rao, 2005; Agarwal and Rao, 2010) achieved a simple linear relationship between the surface roughness and the expectation of undeformed chip thickness based on purely ductile grooves assumption. However, in reality with the decrease of wheel speed/increase of workpiece speed, the material removal mechanism will transfer from more ductile to more brittle and thus the change in the surface generation mechanism cannot be reflected by the purely plastic flow hypothesis.

7.4.1.2 Grinding Experiment of Silicon Nitride

In order to further validate the model predictions, surface roughens data from grinding experiment of silicon nitride material in literature (Huang et al., 2003) are compared to the model predictions. Surface grinding experiments were performed on an Okamoto high speed grinder. The grinding wheel diameter is 200 mm, grinding width is 6 mm and wheel speed is 40 m/s. The average grain size used is 160μm. The grinding experiment were employed in a down grinding mode under different wheel engagement depth and different workpiece speed. The surface roughness of ground samples was measured using a profilometer perpendicular to the grinding direction. The predictions of physics-based and non-physics-based models are compared to the measurements in Figure 7.8(a) and Figure 7.8(b). The mean error for physics-based model is estimated to be 18.9% while the mean error for non-physics-based model is 35.6%. The results also show that the physics-based model is able to capture the trend of surface roughness with increasing depth of cut or workpiece speed while the linear non-physics model failed to.

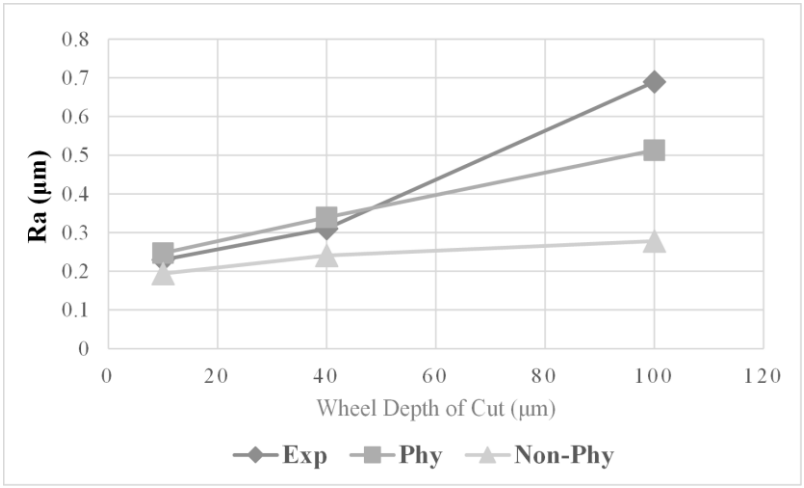

(a)

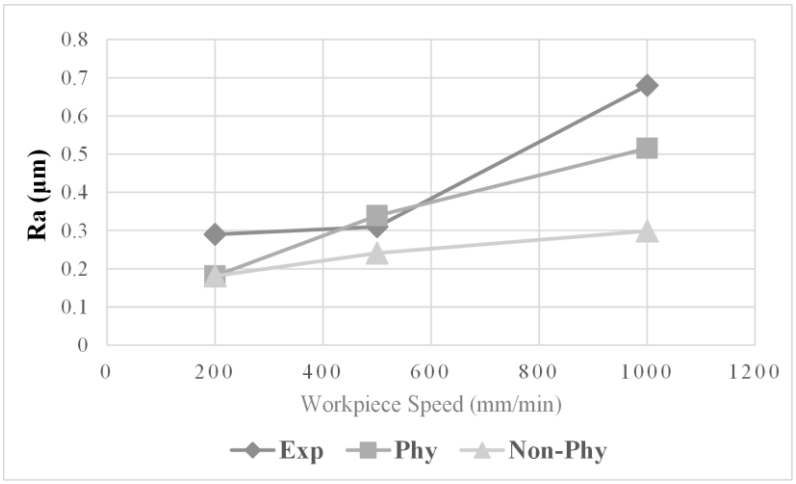

(b)

Figure 7.8 Comparison of predictions and experimental results in surface grinding of Si3N4 (a) varying depth of cut, (b) varying workpiece speed

7.4.2 Strength Degradation Experimental Results

In order to validate the strength degradation due to grinding process, the experimental data from Hwang, et al. [90] has been used. The grinding wheel of diameter 203 mm and width 25.4 mm containing a single layer of 180 grit diamond abrasive grains

in an electroplated nickel bond was used. The workpiece was slipcast sintered silicon nitride with a fracture toughness K_c = 8.0 MPam$^{1/2}$ and hardness H = 16 GPa. The flexure strength were conducted to investigate the effect of wheel speed and grinding direction. The specimens were ground in longitudinal and transverse direction with a = 25.4 μm and V_w = 63.5 mm/s. The wheel speed conditions tested was V_s = 85 m/s and 149 m/s. Here, the wheel speed of 85 m/s was used to calibrate the parameter Q as well as k in (7.6) and (7.7). The comparison is shown in Figure 7.9. It can be seen from the prediction and the experimental results that the wheel speed does not significantly influence the flexure strength in this case but the grinding direction significant affects the flexure strength. The model prediction is close to the experimental results with an average error of 4.3%.

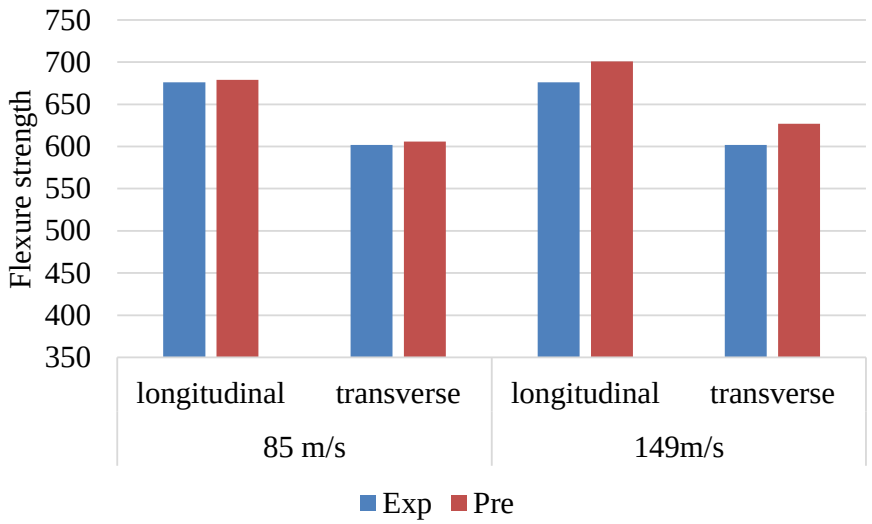

Figure 7.9 Comparison of predictions and experimental results of flexure strength after grinding of silicon nitride bar

7.5 Summary

This chapter describes the modeling technique for some of the most important surface characteristics in grinding of ceramic materials that includes surface roughness and the strength degradation due to surface cracks.

Section 7.1 reviews the previous studies on crack propagation and material removal mechanism in ceramic grinding which serve as a theoretical foundation for our predictive models.

In section 7.2, a probabilistic model of surface roughness in ceramic grinding is proposed. The surface generation due to ductile and brittle material removal is combined with grinding kinematics model for accurate prediction of the surface roughness.

In section 7.3, the strength degradation due to median crack propagation is discussed. A predictive model describing the tensile strength of a ceramic component due to grinding imparted surface cracks is proposed.

Section 7.4 presents the validation result for the predictive models. Surface roughness is validated at various experimental conditions with different ceramic materials including silicon carbide and silicon nitride. The strength degradation is validated at different wheel speed and grinding direction.

CHAPTER 8

CONCLUSIONS

8.1 Summary

This dissertation presents a method of predicting residual stresses in MQL grinding processes and surface roughness in grinding of ceramics. The residual stress modeling techniques were derived from previously developed modeling techniques for grinding processes under different lubrication conditions. In CHAPTER 3, the general model of grinding force was presented. The lubrication effect of MQL was investigated based on boundary lubrication theory. The modeling approach includes single grit interaction analysis as well as distribution of undeformed chip thickness. CHAPTER 4 presented the grinding temperature modeling. The modeling approach was based on moving heat source model and heat partition analysis. The cooling effect of MQL was estimated by using two-phase homogeneous flow and the parallel plate heat transfer model. The coupling effect of grinding force and temperature modeling was addressed using Johnson-Cook constitutive model to predict the flow stress at different temperature.

In CHAPTER 5, the residual stress modeling approach was proposed. The mechanical loading and thermal loading stresses have been considered in this study. The stress history in grinding process have been discussed due to the discrepancy of strain rate, moving speed, and loading passes of mechanical and thermal stress field. The McDowell hybrid model have been utilized in this study to calculate the residuals stress generation based on stress history analysis.

CHAPTER 6 compared the model predictions to experimental data for grinding process under dry, MQL and flood cooling conditions. The experiment set-up and equipment was first introduced. Followed by the characterization of wheel surface properties and boundary lubrication parameters. Different workpiece materials, process parameters and lubrication conditions have been pursued in the experimental validations. Grinding force and workpiece temperature predictions were presented based on different measurement techniques. Good agreement have been achieved between the predictions and experimental measurements. The residual stress model was compared to experimental data for a range of different conditions with AISI 1018 and AISI 1045 steel. The results showed good agreement with the magnitude and residual stress trends. The model have also been used for successfully predicted the onset temperature for tensile residual stress of AISI 52100 steel.

In CHAPTER 7, the surface characteristics in ceramic grinding have been investigated. Important parameters including surface fracture percentage, crack size, and surface roughness have been analyzed. A ductile-brittle mixed surface generation mechanism was employed for the estimation of surface fracture and surface roughness. The predictions were compared with published experimental data. The surface roughens of silicon carbide and silicon nitride materials under different grinding conditions have been used for experimental validation. Generally, the physics-based model achieves more precise prediction than conventional undeformed chip thickness models, especially at large undeformed chip thickness where the brittle fracture could be the major surface generation mechanism.

8.2 Conclusions

The research presented in this dissertation was driven by the need for an analytical model for predictive modeling of grinding process. The research has shown that it is possible to model grinding induced residual stresses and other surface characteristics in an analytical fashion. The impact of cutting forces and thermal effects coupled with knowledge of the material behavior under the influence of those parameters can be coupled with an incremental plasticity model to predict residual stresses in MQL grinding. The ductile-brittle mixed material removal mechanism and indentation fracture mechanics analysis of the crack system have been utilized in the modeling of surface characteristics in ceramic grinding. The modeling techniques presented are well suited for quick and trend-accurate analysis of grinding process output parameters such as cutting forces, workpiece temperatures, residual stresses and other surface characteristics. The predictive models have shown generally good agreement with the experimental results.

MQL effectively reduces the friction coefficient and thus lowers the grinding forces and the efficient chip removal reduces the tendency of wheel loading. The grinding temperature in MQL is also noticeably lower due to the decrease of total grinding energy input as well as the cooling effect of MQL. As for residual stress generation, due to the lower temperature rise, the residual stress is more compressive than dry condition and comparable to flood cooling condition in some cases. In general, the MQL could significantly improve the grinding performance comparing to complete elimination of lubricant. However, due to the nature of high energy input and temperature rise in grinding process, the MQL process is currently limited to the application with low material removal rate. The performance could be greatly improved by enhancing the

cooling effect using grinding wheels with higher thermal conductivity or external cooling sources.

In ceramic grinding, the surface roughness and surface degradation are directly related to process conditions, grit type as well as material properties. With an increase of undeformed chip thickness, rougher surface, larger crack sizes and lower component strength are expected. A smaller undeformed chip thickness or smaller single grit load could promote the ductile material removal of the material which results in a smoother surface and less damage. It is shown by the experiment as well as the predictive model that by tuning the process conditions and wheel characteristics, a better surface quality could be achieved with same material removal rate.

8.3 Contributions

The modeling techniques presented in this dissertation provided improvements to the current state of the art in analytical residual stress prediction in MQL grinding and physics-based prediction of surface characteristics in ceramic grinding. The intellectual contributions of the research presented are as follows:

- Developed an analytical predictive residual stress model for MQL grinding process based on lubrication characteristics, cutting forces, thermal effects, and flow behavior of the material
- Stress history analysis for mechanical and thermal loadings
- Validated the model for grinding process under various process and lubrication conditions based on experimental measurements and published data

- Incorporated the effects of MQL in terms of lubrication and cooling
- Physics-based modeling of surface fracture, crack size and surface roughness in grinding of ceramic materials
- Validated the model with published experimental data of silicon carbide and silicon nitride

8.4 Future Work

The current model provides a solid foundation for predicting grinding forces, temperature and residual stresses produced from the grinding process. It offers a quick and effective method of modeling those process output parameters. However, there are opportunities for improving the predictive capability of the model. The following areas for future research will help to address limitations in the current modeling capabilities and improve the state of residual stress modeling.

Due to the complexity of grinding process, a number of factors including the wheel dressing conditions, wheel wear, wheel type, chip removal, and MQL lubrication parameters (flow rate, air pressure, nozzle position, and type of fluid) were not fully addressed in this work. The variations in grinding output parameters due to these effects may impact the residual stress generation.

Although the model presented performs well in terms of capturing trends and magnitudes of residual stresses produced from a variety of grinding conditions, there are still areas for improvement. The effect of phase transformation is apparent at high temperature cases. The current modeling approach does not account for that effect on the

residual stress formation. A method to incorporate phase transformation and its influence on the residual stress production needs to be developed.

In the present application, the friction coefficient was estimated based on the adsorbed lubricant film which was experimentally calibrated. An analytical model relating the lubricant film to the lubrication parameters would be necessary to quantify the influence of MQL parameters such as flow rate and air pressure. Also, the friction coefficient in dry grinding process was calibrated and was treated as a constant value. Perhaps a more analytical approach would serve the model better.

Measuring residual stresses is still a laborious task. Developing alternative techniques to measure sub-surface residual stresses such as the Barkhausen noise or ultrasonic sensing will ease the tremendous experimental efforts necessary to acquire residual stress data. Advancements in measuring capabilities may help to improve general modeling capabilities as well as guide process planning in production environments.

Regarding the surface characteristics modeling in ceramic grinding, the accuracy of the predictive models relies on the description of the crack systems in grinding process. Unlike indentation process, the interactions between different grits could affect the crack generation and propagation mechanism in grinding process. A more complete analysis should be conducted to investigate these effects.

The estimation of surface roughness is based on a number of assumptions such as triangular groove geometry, non-overlap grooves. The model accuracy could be greatly enhanced with a more accurate description of the surface profile. The strength degradation prediction requires more experimental validation efforts to justify the validity of the predictive model.

With the above enhancements to the current modeling, the techniques presented can progress towards becoming a more highly reliable, robust analytical model for predicting residual stresses in metal components and surface characteristics in ceramic components. The results will be realized as a useful tool in improving process optimization of grinding operations.

REFERENCES

[1] R. Autret and S. Liang, "Minimum quantity lubrication in finish hard turning," in *Proceedings of International Conference on Humanoid, Nanotechnology, Information Technology, Communication and Control, Environment, and Management*, 2003.

[2] S. Liang and J. Su, "Residal stress modeling in orthogonal machining," *CIRP Annals*, vol. 56, no. 1, pp. 65-68, 2007.

[3] S. Malkin, Grinding Technology: Theory and Applications of Machining with Abrasives, Ellis Howard Ltd. and Prentice Hall, 1989.

[4] S. Malkin and T. Huang, "Grinding mechanism for ceramics," *CIRP Annals*, vol. 45, no. 2, pp. 569-580, 1996.

[5] H. Park and S. Liang, "Force modeling of micro-grinding incorporating crystallographic effects," *International Journal of Machine Tools and Manufacture*, vol. 48, no. 15, pp. 1658-1667, 2008.

[6] R. Hecker, S. Liang, X. Wu, P. Xia and W. Guo, "Grinding force and power modeling based on chip thickness analysis," *International Journal of Advanced Manufacturing Technology*, vol. 33, no. 5-6, pp. 449-459, 2007.

[7] A. Filipovis and D. Stephenson, "Minimum quantity lubrication (MQL) applications in automotive power-train machining," *Machining science and Technology*, vol. 10, no. 1, pp. 3-22, 2006.

[8] B. Tai, D. Stephenson and A. Shih, "Workpiece temperature during deep-hole drilling of cast iron using high air pressure minimum quantity lubrication," *ASME Journal of Manufacturing Science and Engineering*, vol. 135, no. 3, 2013.

[9] S. Zhang, J. Li and Y. Wang, "Tool life and cutting forces in end milling Inconel 718 under dry and minimum quantity lubrication cutting conditions," *Journal of Cleaner Production*, vol. 32, pp. 81-87, 2012.

[10] Y. Liao and H. Lin, "Mechanism of minimum quantity lubrication in high-speed milling of hardened steel," *International Journal of Machine Tools and Manufacture*, vol. 47, no. 11, pp. 1660-1666, 2007.

[11] K. Li and S. Liang, "Modeling of cutting forces in near dry machining under tool wear effect," *International Journal of Machine Tools & Manufacture,* vol. 47, pp. 1292-1301, 2007.

[12] X. Ji, X. Zhang, B. Li and S. Liang, "Modeling of the effects of minimum quantity lubrication on machining force, temperature, and residual stress," *Machining Science and Technology,* vol. 18, no. 4, pp. 547-564, 2014.

[13] L. Silva, E. Bianchi, R. Fusse, R. Catai, T. Franca and P. Aguiar, "Analysis of surface integrity for minimum quantity lubricant - MQL grinding," *International Journal of Machine Tools & Manufacture,* vol. 47, pp. 412-418, 2007.

[14] C. Li, Y. Hou, S. Xiu and G. Cai, "Application of lubrication theory to near-dry green grinding - feasibility analysis," *Advanced Materials Research,* Vols. 44-46, pp. 135-142, 2008.

[15] B. Shen and A. Shih, "Minimum quantity lubrication (MQL) grinding using vitrified CBN wheels," in *Transactions of the North American Manufacturing Research Institution of SME, 37*, 2009.

[16] B. Shen, "Minimum Quantity Lubrication Grinding Using Nanofluids," Michigan, 2008.

[17] M. Sadeghi, M. Hadad, T. Tawakoli and M. Emami, "Minimal quantity lubrication - MQL in grinding of Ti-6Al-4V titanium alloy," *International Journal of Advanced Manufacturing Technology,* vol. 44, pp. 487-500, 2009.

[18] M. Sadeghi, M. Hadad, T. Tawakoli and M. Emami, "An investigation on surface grinding of AISI 4140 hardened steel using minimum quantity lubrication-MQL technique," *International Journal of Material Forming,* vol. 3, pp. 241-251, 2010.

[19] T. Tawakoli, M. Hadad, M. Sadeghi, A. Daneshi, S. Stockert and A. Rasifard, "An experimental investigation of the effects of workpiece and grinding parameters on minimum quantity lubrication - MQL grinding," *International Journal of Machine Tools and Manufacture,* vol. 49, no. 12-13, pp. 924-932, 2009.

[20] T. Tawakoli, M. Hadad and M. Sadeghi, "Influence of oil mist parameters on minimum quantity lubrication - MQL grinding process," *International Journal of Machine Tools & Manufacture,* vol. 50, no. 6, pp. 521-531, 2010.

[21] T. Tawakoli, M. Hadad and M. Sadeghi, "Investigation on minimum quantity lubricant-MQL grinding of 100Cr6 hardened steel using different abrasive and coolant-lubricant types," *International Journal of Machine Tools& Manufacture,* vol. 50, no. 8, pp. 698-708, 2010.

[22] M. Hadad and B. Sadeghi, "Thermal analysis of minimum quantity lubrication-MQL grinding process," *International Journal of Machine Tools & Manufacture,* vol. 63, pp. 1-15, 2012.

[23] M. Hadad, T. Tawakoli, M. Sadeghi and B. Sadeghi, "Temperature and energy partition in minimum quantity lubrication-MQL grinding process," *International Journal of Machine Tools & Manufacture,* Vols. 54-55, pp. 10-17, 2012.

[24] H. Dolle and J. Cohen, "Residual stresses in ground steels," *Metallurgical Transactions A,* vol. 11A, pp. 159-164, 1980.

[25] Y. Zhejun and H. Zhonghui, "Surface integrity of grinding of bearing steel GCr15 with CBN wheels," *CIRP Annals,* vol. 38, no. 1, pp. 677-688, 1989.

[26] B. Kruszynski and R. Wojcik, "Residual stress in grinding," *Journal of Materials Processing Technology,* vol. 109, pp. 254-257, 2001.

[27] M. Balart, A. Bouzina, L. Edwards and M. Fitzpatrick, "The onset of tensile residual stresses in grinding of hardened steels," *Materials Science and Engineering A,* vol. 367, pp. 132-142, 2004.

[28] X. Chen, W. Rowe and D. McCormack, "Analysis of the transitional temperature for tensile residual stress in grinding," *Journal of Materials Processing Technology,* vol. 107, pp. 216-221, 2000.

[29] A. Mishra and T. Prasad, "Residual stresses due to a moving heat source," *International Journal of Mechanical Sciences,* vol. 27, no. 9, pp. 571-581, 1985.

[30] M. Mahdi and L. Zhang, "Applied mechanics in grinding. Part 7: residual stresses induced by the full coupling of mechanical deformation, thermal deformation and phase transformation," *International Journal of Machine Tools & Manufacture,* vol. 39, p. 1285–1298, 1999.

[31] P. Moulik, T. Yang and S. Chandrasekar, "Simulation of thermal stresses due to grinding," *International Journal of Mechanical sciences,* vol. 43, pp. 831-851, 2001.

[32] H. Hamdi, H. Zahouani and Bergheau, "Residual stress computation in a gridning process," *Journal of Materials Processing technology,* vol. 147, pp. 277-285, 2004.

[33] Y. Matsumoto, M. Barash and C. Liu, "Effect of hardness on the surface integrity of AISI 4340 steel," *Journla of Engineering for Industry,* vol. 108, no. 3, pp. 169-175, 1986.

[34] D. Wu and Y. Matsumoto, "Effect of hardness on residual stresses in orthogonal machining of AISI 4340 steel," *Journal of Engineering for Industry,* vol. 112, no. 3,

pp. 245-252, 1990.

[35] J. Su, K. Young, K. Ma, S. Srivatsa, J. Morehouse and S. Liang, "Modeling of residual stresses in milling," *International Journal of Advanced Manufacturing Technology,* vol. 65, pp. 717-733, 2013.

[36] H. Tonshoff, J. Peters, I. Inasaki and T. Paul, "Modeling and simulation of grinding processes," *CIRP Annals,* vol. 41, no. 2, pp. 677-688, 1992.

[37] S. Malkin and J. Ritter, "Grinding mechanisms and strength degradation for ceramics," *Journal of Engineering for Industry,* vol. 111, pp. 167-174, 1989.

[38] A. Imanaka, A. Fujino and S. Maneta, "Direct observation of material removal process during grinding of ceramics by micro-flash technique," in *Proceedings of the Symposium on the Science of Ceramic Machining and Surface Finishing*, Gaitherabug, 1970.

[39] B. Zhang, H. Tokura and M. Yoshikawa, "Study on surface cracking of alumina scratched by single-point diamonds," *Journal of Materials Science,* vol. 23, pp. 3214-3224, 1988.

[40] T. Bifano, T. Dow and R. Scattergood, "Ducile-regime grinding: a new technology for machining brittle materials," *Journal of Engineering for Industry,* vol. 113, no. 2, pp. 184-189, 1991.

[41] C. Chen, Y. Jung and I. Inasaki, "Surface, cylindrical and internal grinding of advanced ceramics," in *Grinding Fundamentals and Applications,* 1989, pp. 201-211.

[42] K. Li and T. Liao, "Surface/subsurface damage and the fracture strength of ground ceramics," *Journal of Materials Processing Technology,* vol. 57, pp. 207-220, 1996.

[43] T. Maksoud, A. Mokbel and J. Morgan, "Evaluation of surface and sub-surface cracks of ground ceramic," *Journal of Materials Processing Technology,* vol. 88, pp. 222-243, 1999.

[44] R. Lawn and A. Evans, "Elastic/plastic indentation damage in ceramics: the median/radial crack system," *Journal of the American Ceramic Sociecty,* vol. 63, no. 9-10, pp. 574-581, 1980.

[45] D. Marshall, B. Lawn and A. Evans, "Elastic/plastic indentation damage in ceramics: the lateral crack system," *Journal of the American Ceramic Society,* vol. 65, no. 11, pp. 561-566, 1982.

[46] J. Conway Jr. and H. Kirchner, "The mechanics of crack initiation and propagation beneath a moving sharp indentor," *Journal of Materials Science,* vol. 15, pp. 2879-2883, 1980.

[47] A. Evan and D. Marshall, "Wear Mechanisms in Ceramics," in *Fundamentals of Friction and Wear of Materials*, ASME, 1981, p. 439.

[48] J. Conway Jr. and H. Kirchner, "Crack branching as a mechanism of crushing during grinding," *Journal of the American Ceramic Society,* vol. 69, pp. 603-607, 1986.

[49] R. Hecker, "Part surface roughness modeling and process optimal control of cylindrical grinding," Atlanta, 2002.

[50] S. Kato, E. Marui and M. Hashimoto, "Fundamental study on normal load dependency of friction characteristics in boundary lubrication," *Tribology Transactions,* vol. 41, no. 3, pp. 341-349, 1998.

[51] V. A. Godlevski, A. V. Volkov, V. N. Latyshev and L. N. Maurin, "The kinetivs of lubricant penetration action during machining," *Lubrication Science,* vol. 9, no. 2, pp. 127-140, 1997.

[52] X. Ji, "Predictive modeling of residual stress in minimum quantity lubrication machining," Shanghai, 2014.

[53] H. Sin, N. Saka and N. P. Suh, "Abrasive wear mechanisms and the grit size effect," *Wear,* vol. 55, no. 1, pp. 163-190, 1979.

[54] B. Bhushan, Tribology and Mechanics of Magnetic Storage Devices, New York: Springer-Verlag, 1999.

[55] S. Son, H. Lim and J. Ahn, "Effects of the friction coefficient on the mininum cutting thickness in micro cutting," *International Journal of Machine Tools and Manufacture,* vol. 45, no. 4-5, pp. 529-535, 2005.

[56] N. Ikawa, S. Shimada, H. Tanaka and G. Ohmori, "Atomistic analysis of nanometric chip removal as affected by tool-work interaction in diamond turning," *CIRP Annals,* vol. 40, no. 1, p. 5519554, 1991.

[57] P. Basauray, B. Misra and G. Lal, "Transition from ploughing to cutting during machining with blunt tools," *Wear,* vol. 43, no. 3, pp. 341-349, 1977.

[58] J. Manjunathaiah and W. Endres, "A new model and analysis of orthogonal machining with an edge-radiused tool," *Transactions of the ASME,* vol. 122, pp. 384-390, 2000.

[59] M. Shaw, Principles of Abrasive Processing, Oxford Unviersity Press, 1996.

[60] L. Li and J. Fu, "A study of grinding force mathematical model," *CIRP Annals,* vol. 29, pp. 245-259, 1980.

[61] S. Malkin and N. Cook, "The wear of grinding wheels, part 1, attritious wear," *Journal of Manufacturing Science and Engineering,* vol. 93, no. 4, pp. 1120-1128, 1971.

[62] J. Tang, J. Du and Y. Chen, "Modeling and experimental study of grinding forces in surface grinding," *Journal of Materials Processing Technology,* vol. 209, pp. 2847-2854, 2009.

[63] U. Durgumahanti, V. Singh and P. Rao, "A new model for grinding force prediction and analysis," *International Journal of Machine Tools & Manufacture,* vol. 50, pp. 231-240, 2010.

[64] S. Kannappan and S. Malkin, "Effect of grain size and operating parameters on the mechanics of grinding," *Journal of Manufacturing Science and Engineering,* vol. 94, no. 3, pp. 833-842, 1972.

[65] M. Younis and H. Alawi, "Probabilistic analysis of the surface grinding process," *Transaction of the CSME,* vol. 8, no. 4, pp. 208-213, 1984.

[66] W. Rowe, M. Morgan, H. Qi and H. Zheng, "The effect of deformation on the contact area in grinding," *CIRP Annals,* vol. 42, no. 1, pp. 409-412, 1993.

[67] R. Hecker, I. Ramoneda and S. Liang, "Analysis of wheel topography and grit force for grinding process modeling," *Journal of Manufacturing Processes,* vol. 5, no. 1, pp. 13-23, 2003.

[68] J. Jaeger, "Moving sources of heat and the temperature at sliding contacts," *Journal of the Royal Soceity of New South Wales,* vol. 84, no. 21, pp. 4316-4318, 1942.

[69] W. Rowe, "Temperature case studies in grinding including an inclined heat source model," *Proceedings of the Institution of Mechanical Engineers, Part B: Journal of Engineering Manufacture,* vol. 215, no. 4, pp. 473-491, 2001.

[70] W. Rowe, "Thermal analysis of high efficiency deep grinding," *International Journal of Machine Tools & Manufacture,* vol. 41, pp. 1-19, 2001.

[71] R. Hahn, "On the nature of the grinding process," in *Proceedings of the 3rd MTDR Conference,* 1962.

[72] N. Kim, C. Guo and S. Malkin, "Heat flux distribution and energy partition in creep-feed grinding," *CIRP Annals*, vol. 46, no. 1, pp. 227-232, 1997.

[73] T. Bergman, A. Lavine, F. Incropera and D. Dewitt, Fundamentals of Heat and Mass Transfer, 7th ed., John Wiley & Sons, Inc., 2011.

[74] K. Johnson, Contact Mechanics, Cambridge: Cambridge Univeristy Press, 1985.

[75] S. Timoshenko and J. Goodier, Theory of Elasticity, International Ed., McGraw-Hill, 1970.

[76] D. McDowell, "Approximate algorithm for elastic-plastic two-dimentional rolling/sliding contact," *Wear*, vol. 211, no. 2, pp. 237-246, 1997.

[77] O. Fergani, Y. Shao, I. Lazoglu and S. Liang, "Temperature effects on grinding residual stress," *Procedia CIRP*, vol. 14, pp. 2-6, 2014.

[78] M. Saif, C. Hui and A. Zehnder, "Interface shear stresses induced by non-uniform heating of a film on a substrate," *Thin Solid Films*, vol. 224, pp. 159-167, 1993.

[79] J. Merwin and K. Johnson, "An analysis of plastic deformation in rolling contact," *Proceedings, Institution of Mechanical Engineers*, vol. 177, no. 25, pp. 676-685, 1963.

[80] G. List, G. Stter and A. Bouthiche, "Cutting temperature prediction in high speed machining by numerical modelling of chip formation and its dependence with crater wear," *International Journal of Machine Tools & Manufacture*, Vols. 54-55, pp. 1-9, 2012.

[81] S. Jaspers and J. Dautzenberg, "Material behaviour in conditions similar to metal cutting: flow stresses in the primary shear zone," *Journal of Materials Processing Technology*, vol. 122, no. 2-3, pp. 322-330, 2002.

[82] L. Yan, Y. Rong, F. Jiang and Z. Zhou, "Three-dimension surface characterization of grinding wheel using white light interferometer," *International Journal of Advanced Manufacturing Technology*, vol. 55, pp. 133-141, 2011.

[83] Y. Shao, B. Li, K. Zhang and S. Liang, "Physics-based analysis of minimum quantity lubrication grinding," *International Journal of Advanced Manufacturing Technology*, 2015.

[84] Y. Huang and S. Liang, "Force modeling in shallow cuts with large negative rake angle and large nose radius tools-application to hard turning," *International Journal of Advance manufacturing Technology*, vol. 22, pp. 626-632, 2003.

[85] S. Jahanmir, H. Xu and L. Ives, "Mechanisms of material removal in abrasive machining of ceramics," in *Machining of Ceramics and Composites*, New York, Marcel Dekker, 1999, pp. 11-84.

[86] J. Chen, J. Shen, H. Huang and X. Xu, "Grinding characteristics in high speed grinding of engineering ceramics with brazed diamond wheels," *Journal of Materials Processing Technology*, vol. 210, pp. 899-906, 2010.

[87] B. Zhang and T. Howes, "Material-removal mechanisms in grinding ceramics," *CIRP Annals - Manufacturing Technology*, vol. 43, no. 1, pp. 305-308, 1994.

[88] H. Kirchner, "Comparison of single-point and multipoint damage in glass," *Journal of American Ceramic Society*, vol. 67, pp. 347-353, 1984.

[89] K. Trustrum, A. De and S. Jayatilaka, "On estimating the Weibull modulus for a brittle material," *Journal of Materials Science*, vol. 14, pp. 1080-1084, 1979.

[90] T. Hwang, C. Evans and S. Malkin, "An investigation of high speed grinding with electroplated diamond wheels," *CIRP Annals*, vol. 49, no. 1, pp. 245-248, 2000.